UNIVERSITÀ DEGLI STUDI DI TRIESTE

UNIVERSITÉ DE MONS

XXXV CICLO DEL DOTTORATO DI RICERCA IN

NANOTECNOLOGIE (DOCTORAT EN SCIENCES)

UNIVERSITÀ DI TRIESTE, UNIVERSITÉ DE MONS

Quantum-Chemical Modelling of the Photocatalytic Response of Functionalized 2D Carbon Nitride Materials

Settore scientifico-disciplinare: **CHIM/02**

DOTTORANDO

EDOARDO RACITI

COORDINATORE

PROF. ALBERTO MORGANTE

SUPERVISORE DI TESI

PROF. MAURIZIO PRATO

PROF. ROBERTO LAZZARONI

ANNO ACCADEMICO 2021/2022

Roberto Lazzaroni
Université de Mons

Alberto Morgante
Università di Trieste

Maurizio Prato
Università di Trieste

University of Trieste, Italy

University of Mons, Belgium

Quantum-Chemical Modelling of the Photocatalytic Response of Functionalized 2D Carbon Nitride Materials

XXXV Cycle of the joint PhD in Nanotechnology with the University of Mons

PhD Candidate

Edoardo Raciti

PhD Coordinator

Alberto Morgante (University of Trieste)

Thesis Supervisors

Maurizio Prato (University of Trieste, Italy)

Roberto Lazzaroni (University of Mons, Belgium)

Academic Year

2021/2022

Contents

Acknowledgements

First of all, this work is dedicated to myself, as a proof of having overcome some really high interior limits in a field that I used to consider beyond my capabilities and, secondly, to my family, for having supported me and always let me believe in myself.

A great thank you to Professor Maurizio Prato, for having made this project possible and for having welcomed me in Trieste.

A special thank you to Professor Roberto Lazzaroni, for having welcomed me in Mons, for his illuminating attitude, for his tendency not to rush things and for his clear explanations and solutions found in all possible situation where diplomacy is required.

A great thank you to Dr. Sai Manoj Gali for his patience and teaching in the Density Functional Theory World and for our stimulating conversations about personal growth and attitude in the academic world and for our pleasant moments with all the people from the Chimie des Matériaux Nouveaux (CMN), Univeristé de Mons, Belgium.

A special thank you to Prof. David Beljonne for his fresh and stimulating attitude towards the undertaken and obscure world of theoretical calculations, which surprisingly turn to be bright and a useful confirmation of the practical and real world.

A great thank you to Prof. Jérôme Cornil for his happy and friendly attitude in life, even during Master Courses attended in my PhD adventure.

A great thank you to all other Professors, Post-Docs and interns from the Chimie des Matériaux Nouveaux Group for the warm and pleasant atmosphere created in the lab.

A sincere thank you to Dr. Michele Melchionna for his calm attitude towards problems and life in general and for his ability of ironically take up things that would otherwise be heavy to deal with.

A special thank you to Dr. Giacomo Filippini for always stimulating my critical approach towards science, concepts and duties.

A great thank you to all other PhD Students, Post-Docs and interns from Prato Group for making me remember that synthetic organic chemistry and experimental data “somehow” exist.

A warm thank you to Dr. Francesca Martini, as one of my firm references of life, friendship, happiness and freedom in a world made of laughter, tenderness and complicity and for the support that she also provided for things I love.

A warm thank you to Dr. Edoardo Nisio, for his constant supply of Karma, valuable advice for my interior growth and valorization of the goals achieved in my life and for crazy things and conversations about philosophy, people, animals,… everything!

A warm thank you to Dr. Veronica Tringali, for striking back to my life as I approached Trieste and for her being out-of-schemes, for her complicity and effort in keeping alive a friendship “diluted” by kilometers and kilometers of distance and for rendering Friuli Venezia-Giulia a much better place when she comes back.

A warm thank you to Dr. Marc Morant Giner, for the sincere, happy and stimulating friendship made of trips, travels, dinners, long and deep conversations into life, points of view and philosophical sentences as tools for memorizing lessons of life.

A warm thank you to Dr. Francesco Palazzi (Francis Buildings!!), for giving me strength in certain moments, for the “canteen group” and for being a reference of trust and happiness in Trieste.

Chapter 1: Introduction

Clean energy exploitation and storage methods are two of the most appealing topics in environmental chemistry nowadays. The urgency to rely on novel approaches capable of setting up systems for energy production and conversion are becoming the basis for the future of our society. Among these, photocatalytic technology is considered one of the most promising tools to directly harvest, convert and store solar energy for generating sustainable and green energy and a broad range of environmental applications[1]. Some first examples can be found in biological systems' mimicking strategies, where the work of Bonchio *et al*. appears as a benchmark study in the field of artificial photosynthesis[2]. The most prominent cases however rely on the use of semiconductor-based photocatalysis for H_2 production from water-splitting, CO_2 reduction into "solar fuels" or for applications in organic synthesis and environmental remediation[1,3,4].

Classically, the semiconductors used for photocatalysis are based on metal oxides or sulfides. Among those, titanium dioxide (TiO_2) has been extensively investigated because of some attractive features, such as high chemical stability, easy synthesis and low-cost[5–7]. However, its absorption in the UV region of the spectrum due to its bang-gap of 3.2 eV, fast charge-carrier recombination and slow electron-hole diffusion, along with possible toxicity issues, limit its use. Recently, there has been a growing interest in developing new semiconductor photocatalysts based on abundant elements and that are able to utilize visible light and that exhibit favorable excited states dynamics and efficient charge transport[8–11].

In this context, graphitic carbon nitride is prominently emerging as one of the most promising and appealing materials. It is a metal-free 2D polymer made of carbon and nitrogen in a C/N ratio of ≈ 0.75 (see Fig. 1–1), which justifies the concise formula that identifies its stoichiometry as *g*-C_3N_4[12–14].

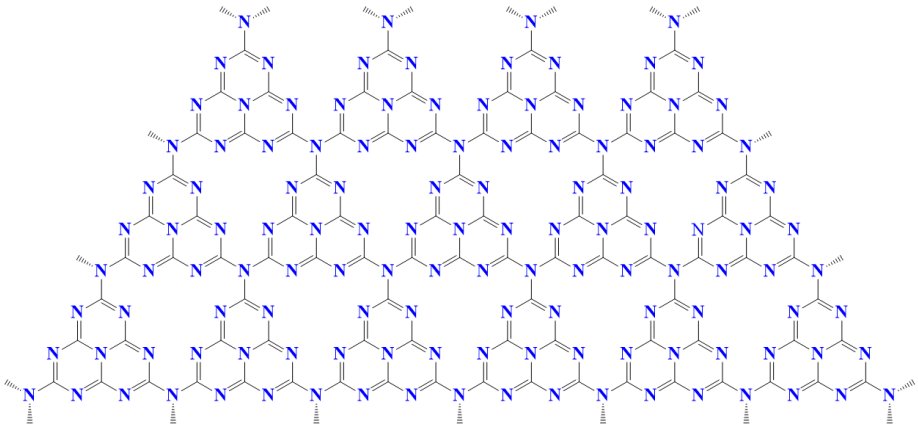

Figure 1–1: General representation of a 2D carbon nitride sheet (g-C_3N_4) based on melem units cross-linked via nitrogen bridges and stacked in a graphitic fashion.

Unlike TiO_2, which is active in the UV region, g-C_3N_4 possesses a bandgap of ca. 2.7 eV, making it a visible-light-active photocatalyst for a wide range of reactions[15–19]. Its Conduction Band (CB) and Valence Band (VB) positions are located at ≈ −1.1 eV and ≈ +1.6 eV vs. normal hydrogen electrode (NHE), respectively[20]. The absorption of light causes an electronic transition from VB to CB, as illustrated in Figure 1–2, after which an electron (e^-) is localized in CB and a positive hole (h^+) is left in VB.

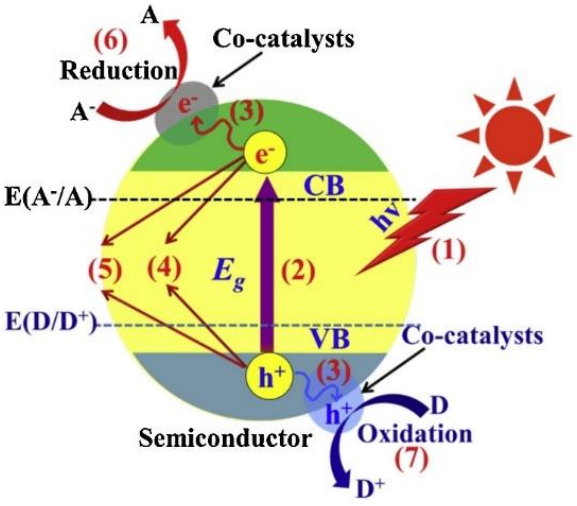

Figure 1–2[1]: Schematic representation of a general semiconductor electronic structure and possible electrochemical processes occurring upon photoexcitation across the Conduction Band (CB) -Valence Band (VB) bandgap or at the interface with a co-catalyst.

Apart from energy-related processes, *g*-C_3N_4 has also appeared as a very interesting photocatalytic material for a much broader range of chemical reactions, such as photocatalytic organic transformations[21], selective oxidations of alcohols[22], aerobic oxidative couplings of amines[23], dye degradation[24] and oxidative sulfonylations of alkenes[25]. This opens wide avenues for the easy and environmental-friendly synthesis of a large variety of organic compounds of industrial and pharmaceutical interest. Among those, two classes of reactions are investigated in our group at the University of Trieste. The first one is the coupling of a perfluorinated alkyl group to an electron-rich aromatic moiety via a C-C bond formation (an example is shown in Fig. 1–3a).

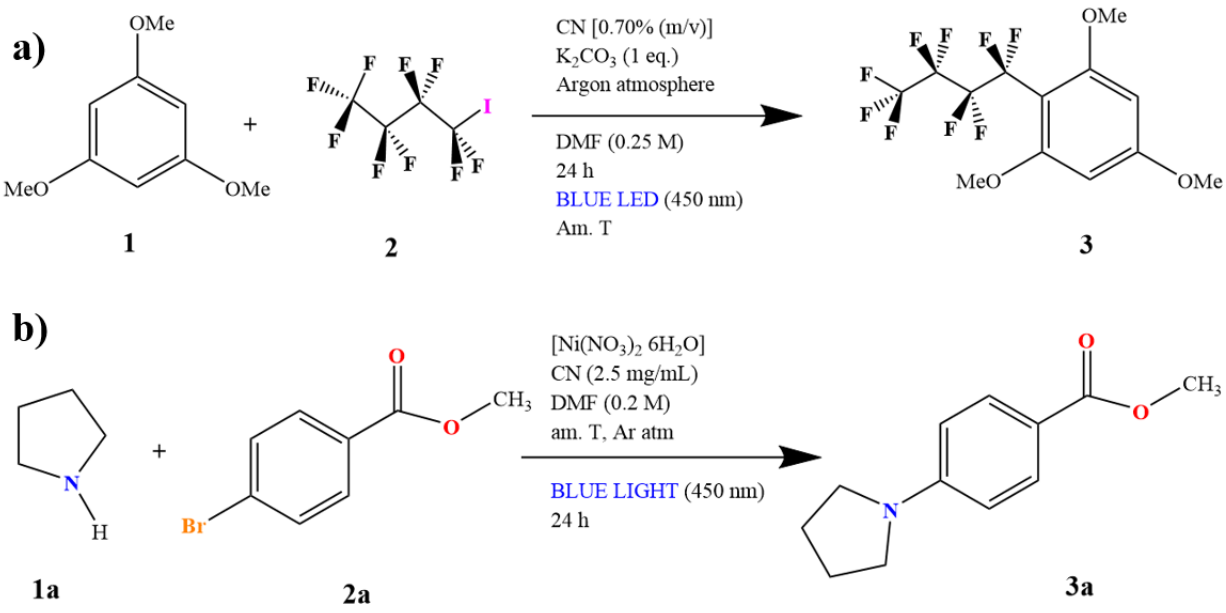

Figure 1–3: The reactions studied in this work: **a)** C–C bond-formation reaction between 1,3,5–trimethoxybenzene (**1**) and nonafluoro–1–iodobutane (**2**) and **b)** C–N bond-formation reaction between pyrrolidine (**1a**) and methyl–4–bromobenzoate (**2a**).

Fluoroalkylated groups are important compounds in medicinal chemistry, agrochemistry and materials science[26,27] because they add some convenient properties to the molecules to which they are bound, such as better lipophilicity[28,29] and increased cell membrane penetration at physiological pH values[30,31]. For this reason, the understanding of the reactions involving these important groups is important.

In order to optimize the conditions for reaction **a**), different modified forms of *g*-C_3N_4 were synthesized and their photocatalytic activity compared to that of pristine graphitic carbon nitride (*g*-C_3N_4). More specifically, a reduced form of carbon nitride (*red*. CN) was prepared from the pristine one in a tubular furnace at 550°C under H_2 flux; an oxidized form (*ox*. CN) by an oxidizing treatment with a 4 M solution of HNO_3; an amorphous form (*am*. CN) via a high-temperature treatment conducted in the tubular furnace under argon (Ar) atmosphere. All of these were fully characterized by TGA, TEM, XRD, XPS, UV-vis. and FT-IR spectroscopies and tested in the C-C coupling reaction[32]. In general, the more defects were created in the *g*-C_3N_4 structure, the more efficient it was in the reactions, with *am*. CN being the most active photocatalyst for reaction **a**). In order to understand in detail the relationship between the chemical structure of those modified CNs and their efficiency, we have decided to undertake a theoretical Density Functional Theory (DFT) study on their interactions with the fluorinated substrate and their reactivity. For this purpose, convenient theoretical models of the carbon nitrides and the perfluoroalkyl molecule have been built, based on the experimental data obtained. This permitted the determination of the electronic structure of all models, in particular in the Density of States plots (DOS). Based on those ground-state calculations, the modelling of the photochemical reaction was performed by means of Time-Dependent DFT (TD-DFT), which addresses the excited-state electronic structure. The theoretical optical absorption spectra have been calculated, along with the localizations of both hole (h^+) and electron (e^-) densities associated to each transition. In this way, the nature of the interaction between the carbon nitrides and the fluorinated molecule upon photoexcitation can be determined and relevant insight to understand the reaction mechanism can be obtained.

The second class of reactions of interest is the *g*-CN-assisted C-N coupling between a secondary amine and an aromatic core. This type of reaction involves the association of a light-induced

process with a non-photochemical second catalytic route, introducing the concept of "dual catalysis"[33]. One popular example consists in the combination of Ru or Ir polypyridyl complexes with a Ni-containing catalyst, which has given access to many challenging C-C and C-heteroatom couplings under mild reaction conditions[34]. However, it is once again desirable to use non-metallic photocatalysts for environmental reasons and carbon nitride has shown to meet the requirements to fit well in this other reactive scenario. The mechanism for this reaction is not fully understood and, to date, two hypotheses have been debated and presented in literature. The first one proposes that a Ni^0 species is transformed into a Ni^{II} complex through an oxidative addition step. Then, a single-electron transfer (SET) oxidation process of Ni^{II}, driven by the excited photocatalyst, may form a Ni^{III} complex, which undergoes a more facile reductive elimination than a Ni^{II} species. Lastly, the reduction of the Ni^{I} species closes the combined catalytic cycle[35,36]. In alternative to this route, a second possible scenario entails the light-mediated formation of a reactive Ni^{I} species from a Ni^{II}-based pre-catalyst, which is then capable of initiating a self-sustaining Ni^{I} /Ni^{III} operative cycle[37]. To shed light on that mechanism, in particular the details of the interaction between carbon nitride and the nickel species, a DFT study on model systems has been carried out, focusing on the use of a new microwave-treated carbon nitride (*mw*-CN), which appears to be the most efficient species for this reaction[38]. As for reaction 3a, suitable models for carbon nitride and the Ni complexes models have been conceived, on the basis on the experimental conditions at which the reaction is set up. Focusing on mechanism (b) we will build Ni^{II} complexes initially optimized in a DMF solvent cavity (the solvent of reaction). Then possible binding sites at the *mw*-CN surface will be hypothesized, which would coordinate the Ni^{II} metallic centers, acting as new ligands in the complexes. The possibility of an electron-transfer induced by the light absorbed by *mw*-CN will be investigated by means of TD-DFT; the localization of the

hole (h^+) and electron (e^-) densities of each transition will be determined and the stability of the Ni species on the *mw*-CN surface will be assessed.

Although DFT and TD-DFT are excellent methods for determining electronic structures, the latter often fails in the evaluation of Rydberg states, valence states exhibiting large π-systems[39,40] and charge transfers[41,42]. The problem with the first two depends on the wrong long-range behavior of current standard exchange functionals which decay faster than 1/*r*, *i.e*. the asymptotic decay that an electric potential term has in a typical Hamiltonian. Wavefunction-based methods such as Configuration Interaction (CI)[43,44], Complete Active Space Self-Consistent Field (CASSCF)[45], also including the second-order perturbative corrections (CASPT2)[46], could be an alternative, although only applicable to small molecules[39]. In conclusion DFT and TD-DFT remain the more appropriate methods to apply.

The manuscript is organized as follows:

Chapter 2 provides a general description of the structural, electronic and photocatalytic properties of carbon nitride, from both the experimental and modeling standpoints. In Chapter 3 we describe the general modelling methodology and the protocols used in the DFT calculations. Chapter 4 shows the results obtained for the first reaction modelled (C–C bond-formation reaction) while Chapter 5 is dedicated to the modeling of the second reaction (C–N bond-formation reaction). In Chapter 6 we give the major conclusions of this study and we propose some perspectives for future work.

References

[1] J. Wen, J. Xie, X. Chen, X. Li, *Appl. Surf. Sci.*, 391, (**2017**), 72–123.

[2] M. Bonchio, Z. Syrgiannis, M. Burian, N. Marino, E. Pizzolato, K. Dirian, F. Rigodanza, G. A. Volpato, G. La Ganga, N. Demitri, S. Berardi, H. Amenitsch, D. M. Guldi, S. Caramori, C. A. Bignozzi, A. Sartorel, M. Prato, *Nat. Chem.*, 11, (**2019**), 146–153.

[3] S. J. Mun, S. J. Park, *Catalysts*, (**2019**), 9, 805.

[4] A. J. Bard, M. A. Fox, *Acc. Chem. Res.*, 28, (**1995**), 141–145.

[5] P. V. Kamat, *J. Phys. Chem. C.*, 111, (**2007**), 2834–2860.

[6] J. Schneider, M. Matsuoka, M. Takeuchi, J. Zhang, Y. Horiuchi, M. Anpo, D. W. Bahnemann, *Chem. Rev.*, 114, (**2014**), 9919–9986.

[7] F. Zahng, J. Zaho, T. Shen, H. Hidaka, E. Pelizzetti, N. Serpone, *Appl. Catal. B*, 15, (**1998**), 147–156.

[8] Y. Shiraishi, T. Takii, T. Hagi, S. Mori, Y. Kofuji, Y. Kitagawa, S. Tanaka, S. Ichikawa,T. Hirai, *Nat. Mater.*, 18, (**2019**), 985–993.

[9] G. Parthasarathy, P. E. Burrows, V. Khalfin, V. G. Kozlov, S. R. Forrest, *Appl. Phys. Lett.*, 82, (**1998**), 2138–2140.

[10] S. Li, H. Wang, D. Li, X. Zhang, Y. Wang, J. Xie, J. Wang, Y. Tian, W. Ni, Y. Xie, *J. Mater. Chem. A*, 4, (**2016**), 15841–15844.

[11] F. Wang, W. K. H. Ng, C. Y. Jimmy, H. Zou, C. Li, L. Zhang, Z. Liu, Q. Li, *Appl. Catal. B*, 111–112, (**2012**), 409–414.

[12] A. Thomas, A. Fischer, F. Göttmann, M. Antonietti, J.-O. Müller, R. Schlögl, J. M. Carlsson, *J. Mater. Chem.*, 18, (**2018**), 4893–4908.

[13] Y. Wang, X. Wang, M. Antonietti, *Angew. Chem. Int. Ed.*, 51, (**2012**), 68–89.

[14] W. Tu, Y. Xu, J. Wang, B. Zhang, T. Zhou, S. Yin, S. Wu, C. Li, Y. Huang, Y. Zhou, Z. Zou, J. Robertson, M. Kraft, R. Xu, *ACS Sustain. Chem. Eng.*, 5, (**2017**), 7260–7268.

[15] X. Wang, K. Maeda, A. Thomas, K. Takanabe, G. Xin, J. M. Carlsson, K. Domen, M. Antonietti, *Nat. Mater.*, 8, (**2009**), 76–80.

[16] P. Choudhary, A. Bahuguna, A. Kumar, S. S. Dhankhar, C. M. Nagaraja, V. Krishnan, *Green Chem.*, 22, (**2020**), 5084–5095.

[17] A. Vijeta, E. Reisner, *Chem. Commun.*, 55, (**2019**), 14007–14010.

[18] H. Kasap, C. A. Caputo, B. C. M. Martindale, R. Godin, V. W. Lau, B. V. Lotsch, J. R. Durrant, E. Reisner, *J. Am. Chem. Soc.*, 138, (**2016**), 9183–9192.

[19] H. Kasap, D. S. Achilleos, A. Huang, E. Reisner, *J. Am. Chem. Soc.*, 140, (**2018**), 11604–11607.

[20] S. C. Yan, S. B. Lv, Z. S. Li, Z. G. Zou, *Dalton Trans*., 39, (**2010**), 1488.

[21] A. Savateev, I. Ghosh, B. König, M. Antonietti, *Angew*. *Chem*. *Int*. *Ed*, 57, (**2018**), 15936–15947.

[22] F. Su, S. C. Mathew, G. Lipner, X. Fu, M. Antonietti, S. Blechert, X. Wang, *J*. *Am*. *Chem*. *Soc*., 132, (**2010**), 16299–16301.

[23] F. Su, S. C. Methew, L. Möhlmann, M. Antonietti, X. Wang, S. Blechert, *Angew*. *Chem*. *Int*. *Ed*., 50, (**2011**), 657–660.

[24] G. Li, J. Shi, G. Zhang, Y. Fang, M. Anpo, X. Wang, *Res*. *Chem*. *Intermed*., 43, (**2017**), 5137–5152.

[25] A. U. Meyer, V. W.-h. Lau, B. König, B. V. Lotsch, *Eur*. *J*. *Org*. *Chem*., (**2017**), 2179–2185.

[26] K. Müller, C. Faeh, F. Diederich, *Science*, 317, (**2007**), 1881–1886.

[27] R. Berger, G. Resnati, P. Metrangolo, E. Weber, J. Hulliger, *Chem*. *Soc*. *Rev*., 40, (**2011**), 3496–3508.

[28] H. J. Böhm, D. Banner, S. Bendels, M. Kansy, B. Khun, K: Muller, U. Obst-Sander, M. Stahl, *ChemBioChem*, 5, (**2004**), 637–643.

[29] K. L. Kirk, *Curr*. *Top*. *Med*. *Chem*., 6, (**2006**), 1445.

[30] M. B. van Niel, I. Collins, M. S. Beer, H. B. Broughton, S. K. F. Cheng, S. C. Goodacre, A. Heald, K. L. Locker, A. M. MacLeod, D. Morrison, C. R. Moyes, D. O'Connor, A. Pike, M.Rowley, M. G. N. Russell, B. Sohal, J. A. Stanton, S. Thomas, H.Verrier, A. P. Watt, J. L. Castro, *J*. *Med*. *Chem*., 42, (**1999**), 2087–2104.

[31] M. Morgenthaler, E. Schweizer, A. Hoffmann-Roeder, F. Benini, R. E. Martin, G. Jaeschke, B. Wagner, H. Fischer, S. Bendels, D. Zimmerli, J. Schneider, F. Diederich, M. Kansy, K. Mueller, *ChemMedChem*, 2, (**2007**), 1100–1115.

[32] G. Filippini, F. Longobardo, L. Forster, A. Criado, G. Di Carmine, L. Nasi, C. D'Agostino, M. Melchionna, P. Fornasiero, M. Prato, *Sci*. *Adv*., 6, (**2020**).

[33] K. L. Skubi, T. R. Blum, T. P. Yoon, *Chem*. *Rev*., 116, (**2016**), 10035–10074.

[34] R. Sun, Y. Qin, D. G. Nocera, *Angew*. *Chem*. *Int*. *Ed*., 59, (**2020**), 9527–9533.

[35] E. B. Corcoran, M. T. Pirnot, S. Lin, S. D. Dreher, D. A. Dirocco, I. W. Davies, S. L. Buchwald, D. W. C. MacMillan, *Science*, 353, (**2016**), 279–283.

[36] J. C. Tellis, D. N. Primer, G. A. Molander, *Science*, 345, (**2014**), 433–436.

[37] L. Cavallo. M. Rueping, B. Maity, C. Zhu, H. Yue, L. Huang, M. Harb, Y. Minenkov, *J*. *Am*. *Chem*. *Soc*., 142, (**2020**), 16942–16952.

[38] M. Marchi, E. Raciti, S. M. Gali, F. Piccirilli, H. Vondracek, A. Actis, E. Salvadori, C. Rosso, A. Criado, C. D'Agostino, L. Forster, D. Lee, A. Foucher, R. K. Rai, D. Beljonne, E. Stach, M. Chiesa, R. Lazzaroni, G. Filippini, M. Prato, M. Melchionna, P. Fornasiero, *submitted*, (**2023**).

[39] Z-. L. Cai, K. Sendt, J. R. Reimers, *J. Chem. Phys.*, 117, (**2002**), 5543.

[40] S. Grimme, M. Parac, *Chem. Phys. Chem.*, 3, (**2003**), 292.

[41] D. J. Tozer, R. D. Amos, N. C. Handy, B. J. Roos, L. Serrano-Anders, *Mol. Phys.*, 97, (**1999**), 859.

[42] A. Drew, M. Head-Gordon, *J. Am. Chem. Soc.*, 136, (**2004**), 4007.

[43] P. Carsky, P. v. R. Schleyer, N. L. Clark, J. Gasteiger, P. R. Schreiner, Eds.; Wiley: Chichester, U. K., (**1998**), p. 485.

[44] W. Kutzelnigg, *J. Mol. Struct.*, (*THEOCHEM*), 181, (**1988**), 33.

[45] B. O. Roos, *Adv. Chem. Phys.*, 69, (**1987**), 399.

[46] K. Andersson, B. O. Roos, D. R. Yarkony, *Ed.*; *World Scientific*: *New York*, (**1995**), *Vol.* 1, *p.* 55.

Chapter 2: Structural and electronic properties of carbon nitride catalytic materials

2.1 Structural insights in C- and N-containing 2D materials

There is currently great interest in developing the solid-state chemistry of novel high density C-N-H materials that possess useful electronic and mechanical properties[1]. These include a family of related solid-state materials based on the "melem" structural unit ($C_3N_{10}H_6$ and $C_6N_7(NH_2)_3$). Liebig first gave the name "melon" to an amorphous solid with an approximate composition near $C_6N_9H_3$ that had been previously described by Berzelius[1]. The current interest for this class of compounds arose due to its similarity to graphene, which is an excellent material for electronic applications.

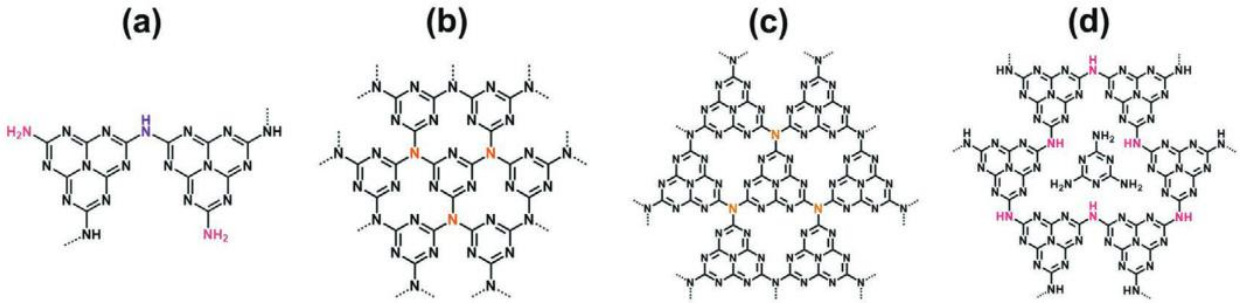

Figure 2–1[2]: Schematic illustrations showing basic structural units of polymeric CN materials; **a)** melon; **b)** triazine-based structure; **c)** heptazine-based structure; **d)** poly(heptazine imide).

Figure 2–1 shows possible geometrical arrangements of C-, N- and H-enriched layers, which have attracted considerable attention due to their electronic and solid-state properties. Each of them was obtained by different research groups and they are all good examples of how "melem" or "melon" are the repeating units in such layers. As illustrated in Figure 2–2, the former is a molecular structure formed by the condensation of three 1,3,5-triazines bearing peripheral $–NH_2$ groups, corresponding to a triamino-heptazine molecule. The latter consists of a linear polymer of interconnected tri-s-triazines via secondary nitrogens, also known as heptazines.

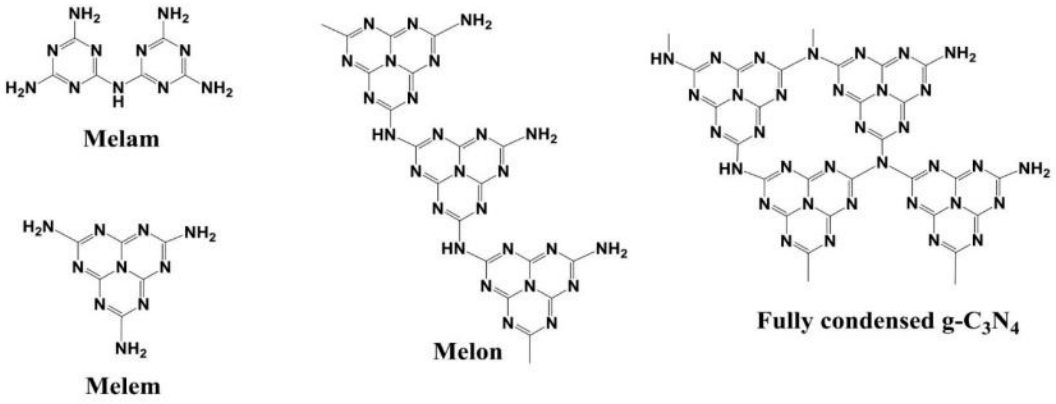

Figure 2–2[3]: Structures of melam, melem, melon and fully condensed graphitic carbon nitride.

Further insights into "melon" structures were provided by Franklin as early as 1922[4]. He found that the empirical composition of melon derivatives obtained from mercuric thiocyanate varied with the method of preparation and that the hydrogen content varied from 1.1 to 2.0 wt%. It was hence concluded that probably not one single structure should be assigned to it, as it is more likely to be a mixture of polymers of different sizes and architectures. Besides melon, most polymeric CN materials are also constructed from heptazine (1,3,4,6,7,9,9b-heptaazaphenalene, or tri-s-triazine, C_6N_7) building blocks and if one heats melamine (one of the possible N- and H-enriched precursors), a three component heptazine-based melem can be obtained[2]. The condensation of melem above 520°C induces the formation of $[C_6N_7(NH_2)(NH)]_n$ poly(amino-imino) heptazine units, known indeed as Liebig's adduct "melon".

As a metal-free photocatalyst, carbon nitride has attracted increasing attention, due to its easy availability, capability of absorbing visible light with wavelength up to around 450 nm, low-cost and good stability[5–7]. In particular, graphitic carbon nitride (g-C_3N_4) has been explored to capture, activate and reduce CO_2 via thermal catalysis in the presence of sacrificial hydrocarbons and visible light. The formation of carbamate species follows from the binding of CO_2 to the heptazine-based covalent framework with Lewis basic functions[8]. More specifically, g-C_3N_4 is a 2D fully

conjugated polymer constituted by C, N and H, which is usually obtained from the commercially available melamine molecule[9] through pyrolysis reaction (Figure 2-3), even though other typically employed starting materials include cyanamide[10], dicyanamide[11], thiourea[12], urea[13] or a mixture thereof[14]. For instance, Montigau *et al*. reported on the solvothermal condensation of melamine with cyanuric chloride[15], while Qian *et al*. synthesized carbon nitrides by condensing cyanuric chloride and calcium cyanamide[16]. Another benchmark step towards better defined and organized *g*-C_3N_4 systems was published by Schnick *et al*., who were able to isolate and solve the crystal structure of another intermediate, the 2,5,8-triamino-tri-s-triazine (melem), with the chemical formula $C_6N_{10}H_6$[17]. Despite its stability, if further heated, it could yield only poorly-defined amorphous carbon nitride[18].

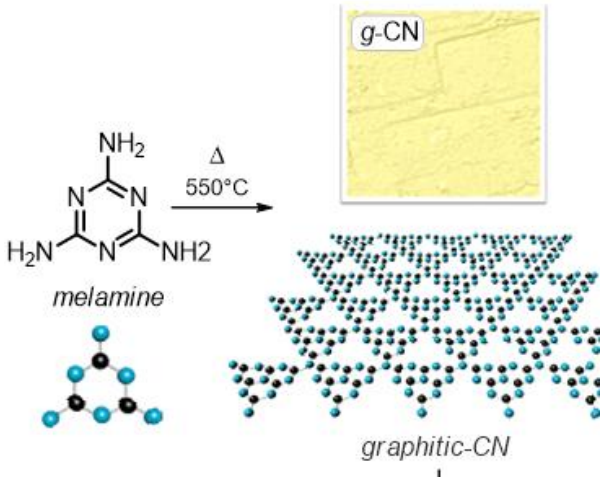

Figure 2–3[19]: The synthetic precursor melamine and carbon nitride (*g*-C_3N_4).

From a more historical and broader point of view, it was shown that the combustion of mercury(II) thiocyanate to form "Pharaoh's serpents" yielded a carbon nitride with the ideal formula "C_3N_4" along with HgS[20]. This is a spectacular reaction, first described two centuries ago, often used to show the magic that chemistry can make (see Fig. 2–4). The reaction equation is as follows:

$$2Hg(SCN)_2 \rightarrow 2HgS + CS_2 + C_3N_4. \quad \text{(Eq. 1)}$$

Its mysterious and interesting name derives from a previous attempt to obtain thiocyanic acid (HSCN) by treating mercury(II) thiocyanate by Wöhler *et al*., who noted the characteristic appearance of the voluminous porous solid residue that emerged as the salt burned in air[21,22]. Combustion analysis measurements of the overall bulk showed that the light element composition (C, N, H) yielded a C/N ratio of 0.74, very close to the ideal C_3N_4 stoichiometry (0.75).

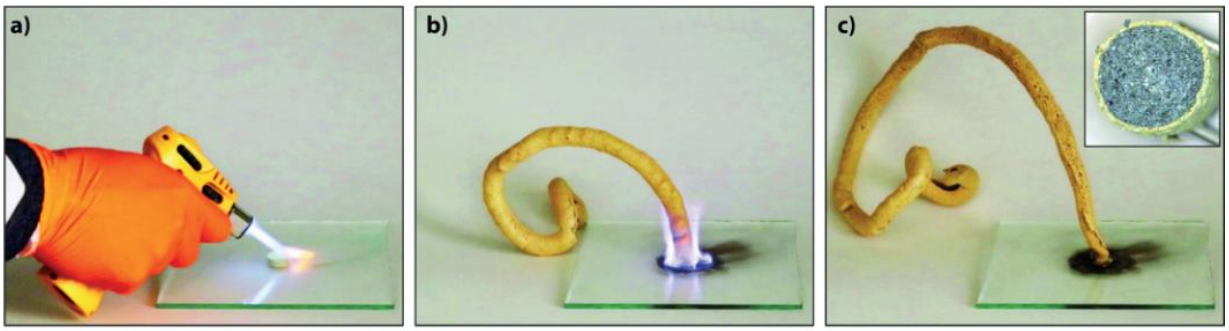

Figure 2–4[20]: The Pharaoh's serpents' reaction. **a)** ignition of $Hg(SCN)_2$; **b)** the progress of the self-propagating combustion reaction; **c)** the final reaction product. Inset in **c)** shows a cross-section of a branch of a Pharaoh's serpent product material.

The presence of triazines and/or heptazines in carbon nitride has been revealed by spectroscopic measurements: T. S. Miller *et al*. have recorded an ATR-FTIR spectrum showing a strong band between 2900 and 3400 cm^{-1}, associated to –NH– and $–NH_2$ groups of a polyheptazine-like material[23]. The XPS spectrum in the C1s region presents a peak at 288.2 eV assigned to an sp^2 C atom bonded to an N atom within either a triazine or heptazine unit[20]. McMillan *et al*. obtained a UV-vis. absorption spectrum whose overall aspect is similar to that observed for the polymeric compound $C_xN_yH_z$, which has an heptazine-based structure[1]. The synthesis of microscopic flakes of triazine-based graphitic carbon nitride composed of nitrogen-linked triazine units was also reported recently[24].

Carbon nitride has a very good chemical and thermal stability, along with optical characteristics that make it a suitable material in solar cells and fuel cells electrodes[25,26]. There is therefore a considerable effort in trying to expand the methodologies and deeply investigate its synthesis, electronic structure, elastic hardness and linear and non-linear optical responses[27–33]. All of these properties however depend on the structural characteristics of carbon nitride, or more precisely on its polymorphs. Up to now, four phases of C_3N_4, in addition to the common *g*-C_3N_4, are known: α–C_3N_4, β–C_3N_4, cubic-C_3N_4 and pseudo-cubic C_3N_4[34,35] (Fig. 2–5).

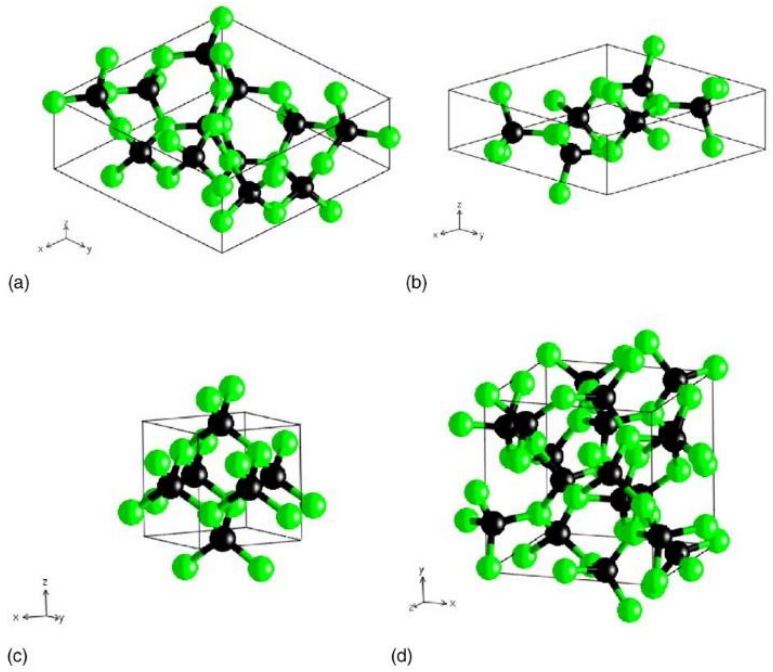

Figure 2–5[35]: Theoretical models of the carbon nitride polymorphs: (a) α-C_3N_4 (P31c); (b) β-C_3N_4 (P63/m); (c) "pseudo-cubic" or "(defect) zincblende"-C_3N_4 ($P\bar{4}2m$); (d) "cubic" or "willemite-II" C_3N_4.

Interest in dense carbon nitride polymorphs based on sp^3-bonded C atoms began with predictions of superhard properties from density functional theory (DFT) calculations[38,39]. A first-principle pseudopotential calculation for the structural and physical properties of carbon nitride predicts a cubic form, with a zero pressure bulk modulus exceeding that of diamond[35], whereas another theoretical study indicates that β–C_3N_4 possesses a larger hardness[36]. The calculated bulk

modulus of α–C_3N_4 shows, on the other hand, that the hardness is approximately that of diamond[37]. Those results, in combination with experimental studies, showed the existence of carbon nitride structures containing both sp^2 and sp^3 bonded C atoms obtained from the graphitic layered polytriazine imide (PTI) compound $C_6N_9H_3 \cdot HCl$[40].

2.2 Electronic properties, elemental doping and absorption of light

As previously reported, *g*-C_3N_4 exhibits interesting features such as the absence of metallic elements, the possibility to be easily synthesized and a tunable band-gap of about 2.7 eV, which enables absorbing radiations in the visible region[41–43]. Those properties open the possibility for carbon nitride to be employed as a photocatalyst[41,42,44–47] but its efficiency is in general rather poor. This is due to its low surface area, fast charge-carrier recombination and consequently the reduction of charge-carrier mobility[48–55]. In order to overcome these difficulties, several strategies have been adopted: (i) It was shown that ***the introduction of non-metal elements***, such as C, N, P or S, into the *g*-C_3N_4 framework modulates its surface morphology, size of particles, electronic, optical and other physico-chemical properties[56–60]. Other groups reported on: (ii) the synthesis of mesoporous *g*-C_3N_4 (*mpg*-C_3N_4)[61,62], (iii) the fabrication of ultrathin *g*-C_3N_4 nanosheets[63], (iv) the acidification with concentrated acids which in particular generates a higher specific surface area[64], and (v) the combination with other semiconductors for the formation of heterojunctions[65–67], all of them being equally valuable techniques to ameliorate the properties of the pristine material. Li *et al*., for example applied thioacetamide as a sulfur source for obtaining an S-doped terminal-methylated *g*-C_3N_4 (SM-*g*-C_3N_4)[68], which shows a valence band-splitting near the Fermi level and the appearance of a mid-gap electronic state, with a consequent decrease of the band-gap. Su *et al*. performed the thermal condensation of adenosine phosphate and urea followed by thermal exfoliation to obtain porous P-*g*-C_3N_4 nanosheets[69]. It was shown that the P-doping

changed the original band gap structure due to the formation of impurity level between the valence- and the conduction-band. A decrease in the VB position from 1.7 to 1.57 eV was suggested as a result of defects generation under the thermal exfoliation. Li *et al*. introduced intra- and inter-triazine N-vacancies into *g*-C_3N_4 during melamine treatment in various atmospheres[70]. DFT calculations and optical properties studies demonstrated that the band-gap was only slightly reduced by the intra-triazine N-vacancy but was strongly reduced by the inter-triazine N-vacancy. Table 2–1 below shows different non-metal doping CN products with different applications.

Table 2-1[71]: Different gCN-based catalysts obtained by different doping methods, each of them yielding different band-gaps, SSA, applications and improved performance.

Dopant (s)	**Catalyst**	**Synthetic method**	**Bandgap** (eV) **(pour vs. doping)**	**SSA** (m^2/g) **(pour vs. doping)**	**Application**	**Improved performance**	**Reusability and stability (after 5 cycles)**	**Ref.**
C	BTPMC g–C_3N_4	Thermal condensation	2.75 vs 2.28	48.6 vs 49.6	Photocatalytic BPA degradation	-	No significant change	[72]
N	NDCN–4S	Thermal treatment	2.51 vs 2.54	18.36 vs 74.79	Photocatalytic TC degradation	2.07 times	Slightly decreased	[73]
N	TCN(NH_3)	Supramolecular self-assembly	-	8.6 vs 135.8	Photocatalytic CO_2 reduction	17 times	Maintained at 100 μmol $g^{-1}h^{-1}$	[74]
S	MTCN–6	Self-assembling	2.71 vs 2.64	16.3 vs 66.4	Photocatalytic H_2 generation	11 times	No obvious decrease	[75]
P	P–C_3N_4	Thermal co-poly-condensation	2.67 vs 2.57	12.37 vs 40.89	Photocatalytic Rh B degradation	18 times	Decreased from 100% to 91.2%	[76]

Metal-doping is an equally-sought strategy used to improve carbon nitride's catalytic performance, also directly addressing its physical and electronic properties. A wide range of interesting applications of metal-doped carbon nitride materials have recently been investigated from photocatalysis to other emerging fields, including electrocatalysis, organic synthesis, biosensors, and nanozymes[77]. The inclusion of typical metallic elements like Fe, Cu, Zn, Ni allows for light-absorption modulation, band-gap reduction, charge mobility improvement and the extension of charge-carrier lifetime[78–82]. For instance, the inclusion of Zn^{2+} and Fe^{2+} into the *g*-C_3N_4 framework was reported for the first time by Wang *et al*[83]. It was found that the metal-

containing *g*-C_3N_4 expanded the light-absorption range and that the band-gap of the metal/*g*-C_3N_4 nanohybrid gradually shifted to higher wavelengths (lower energies) with increasing metal contents. Ding *et al*. revealed that other transition metal cations, such as Ni^{2+}, Cu^{2+}, Co^{3+} and Mn^{3+}, could all be incorporated into the *g*-C_3N_4 framework without destroying its hosting ability[84]. Analogously to Wang's observations, the abovementioned transition metals were also able to noticeably extend the light-absorption spectrum of the material to longer wavelengths and significantly retard the recombination of photo-induced charge-carriers. In addition to transition metal ions, the coordination of alkali metal ions such as K^+, Na^+ and Li^+ into the nitrogen sites of *g*-C_3N_4 was also observed[85, 86–89]. Their introduction remarkably ameliorates the transfer, transport and separation efficiency of charge carriers to create a spatial charge distribution for enhanced photocatalytic redox reactions[90,91].

Molecular doping is a strategy used to tackle the possibly main drawback that carbon nitride and, in general, semiconductors can suffer from, *i.e*. the recombination of the electrons and holes generated upon absorption of photons. The bandgap engineering via cation, anion or their cooperative doping has been demonstrated as an effective procedure to enhance the optical absorption of wide band-gap semiconductors for relevant chemical conversions via sunlight[92,93]. It is also known that the incorporation of entire molecules in the carbon nitride structure can equally adjust its optical and/or electronic properties. Chen *et al*. selected a π-deficient pyridine ring, which appeared to effectively modulate its electronic and band structure by affecting its π-electrons[94]. Zhang *et al*. used electron-rich thiophene donors, which showed a marked capacity of changing the intrinsic bulk and surface features, promoting the charge-carrier migration and separation by forming surface dyadic structures[95].

On the other hand, the ***construction of g-C_3N_4-based heterojunction*** nanohybrids is an alternative to doping and it consists of the connection between two semiconductors, *i.e.* carbon nitride with another one, namely the co-catalyst[96]. Once spatially separated, the charge generated from the excited states are able to initiate the reduction and oxidation processes. The location of the reactive sites can be either on the carbon nitride surface where the photoexcitation occurs or across the interface with the other semiconductor. The coupling between carbon nitride and another semiconductor with dissimilar band and electronic structures results in a new electronic structure after hybridization. In other words, band bending is created at the interface of the heterojunction nanocomposites as a result of the potential difference between the two sides[97]. This in turn induces a built-in electric field within a space charge region to spatially separate and migrate the photogenerated electrons and holes[98]. There are typically three types of heterojunctions, based on the relative the positions of the CB and VB (Fig. 2–6): Type I (straddling gap), Type II (staggered gap) and Type III (broken gap)[99]. Type I band alignment features both the CB and VB potentials of the smaller band-gap semiconductor. In such configuration, both the electron and hole photogenerated in the larger bandgap material are expected to be transferred to the lower-gap material and charge separation is not favored. Type II features staggered CB and VB between the two semiconductors; here electron-hole pairs photogenerated in both materials are expected to be separated at the interface. Type III, both the CB and VB of one component are located above the CB of the other one. To favor charge separation upon photoexcitation, carbon nitride must therefore be associated with another semiconductor so that a type II heterojunction is formed.

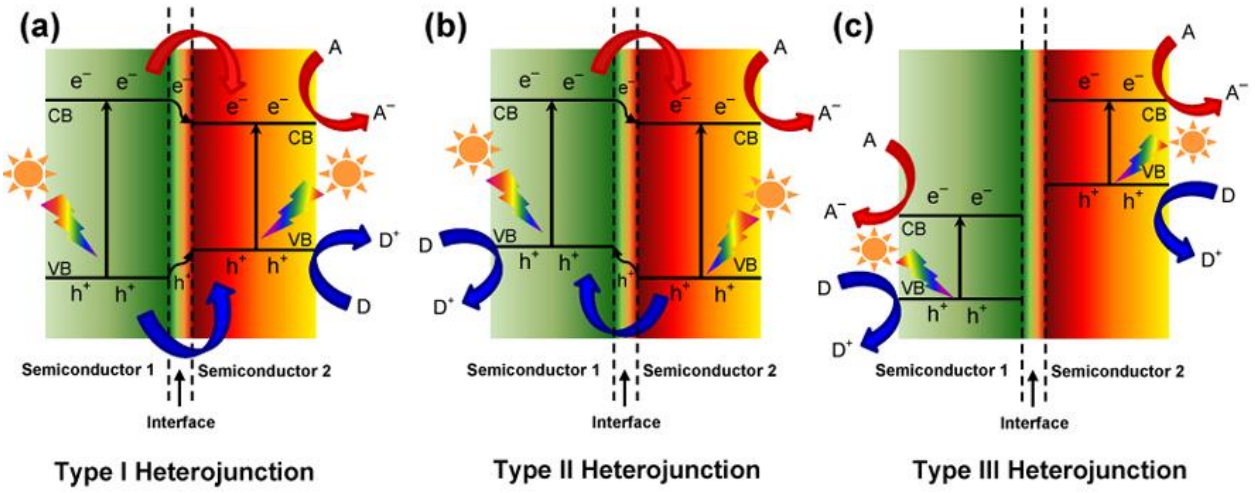

Figure 2–6[96]: Schematic energy band diagram of three different types of heterojunctions in a typical semiconductor hybrid nanocomposite: **(a)** Type I heterojunction; **(b)** Type II heterojunction; **(c)** Type III heterojunction.

The construction of such systems was further encouraged by the intrinsic properties of carbon nitride, since its band-gap of 2.7 eV is lower than many other oxide semiconductors previously studied[100]. Therefore, many different type II heterojunction composites with oxide semiconductors have been reported using carbon nitride. Several groups have recently investigated the properties of carbon nitride-TiO_2 composites[101–106]. Bledowski *et al*. showed that the in-situ formation of carbon nitride in the presence of TiO_2 leads to very intensive interfacial contact between both semiconductors, resulting in a core–shell morphology[103]. Carbon nitride has also been used to prepare composite photocatalytic systems with Ag_3PO_4[107], Bi_2WO_6[108,109], $Bi_5Nb_3O_{15}$[110], BiOBr[111,112], CdS[113,114], $CuInS_2$[115], Fe_2O_3[116], Fe_3O_4[117], N-$H_2Ta_2O_6$[118], MoS_2[119], N-Nb_2O_5[120], $SrTiO_3$[121,122], TaON[123], WO_3[124], ZnO[125] and $ZnWO_4$[126] with enhanced catalytic activity due to improved charge carrier separation relative to that of non-composite materials.

2.3 Photocatalytic use of carbon nitride

In recent years, the use of *g*-C_3N_4 has also been extended to photocatalytic organic synthesis for preparing industry-relevant compounds with an environmentally-friendly approach[127]. Thanks to its convenient characteristics, carbon nitride can meet the requirements for many industrial scale-up methods and it is also easily separable from the reaction mixture. While mainly used in photocatalytic oxidations of small molecules, carbon nitride is also active for C–C or C–heteroatom bond formation reactions[128–131]. These include the functionalization of arenes and heteroarenes with fluoroalkylated groups[132], which are important compounds in medicinal chemistry, agrochemistry and material science. Sci *et al*. recently reported the perfluoroalkylation of terminal alkynes by use of mesoporous graphitic carbon nitride (*mpg*-C_3N_4)[133]; Mazzanti *et al*. performed dichloromethylation of enones by carbon nitride photocatalysis[134]; Rueping *et al*. reported the generation of α–aminoalkyl radicals with heterogeneous *g*-C_3N_4 for addition reactions onto electrophiles[135]. The anchoring of fluorinated groups to organic substrates has indeed attracted considerable attention, mostly due to their relevance in medicinal and industrial chemistry[127]. In particular, the trifluoromethyl $–CF_3$ group is typically used in common drug candidate protecting strategies against *in vivo* metabolism. These reactions are generally accomplished with transition metal-catalyzed cross-couplings, which are another important chapter in modern organic chemistry. MacMillan *et al*. reported the trifluoromethylation of arenes and heteroarenes by iridium and ruthenium photocatalysts[136]. A method involving carbon nitride was proposed by Blechert *et al*., although the yields were lower[137].

2.4 Carbon nitride in cross-coupling reactions with metallic complexes

The combined use of a photocatalyst and a metal complex is gaining increasing attention thanks to the plethora of unlocked affordable reactions, based on the pioneering work of MacMillan, Stephenson, Yoon and their co-workers[138–142], who have systematically introduced the concept of photoredox catalysis. Here, the light-induced redox abilities of molecular chromophores, namely photocatalysts (PCs), are exploited[143,144]. From a mechanistic point of view, PC reaches an electronically excited state upon absorption of light (PC*), from which single-electron transfer (SETs) events can take place, to then return to its ground state either by a reductive or an oxidative quenching cycle (see Fig. 2–7).

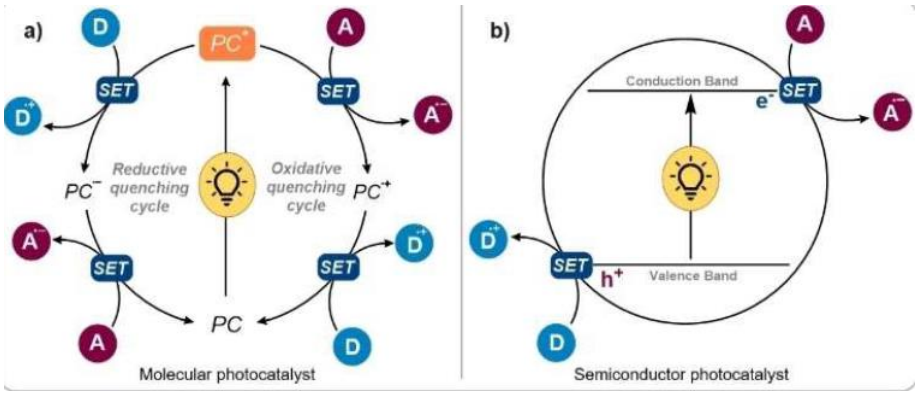

Figure 2–7[145]: (**a**) General reductive and oxidative quenching cycles exploited in homogeneous photoredox catalysis. (**b**) General catalytic mechanism of heterogeneous photoredox catalysis. PC: photoredox catalyst; D: electron donor; A: electron acceptor.

In the former, PC* promotes a SET oxidation of an electron-rich donor species (D). Afterwards, the reduced catalyst is restored to its ground state through a second electron transfer process by reducing an electron-deficient acceptor species (A). The opposite sequence occurs in the oxidative quenching cycle, where the PC* donates one electron to A, and successively the oxidized photocatalyst is reduced by D. Iridium and ruthenium are the most commonly employed metallic centers of polypyridyl PCs and they are typically used as the photoabsorbing species coupled with

a nickel-containing catalyst[145–148]. The latter stands as one of the better-suited transition metals to use in such reactions thanks to its high abundance, low cost, different valence electronic configurations (d^{10}, d^8 or more rarely d^7) and the consequently related oxidation states (0, +2 or more rarely +3). It is in such conditions that the concept of dual catalysis can be defined, *i.e.* a first photoredox and a second non-photochemical catalytic cycle are coupled, in order to take advantage of the synergy between the two[145]. Figure 2–8 summarizes the possible oxidation/reduction cycles that Ni species can undergo in cooperation with a convenient photocatalyst mediating the cross-coupling reactions of different substrates R^1–YH (amines, alcohols, thiols). The distinction of the light-mediated and dark-cycles is also described below.

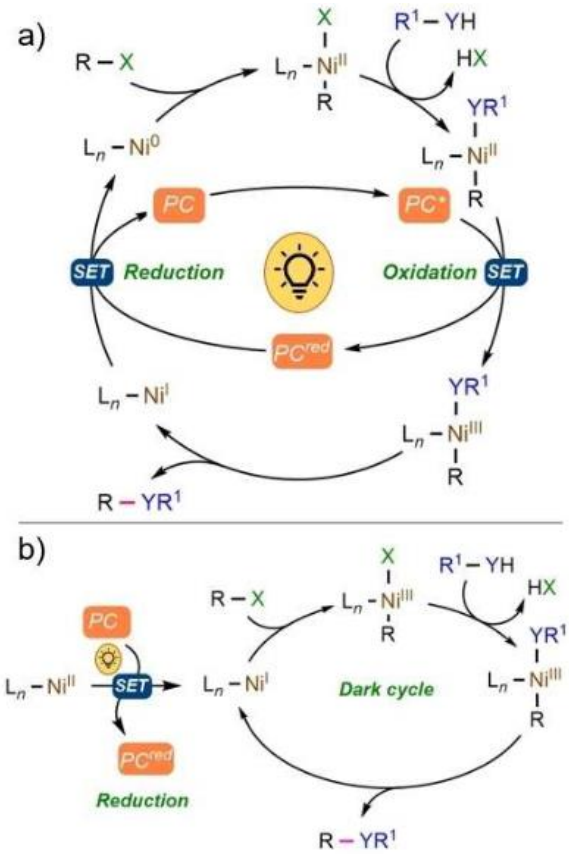

Figure 2–8[143]: General scheme of Ni-catalyzed cross-coupling reactions of substrates R^1–YH of interest **a)** oxidation of Ni(II) coordination compound to Ni(III) and the coupling product R–YR^1; **b)** distinction of the light-mediated and dark-cycle of dual catalytic cross-coupling reactions.

In principle, other mechanisms of both the light-mediated and dark cycles are possible according to MacMillan[149], Miyake[150] and a review published by Wenger[151]. The versatile behavior of nickel permits pathways where it can receive an electron from a reducing excited photocatalyst (PC*), becoming Ni(I) from its initial Ni(II) coordination compound. It can otherwise be oxidized as reported above from an oxidizing excited PC*, becoming a Ni(III) species from its initial Ni(II) state.

Carbon nitride is able to conveniently insert in this reactive scenario. Pieber *et al*. show how the 2D material can be used not only as the photocatalyst but also as a limiting agent preventing the formation of the "nickel black"[152], which interrupts the cross-coupling reaction. In particular, a carbon nitride obtained from the co-condensation of urea and oxamide followed by post-calcination in a molten salt (m-OA) was used in that study. Its broad absorption enables wavelength-dependent control of the rate of the reductive elimination step, which prevents the formation of nickel black. Another use of the abovementioned material was described by Pieber *et al*. in a more modern continuous flow process, set up by the assembly of an oscillatory pump with a microstructured plug-flow photoreactor in order to better stabilize solids in flows[153]. Through careful tuning of the oscillator properties, an excellent performance of the CN-OA-m was achieved over 10 cycles without loss of activity and this enabled the isolation of the desired coupling products on the 10g-scale.

2.5 Modelling the electronic properties of carbon nitride

As reminded above in this chapter, carbon nitride can exist in different forms, featuring different C/N ratios. Although *g*-C_3N_4 is the most stable allotrope, other polymorphs are equally important such as CN, C_2N, C_3N, C_4N, and C_5N, which have also been studied through Density Functional

Theory (DFT) calculations[154]. All these carbon nitride materials possess some similarities with graphene in that they are all two-dimensional with sp^2 hybridized conjugated C atoms. Among the CN structures, C_2N_2, C_3N_3 and C_4N_4 exhibit high structural stability and good conductivity. Their structure possesses round and uniform pores, six pyridinic nitrogens in each unit cell and a bandgap of ≈ 1.5–1.6 eV (Fig. 2–9a,b). The structure of C_2N exhibits sp^2 hybridization and it is filled with uniformly sized pores and a large one at the center, which is due to the six-member nitrogen-containing ring (Fig. 2–9c). The location of the nitrogen atoms in the structure of C_2N makes the π–electronic structure of its benzene rings isolated, making it a semiconductor with a bandgap of 1.96 eV (Fig. 2–9d).

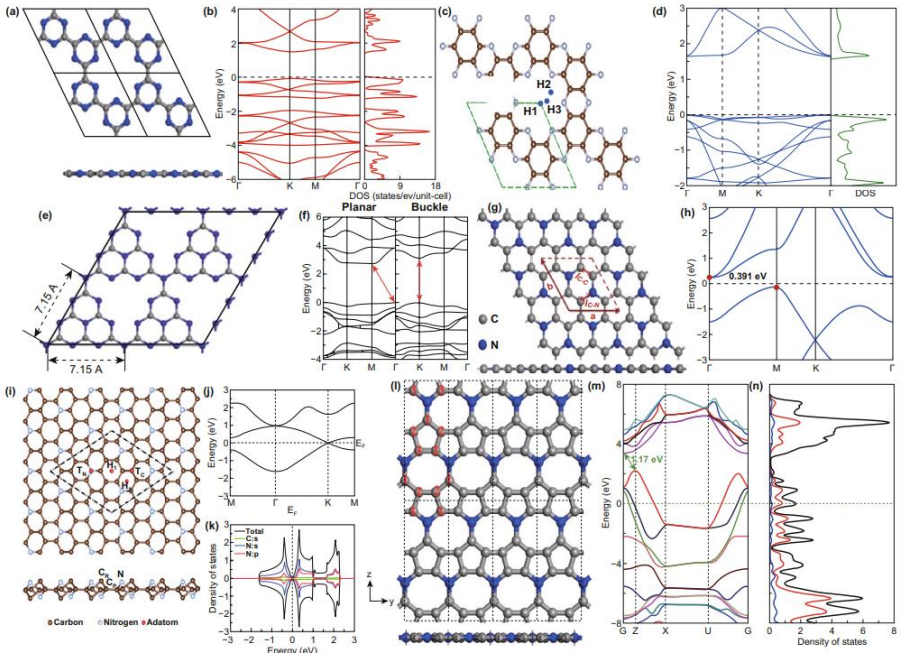

Figure 2–9[154]: **a**. Top view and side view of the supercell (2×2) *g*-C_3N_3; **b**. Band structure and total density of state for 1×1 *g*-C_3N_3: **c**. Relaxed structure of 2×2 C_2N monolayer; **d**. Band structure and density of states of C_2N monolayer; **e**. Schematic structure of monolayer *g*-C_3N_4; **f**. Calculated band structures of monolayer *g*-C_3N_4 with planar or buckled topology; **g**. optimized structure and **h**. band structure of C_3N monolayer. The unit cell is shown by the red dashed line; **i**. top and side view of the atomic structure of monolayer C_4N. The black dashed lines show the 3×3×1 supercell of monolayer C_4N; **j**. Electronic band structures and **k**. PDOS of the unit cell of a pristine C_4N monolayer; **l**. top (upper) and side (lower) view of the atomic structure of C_5N monolayer. The gray and blue balls represent C atoms and N atoms, respectively; **m**. band structure and **n**. density of states (DOS) of C_5N monolayer obtained from HSE06 calculations. The black, red, and blue lines denote the total DOS of C_5N, the partial DOS of C atoms, and the partial DOS of N atoms, respectively.

The C_3N_4 stoichiometry is however the most studied one; it is composed of continuously repeated heptazine units (tri-s-triazine) having planar sp^2-hybridized conjugation structures held together by van de Waals forces. It has an inter-layer distance of about 0.324 nm and a 2.7 eV band-gap (Fig. 2–9e), which can be easily tuned as reported above or by simply inducing buckling (Fig. 2–9f). The structure of C_3N contains only six-membered rings with no pores. It has a high structural stability, superior thermal conductivity (Fig. 2–9g), an orbital gap of ≈ 2.7 eV and an indirect bandgap of 0.39 eV (Fig. 2–9h). The C_4N structure is made of sp^3 hybridized sites and shows a band structure similar to that of graphene (Fig. 2–9i,j), which makes it a semiconductor which displays a narrow bandgap (Fig. 2–9k). Finally, C_5N is the most recently reported graphitic N-based carbon nitride, made of sp^3 hybridized carbon atoms. However, it contains two rings of different sizes (Fig. 2–9l). The analysis of the band structure shows that the Fermi level is located below the valence-band maximum, which suggests it would be metallic and display superior conductivity with respect to the other carbon nitrides (Fig. 2–9m,n). Overall these data illustrate the wide diversity of structures, electronic properties and crystal packing of carbon nitride materials.

In recent years, both experimental[155,156] and theoretical[157–160] works have been published highlighting the ability and describing the mechanisms involving *g*-C_3N_4 as catalyst in H_2 production through the splitting of water. In addition, some efforts have been directed towards the use of *g*-C_3N_4 as a catalyst that artificially mimics photosynthesis in plants for the CO_2 conversion into hydrocarbon fuels when combined with a series of metal oxides[161,162]; however there is no consensus as to the mechanistic role of each species in the association. Du *et al*. have theoretically shown a considerable decrease in the rate-determining barriers when supporting single atom Pd/Pt on *g*-C_3N_4[163]. This was a further confirmation of what Mao *et al*. discovered, *i.e*. urea-based *g*-

CN catalyzes CO_2 conversion into CH_3OH and C_2H_5OH, in 15.1 and 10.8 μmol after 12h of visible light irradiation, respectively[164]. There has been a debate about the mechanism of CO_2 reduction, especially involving the two conformations that the 2D material can have, *i.e*. planar or corrugated and Azofra *et al*. carried out DFT studies at the GGA/PBE level of theory to shed light on the debate currently taking place[165]. They found that corrugated *g*-CN is stabilized by 2.91 eV with respect to the planar one and that corrugation both decreases the nitrogen lone-pair repulsions and generates anchoring sites for CO_2 absorption, by deepening the π–holes. In relation to this study, Melissen *et al*. demonstrated that the B3LYP functional, in conjunction with the Grimme D3 dispersion and a triple zeta (ζ) basis function, is appropriate for describing the basic thermochemistry of *g*-$C_xN_yH_z$ syntheses[166]. Provided that either triazine- or heptazine-based *g*-CN are possible structural units, two final *g*-C_3N_4 systems are formed, often being corrugated or "buckled"[165].

As mentioned above, carbon nitride is sometimes doped with certain metallic elements not only to reduce its electronic band-gap but also to make some reactions possible. Guo *et al*. reported on a DFT study of the carbon dioxide reduction-reaction (CRR) performed on the *g*-CN surface previously doped with either nickel, iron or cobalt[166]. The structures of the electrocatalysts, the CO_2 adsorption configurations and the CO_2 reduction mechanisms showed that CO_2 can be chemically adsorbed on Co-C_3N_4 and Fe-C_3N_4, but is only physically adsorbed on Ni-C_3N_4. This was also analyzed at the GGA/PBE level of theory, with the addition of a Projector-Augmented Wave (PAW) pseudopotential to describe the ionic cores.

Finally, in relation to the important topic of the water-splitting reaction, another DFT study predicts that all classes of carbon nitride cluster models considered by Butchosa *et al*. are thermodynamically able to reduce protons and oxidize water[157]. In that combined DFT/TD-DFT

study, the authors calculated the theoretical optical spectra, which were then compared to the experimental ones. The B3LYP/DZP level of theory was used for both the ground-state optimizations and the excited-states calculations performed on frozen-core structures.

2.6 Conclusions

As it was discussed in this chapter, carbon nitride is an extremely versatile material that can be used in many catalytic contexts. Thanks to its numerous phases and geometric arrangements (triazine, melon), it shows different polymorphs with peculiar structural features (compressibility, elasticity, linearity, corrugation). Graphitic carbon nitride (*g*-C_3N_4) is a metal-free material with a band-gap of ≈ 2.7 eV which allows interaction with visible light, unlike other extensively used metallic semiconductors (TiO_2). Elemental doping (with non-metals or metals) can modulate its band-gap, enabling an even greater interaction with light. This is the reason why it is used in heterogeneous photocatalysis, for reactions like the splitting of water, CO_2 reduction and other general H_2 production reactions. These are however complex processes usually hard to characterize with classical experimental tools. Complementary to experiment, Density Functional theory (DFT) is a powerful approach that can shed light on the reaction mechanisms or electronic properties of materials. Theoretical calculations can yield the electronic structure of carbon nitride materials, along with their band-gap and eventually reaction energy profiles. In this context, the modelling of the excited states is also very important because the electron transfer processes involved in such reactions can be described (*vide* water-splitting modelling with TD-DFT). It is therefore with Density Functional Theory that we decided to model the two reactions shown in chapter 1, focusing on the interaction between the catalyst and the substrates and on the electron transfer processes involving them.

References

[1] P. F. McMillan, V. Lees, E. Quirico, G. Montagnac, A. Sella, B. Reynard, P. Simon, E. Bailey, M. Deifallah, F. Corà, *J. Solid State Chem*., 182, (**2009**), 2670–2677.

[2] D. Vidyasagar, T. Bhoyar, G. Singh, A. Vinu, *Macromol. Rapid. Commun*., 42, (**2021**), 2000676, 1–6.

[3] E. Alwin, K. Kočí, R. Wojcieszak, M. Zieliński, M. Edelmannová, M. Pietrowski, *Materials*, 13, (**2020**), 2756.

[4] A. Thomas, A. Fischer, F. Göttmann, M. Antonietti, J. O. Müller, R. Schlögel, J. M. Carlsson, *J. Mater. Chem*., 18, (**2008**), 4893–4908.

[5] X. C. Wang, K. Maeda, A. Thomas, K. Takanabe, G. Xin, J. M. Carlsson, K. Domen, M. Antonietti, *Nat. Mater*., 8, (**2009**), 76.

[6] Y. Wang, X. C. Wang, M. Antonietti, *Angew. Chem. Int. Ed*., 51, (**2012**), 68.

[7] X. C. Yang, K. Maeda, X. F. Chen, K. Takanabe, K. Domen, Y. D. Hou, X. F. Fu, M. Antonietti, *J. Am. Chem. Soc*., 131, (**2009**), 1680.

[8] J. Lin, Z. Pan, X. Wang, *ACS Sustainable Chem. Eng*., (**2014**), 2, 353–358.

[9] S. C. Yan, Z. S. Li, Z. G. Zou, *Langmuir*, 25, (**2009**), 10397.

[10] K. Maeda, X. Wang, Y. Nishihara, D. Lu, M. Antonietti, K. Domen, *J. Phys. Chem. C*, 113, (**2009**), 4940.

[11] H. Ji, F. Chang, X. Hu, W. Qin, J. Shen, *Chem. Eng. J*., 218, (**2013**), 183.

[12] G. Zhang, J. Zhang, M. Zhang, X. Wang, *J. Mater. Chem*., 22, (**2012**), 8083.

[13] F. Dong, Z. Wang, Y. Sun, W. K. Ho, H. Zhang, *J. Coll. Int. Sci*., 401, (**2013**), 70.

[14] A. B. Jorge, D. J. Martin, M. T. S. Dhanoa, A. S. Rahman, N. Makwana, J. Tang, A. Sella, F. Corà, S. Firth, J. A. Darr, P. F. McMillan, *J. Phys. Chem. C*, 117, (**2013**), 7178.

[15] H. Montigaud, B. Tanguy, G. Demazeau, I. Alves, S. Courjault, *J. Mater. Sci*., 35, (**2000**), 2547.

[16] Y. Gu, L. Chen, L. Shi, J. Ma, Z. Yang, Y. Qian, *Carbon*, 41, (**2003**), 2674.

[17] B. Jürgens, E. Irran, J. Senker, P. Kroll, H. Müller, W. Schnick, *J. Am. Chem. Soc*., 125, (**2003**), 10288.

[18] B. V. Lotsch, M. Döblinger, J. Sehnert, L. Seyfarth, J. Senker, O. Öckler, W. Schnick, *Chem–Eur. J*., 13, (**2007**), 4969.

[19] G. Filippini, F. Longobardo, L. Forster, A. Criado, G. Di Carmine, L. Nasi, C. D'Agostino, M. Melchionna, P. Fornasiero, M. Prato, *Sci. Adv*., 6, (**2020**).

[20] T. S. Miller, A. D'Aleo, T. Suter, A. E. Aliev, A. Sella, P. F. McMillan, *Z. Anorg. Allg. Chem*., 643, (**2017**), 1572–1580.

[21] H. Irving, *Sci*. *Prog*., 30, (**1935**), 62–66.

[22] T. L. Davies, *J*. *Chem*. *Educ*., 17, (**1940**), 268.

[23] T. S. Miller, A. B. Jorge, T. M. Suter, A. Sella, F. Corà, P. F. McMillan, *Phys*. *Chem*. *Chem*. *Phys*., 19, (**2017**), 15613–15638.

[24] G. A. Siller, N. Severin, S. Y. Chong, T. Björkmann, R. G. Palgrave, A. Laybourne, M. Antonietti, Y. Z. Khimyak, A. V. Krasheninnikov, J. P. Rabe, U. Kaiser, A. I. Cooper, A. Thomas, *Angew*. *Chem*. *Int*. *Ed*., 53, (**2014**), 7450.

[25] H. Pan, *J*. *Phys*. *Chem*. *C*., 118, (**2014**), 9318–9323.

[26] Y. Zheng, J. Liu, J. Liang, M. Jaroniec, S. Z. Qiao, *Energy Environ*. *Sci*., 5, (**2012**), 6717–6731.

[27] A. H. Reshak, S. A. Khan, S. Auluck, *RSC Adv*., 4, (**2014**), 11967.

[28] A. H. Reshak, S. A. Khan, S. Auluck, *RSC Adv*., 4, (**2014**), 6957–6964.

[29] M. Tahir, C. Cao, F. K. Butt, F. Idrees, N. Mahmood, I. Aslam, Z. Ali, M. Tanvir, M. Rizwan, T. Mahmood, *J*. *Mater*. *Chem*. *A*., 1, (**2013**), 13949.

[30] J. R. Holst, E. G. Gillan, *J*. *Am*. *Chem*. *Soc*., 130, (**2008**), 7373.

[31] Y. Guo, W. A. Goddard, *Chem*. *Phys*. *Lett*., 237, (**1995**), 72.

[32] J. L. Corkill, M. L. Cohen, *Phys*. *Rev*. *B*: *Condens*. *Matter*. *Phys*., 50, (**1994**), 17622.

[33] A. H. Reshak, *RSC Adv*., 4, (**2014**), 6337.

[34] D. M. Teter, R. J. Hemley, *Science*, 271, (**1996**), 53.

[35] E. Kroke, M. Schwarz, *Coord*. *Chem*. *Rev*., 248, (**2004**), 493–532.

[36] A. Y. Liu, M. L. Cohen, *Science*, 245, (**1989**), 841.

[37] A. Y. Liu, M. L. Cohen, *Phys*. *Rev*. *B*, 41, (**1990**), 10727.

[38] C. M. Sung, M. Sung, *Mater*. *Chem*. *Phys*., 43, (**1996**), 1.

[39] M. L. Cohen, *Phys*. *Rev*. *B*, 32, (**1985**), 7988.

[40] C. J. Pickard, A. Salamat, M. J. Bojdys, R. J. Needs, P. F. McMillan, *Phys*. *Rev*. *B*, 94, (**2016**), 094104.

[41] J. Wen, J. Xie, X. Chen, X. Li, *Appl*. *Surf*. *Sci*., 391, (**2017**), 72–123.

[42] A. J. Bard, M. A. Fox, *Acc*. *Chem*. *Res*., 28, (**1995**), 141–145.

[43] A. Torres-Pinto, M. J. Sampaio, C. G. Silva, J. L. Faria, A. M. T. Silva, *Catalysts*, 9, (**2019**), 990.

[44] Z. Li, D. Huang, C. Zhou, W. Xue, L. Lei, R. Deng, Y. Yang, S. Chen, W. Wang, Z. Wang, *Chem*. *Eng*. *Journal*, 382, (**2020**), 122657.

[45] V. Hasija, P. Raizada, A. Sudhaik, K. Sharma, A. Kumar, P. Singh, S. B. Jonnalagadda, V. K. Thakur, *Appl. Mat. Today*, 15, (**2019**), 494–524.

[46] J. Barrio, M. Volokh, M. Shalom, *J. Mater. Chem. A*, 8, (**2020**), 11075.

[47] H. Sun, G. Zhou, Y. Wang, A. Suvorova, S. Wang, *ACS Appl. Mater. Interfaces*, 6, 19, (**2014**), 16745–16754.

[48] Y-Y. Han, X-L. Lu, S-F. Tang, X-P. Yin, Z-W. Wei, T-B. Lu, *Adv. Energy Mater.*, 8, (**2018**), 1702992.

[49] J. Liu, Y. Liu, N. Liu, Y. Han, X. Zhang, H. Huang, Y. Lifshitz, S-T. Lee, J. Zhong, Z. Kang, *Science*, 347, (**2015**), 970.

[50] H. Ou, P. Yang, L. Lin, M. Anpo, X. Wang, *Angew. Chem. Int. Ed.*, 56, (**2017**), 10905.

[51] K. Srinivasu, B. Modak, S. K. Ghosh, *J. Phys. Chem. C*, 118, 46, (**2014**), 26479–26484.

[52] L. Cheng, H. Zhang, X. Li, J. Fan, Q. Xiang, *Small*, 17, (**2021**), 2005231.

[53] W. Che, W. Cheng, T. Yao, F. Tang, W. Liu, H. Su, Y. Huang, Q. Liu, J. Liu, F. Hu, Z. Pan, Z. Sun, S. Wei, *J. Am. Chem. Soc.*, 139, (**2017**), 3021–3026.

[54] Y. Hou, Z. Wen, S. Cui, X. Feng, J. Chen, *Nano Lett.*, 16, (**2016**), 2268–2277.

[55] P. Luan, Q. Meng, J. Wu, Q. Li, X. Zhang, Y. Zhang, L-A. O'Dell, S. R. Raga, J. Pringle, J. C. Griffith, C. Sun, U. Bach, J. Zhang, *ChemSusChem*, 13, (**2020**), 328–333.

[56] H. Staruk, P. Praus, *Catalysts*, 10, (**2020**), 1119.

[57] A. E. A. Aboubakr, W. M. A. El Rouby, M. D. Khan, N. Revrapasadu, P. Millet, *Solar Energy Mater. Solar Cells*, 232, (**2021**), 111326.

[58] Q. Lu, A. Abdelgawad, J. Li, K. Eid, *Int. J. Mol. Sci.* 23, (**2022**), 15129.

[59] Y. Jiao, M. Liu, J. Qin, Y. Li, J. Wang, Z. He, Z. Li, *J. Coll. Int. Sci.*, 608, (**2022**), 1432–1440.

[60] X. Han, A. Yuan, C. Yao, F. Xi, J. Liu, X. Dong, *J. Mater. Sci.*, 54, (**2019**), 1593–1605.

[61] G. Elmaci, A. S. Ertürk, M. Sevim, Ö. Metin, *J. Hydrogen Ener.*, 44, (**2019**), 17995–18006.

[62] H. Zhang, W. Tian, L. Zhou, H. Sun, M. Tade, S. Wang, *Appl. Catal. B Environ.*, 223, (**2018**), 2–9.

[63] Y. Hong, E. Liu, J. Shi, X. Lin, L. Sheng, M. Zhang, L. Wang, *J. Hydrogen Ener.*, 44, (**2019**), 7194–7204.

[64] Y. Zhang, A. Thomas, M. Antonietti, X. Wang, *J. Am. Chem. Soc.*, 131, (**2008**), 50–51.

[65] J. Fung, B. Chang, Y. Tian, F. Xi, X. Dong, *J. Mater. Chem.*, 1, (**2013**), 3083–3090.

[66] A. E. A. Aboubakr, W. M. A. El Rouby, M. D. Khan, N. Revrapasadu, P. Millet, *Solar Energy Mater. Solar Cells*, 193, (**2019**), 403–412.

[67] H. Zhang, W. Tian, X. Duan, H. Sun, Y. Shen, G. Shao, S. Wang, *Nanoscale*, 12, (**2020**), 6937–6952.

[68] Y. F. Li, S. Wang, W. Chang, L. H. Zhang, Z. S. Wu, S. Y. Song, Y. Xing, *J. Mater. Chem. A*, 7, (**2019**), 20640–20648.

[69] C. Y. Su, Y. Z. Zhou, L. L. Zhang, X. H. Yu, S. Gao, X. J. Sun, C. Cheng, Q. Q. Liu, J. Yang, *Ceram. Int.*, 46, (**2020**), 8444–8451.

[70] H. L. Li, C. Jin, Z. Y. Wang, Y. Y. Liu, P. Wang, Z. K. Zheng, M. H. Whangbo, L. Z. Kou, Y. J. Li, Y. Dai, *Chem. Eng. J.*, 369, (**2019**), 263–271.

[71] C. Tang, M. Cheng, C. Lai, L. Li, X. Yang, L. Du, G. Zhang, G. Wang, L. Yang, *Coord. Chem. Rev.*, 474, (**2023**), 214846.

[72] M. A. Mohamed, M. F. M. Zain, L. J. Minggu, M. B. Kassim, N. A. S. Amin, W. N. W. Salleh, M. N. I. Salehmin, M. F. M. Nasir, Z. A. M. Hir, *Appl. Catal. B*, 236, (**2018**), 265–279.

[73] L. Jiang, X. Yuan, G. Zeng, J. Liang, Z. Wu, H. Yu, D. Mo, H. Wang, Z. Xiao, C. Zhou, *J. Colloid. Int. Sci.*, 536, (**2019**), 17–29.

[74] Z. Mo, X. Zhu, Z. Jiang, Y. Song, D. Liu, H. Li, X. Wang, Y. She, Y. Lei, S. Yuan, H. Li, L. Song, Q. Yan, H. Xu, *Appl. Catal.* B, 256, (**2019**), 117854.

[75] H. Wang, Y. Bian, J. Hu, L. Dai, *Appl. Catal. B*, 238, (**2018**), 592–598.

[76] P. Wang, C. Guo, S. Hou, X. Zhao, L. Wu, Y. Pei, Y. Zhang, J. Gao, J. Xu, *J. Alloy. Compd.* 769, (**2018**), 503–511.

[77] Y. Bai, Y. Zheng, Z. Wang, Q. Hong, S. Liu, Y. Shen, Y. Zhang, *New J. Chem.*, 45, (**2021**), 11846.

[78] H. Pan, Y-.W. Zhang, V. B. Shenoy, H. Gao, *ACS Catal.*, 1, (**2011**), 99–104.

[79] G. Ding, W. Wang, T. Jiang, B. Han, H. Fan, G. Yang, *ChemCatChem*, 5, (**2013**), 192–200.

[80] B. Yue, Q. Li, H. Iwai, T. Kako, J. Ye, *Adv. Mater.*, 12, (**2011**), 034401.

[81] S. Tonda, S. Kumar, S. Kandula, V. Shnaker, *J. Mater. Chem. A*, 2, (**2014**), 6772–6780.

[82] X. Ye, Y. Cui, X. Qiu, X. Wang, *Appl. Catal. B*, (**2014**), 152–153, 383–389.

[83] X. Wang, X. Chen, A. Thomas, X. Fu, M. Antonietti, *Adv. Mater.*, 21, (**2009**), 1609–1612.

[84] Z. Ding, X. Chen, M. Antonietti, X. Wang, *ChemSusChem*, 4, (**2011**), 274–281.

[85] H. Gao, S. Yan, J. Wang, Z. Zou, *Dalton Trans.*, 43, (**2014**), 8178–8183.

[86] J. Zhao, L. Ma, H. Wang, Y. Zhao, J. Zhang, S. Hu, *Appl. Surf. Sci.*, 332, (**2015**), 625–630.

[87] J. Zhang, S. Hu, Y. Wang, *RSC Adv.*, 4, (**2014**), 62912–62919.

[88] S. Hu, F. Li, Z. Fan, F. Wang, Y. Zhao, Z. Lv, *Dalton Trans.*, 44, (**2015**), 1084–1092.

[89] T. Xiong, W. Chen, Y. Zhang, F. Dong, *ACS Catal.*, 6, (**2016**), 2462–2472.

[90] M. Wu, J-.M. Yan, X-.N. Tang, M. Zhao, Q. Jiang, *ChemSusChem*, 7, (**2014**), 2654–2658.

[91] M. Zhang, X. Bai, D. Liu, J. Wang, Y. Zhu, *Appl. Catal. B*, 164, (**2015**), 77–81.

[92] Y. Gai, J. Li, S-.S. Li, J-.B. Xia, S-.H. Wei, *Phys. Rev. Lett.*, 102, (**2009**), 036402.

[93] X. Chen, S. Shen, L. Guo, S. S. Mao, *Chem. Rev.*, 110, (**2010**), 6503.

[94] Z. Chen, P. Sun, B. Fan, Q. Liu, Z. Zhang, X. Fang, *Appl. Catal. B Environ.*, 170–171, (**2015**), 10–16.

[95] J. Zhang, M. Zhang, S. Lin, X. Fu, X. Wang, *Journal of Catalysis*, 310, (**2014**), 24–30.

[96] W-.J. Ong, L-.L. Tan, Y-.H. Ng, S-.T. Jong, S-.P. Chai, *Chem. Rev.*, 116, (**2016**), 7159–7329.

[97] H. Wang, L. Zhang, Z. Chen, J. Hu, S. Li, Z. Wang, J. Liu, X. Wang, *Chem. Soc. Rev.*, 43, (**2014**), 5234–5244.

[98] Y. Wang, Q. Wang, X. Zhan, F. Wang, M. Safdar, J. He, *Nanoscale*, 5, (**2013**), 8326–8339.

[99] J. Zhang, M. Zhang, R-.Q. Sun, X. Wang, *Angew. Chem., Int. Ed.*, 51, (**2012**), 10145–10149.

[100] F. Su, S. C. Mathew, G. Lipner, X. Fu, M. Antonietti, S. Blechert, X. Wang, *J. Am. Chem. Soc.*, 132, (**2010**), 16299.

[101] X. Lu, Q. Wang, D. Cui, *J. Mater. Sci. Technol.*, 26, (**2010**), 925.

[102] N. Yang, G. Li, W. Wang, X. Yang, W. F. Zhang, *J. Phys. Chem. Solids*, 72, (**2011**), 1319.

[103] M. Bledowski, L. Wang, A. Ramakrishnan, O. V. Khavryuchenko, V. D. Khavryuchenko, P. C. Ricci, J. Strunk, T. Cremer, C. Kolbeck, R. Beranek, *Phys. Chem. Chem. Phys.*, 13, (**2011**),

[104] B. Chai, T. Peng, J. Mao, K. Lia, L. Zan, *Phys. Chem. Chem. Phys.*, 14, (**2012**), 16745.

[105] X. Zhou, B. Jin, L. Li, F. Peng, H. Wang, H. Yu, Y. Fang, *J. Mater. Chem.*, 22, (**2012**), 17900.

[106] K. Kondo, N. Murakami, C. Ye, T. Tsubota, T. Ohno, *Appl. Catal. B*, 142–143, (**2013**), 362.

[107] S. Kumar, T. Surendar, A. Baruah, V. Shanker, *J. Mater. Chem. A*, 1, (**2013**), 5333.

[108] L. Ge, C. Han, J. Liu, *Appl. Catal. B*, 108–109, (**2011**), 100.

[109] Y. Wang, X. Bai, C. Pan, J. Heb, Y. Zhu, *J. Mater. Chem.*, 22, (**2012**), 11568.

[110] S. Zhang, Y. Yang, Y. Guo, W. Guo, M. Wang, Y. Guo, M. Huo, *J. Hazard. Mater.*, 261, (**2013**), 235.

[111] J. Fu, Y. Tian, B. Chang, F. Xi, X. Dong, *J. Mater. Chem.*, 22, (**2012**), 21159.

[112] L. Ye, J. Liu, Z. Jiang, T. Peng, L. Zan, *Appl. Catal. B*, 1, (**2013**), 142–143.

[113] L. Ge, F. Zuo, J. Liu, Q. Ma, C. Wan, D. Sun, L. Bartels, P. Feng, *J. Phys. Chem. C*, 116, (**2012**), 13708.

[114] J. Fu, B. Chang, Y. Tiaz, F. Xi, X. Dong, *J. Mater. Chem. A*, 1, (**2013**), 3083.

[115] F. Yang, V. Kuznietsov, M. Lublow, C. Merschjann, A. Steigert, J. Klaer, A. Thomas, T. Schedel-Niedrig, *J. Mater. Chem. A*, 1, (**2013**), 6407.

[116] S. Ye, L.-G. Qiu, Y.-P. Yuan, Y.-J. Zhu, J. Xia, J.-F. Zhu, *J. Mater. Chem. A*, 1, (**2013**), 3008.

[117] X. Zhou, B. Jin, R. Chen, F. Peng, Y. Fang, *Mater. Res. Bull.*, 48, (**2013**), 1447.

[118] Q. Li, B. Yue, H. Iwai, T. Kako, J. Ye, *J. Phys. Chem. C*, 114, (**2010**), 4100.

[119] L. Ge, C. Han, X. Xiao, L. Guo, *Int. J. Hydrogen Energy*, 38, (**2013**), 6960.

[120] X. Wang, G. Chen, C. Zhou, Y. Yu, G. Wang, Eur. *J. Inorg. Chem.*, 2012, (**2012**), 1742.

[121] X. Xu, G. Liu, C. Randorn, J. T. S. Irvine, *Int. J. Hydrogen Energy*, 36, (**2011**), 13501.

[122] H. W. Kang, S. N. Lim, D. Song, S. B. Park, *Int. J. Hydrogen Energy*, 37, (**2012**), 11602.

[123] S. C. Yan, S. B. Lv, Z. S. Li, Z. G. Zou, *Dalton Trans.*, 39, (**2010**), 1488.

[124] Y. Zang, L. Li, Y. Zuo, H. Lin, G. Li, X. Guan, *RSC Adv.* 3, (**2013**), 13646.

[125] Y. Wang, R. Shi, J. Lin, Y. Zhu, *Energy Environ. Sci.*, 4, (**2011**), 2922.

[126] L. Sun, X. Zhao, C.-J. Jia, Y. Zhou, X. Cheng, P. Li, L. Liu, W. Fan, *J. Mater. Chem.*, 22, (**2012**), 23428.

[127] Y. Markushyna, C. A. Smith, A. Savateev, *Eur. J. Org. Chem.*, (**2019**), 1294–1309.

[128] L. Möhlmann, M. Baar, J. Rieß, M. Antonietti, X. Wang, S. Blechert, *Adv. Synth. Catal.*, 354, (**2012**), 1909–1913.

[129] C. Cavedon, A. Madani, P. H. Seeberger, B. Pieber, *Org. Lett.*, 21, (**2019**), 5331–5334.

[130] B. Pieber, J. A. Malik, C. Cavedon, S. Gisbertz, A. Savateev, D. Cruz, T. Hell, G. Zhang, *Angew. Chem. Int. Ed.*, 58, (**2019**), 9575–9580.

[131] B. Pieber, M. Shalom, M. Antonietti, P. H. Seeberger, K. Gilmore, *Angew. Chem. Int. Ed.*, 57, (**2018**), 9976–9979.

[132] I. Ghosh, J. Khamrai, A. Savateev, N. Shlapakov, M. Antonietti, B. König, *Science*, 365, (**2019**), 360–366.

[133] X. Sci, T. Song, Q. Li, X. Guo, Y. Yang, *Org. Lett.*, 24, 47, (**2022**), 8724–8728.

[134] S. Mazzanti, B. Kurpil, B. Pieber, M. Antonietti, A. Savateev, *Nature Comm.*, 11, (**2020**), 1387.

[135] Y. Cai, Y. Tang, L. Fan, Q. Lefebvre, H. Hou, M. Rueping, *ACS Catal.*, 8, (**2018**), 9471–9476.

[136] D. A. Nagib, D. W. MacMillan, *Nature*, 480, (**2011**), 224–228.

[137] M. Baar, S. Blechert, *Chem. Eur. Joc.*, 21, (**2015**), 526–530.

[138] J. Twilton, C. C. Le, P. Zhang, M. H. Shaw, R. W. Evans, D. W. MacMillan, *Nat. Chem. Rev.*, 1, (**2017**), 0052.

[139] D. Ravelli, M. Fagnoni, A. Albini, *Chem. Soc. Rev.*, 42, (**2013**), 97–113.

[140] D. A. Nicewicz, D. W. MacMillan, *Science*, 322, (**2008**), 77–80.

[141] J. M. R. Narayanam, J. W. Tucker, C. R. J. Stephenson, *J. Am. Chem. Soc.*, 131, (2009), 8756–8757.

[142] M. A. Ischay, M. E. Anzovino, J. Du, T. P. Yoon, *J. Am. Chem. Soc.*, 130, (**2008**), 12886–12887.

[143] J. Twilton, C. C. Le, P. Zhang, M. H. Shaw, R. W. Evans, D. W. C. MacMillan, *Nat. Chem. Rev.*, 1, (**2017**), 0052.

[144] N. A. Romero, D. A. Nicewicz, *Chem. Rev.*, 116, (**2016**), 10075–10166.

[145] M. Marchi, G. Gentile, C. Rosso, M. Melchionna, P. Fornasiero, G. Filippini, M. Prato, *ChemSusChem*, 15, (**2022**), e202201094.

[146] N. A. Till, L. Tian, Z. Dong, G. D. Scholes, D. W. MacMillan, *J. Am. Chem. Soc.*, 142, (**2020**), 15830–15841.

[147] M. Kudisch, C-. H. Lim, P. Thordarson, G. M. Miyake, *J. Am. Chem. Soc.*, 141, (**2019**), 19479–19486.

[148] E. B. Corcoran, M. T. Pirnot, S. Lin, S. D. Dreher, D. A. Di Rocco, I. W. Davies, S. L. Buchwald, D. W. MacMillan, *Science*, 353, (**2016**), 279–282.

[149] N. A. Till, L. Tian, Z. Dong, G. D. Scholes, D. W. MacMillan, *J. Am. Chem. Soc.*, 142, (**2020**), 15830–15841.

[150] M. Kudisch, C-. H. Lim, P. Thordarson, G. M. Miyake, *J. Am. Chem. Soc.*, 141, (**2019**), 19479–19486.

[151] O. S. Wenger, *Chem. Eur. J.*, 27, (**2021**), 2270–2278.

[152] S. Gisbertz, S. Reischauer, B. Pieber, *Nature Catal.*, 3, (**2020**), 611–620.

[153] C. Rosso, S. Gisbertz, J. D. Williams, H. P. L. Gemoets, W. Debrouwer, B. Pieber, C. O. Kappe, *React. Chem. Eng.*, 5, (**2020**), 597.

[154] D. Adekoya, S. Qian, X. Gu, W. Wen, D. Li, J. Ma, S. Zhang, *Nano-Micro Lett.*, 13, (**2021**).

[155] K. Maeda, X. Wang, Y. Nishihara, D. Lu, M. Antonietti, K. Domen, *J. Phys. Chem. C.*, 113, (**2009**), 4940–4947.

[156] S. Martha, A. Nashim, K. M. Parida, *J. Mater. Chem. A*, 1, (**2013**), 7816–7824.

[157] C. Butchosa, P. Guiglion, M. A. Zweijnenburg, *J. Phys. Chem. C*, 118, (**2014**), 24833–24842.

[158] K. Srinivasu, B. Modak, S. K. Ghosh, *J. Phys. Chem. C*, 118, (**2014**), 26479–26484.

[159] J. Wirth, R. Neumann, M. Antonietti, P. Saalfrank, *Phys. Chem. Chem. Phys.*, 16, (**2014**), 15917–15926.

[160] G. Gao, Y. Jiao, F. Ma, Y. Jiao, E. R. Waclawik, A. Du, *J. Catal.*, 332, (**2015**), 149–155.

[161] Y. He, L. Zhang, B. Teng, M. Fan, *Environ*. *Sci*. *Technol*., 49, (**2015**), 649–656.

[162] W. Yu, D. Xu, T. Peng, *J*. *Mater*. *Chem*. *A*, 3, (**2015**), 19936–19947.

[163] G. Gao, Y. Jiao, E. R. Waclawik, A. Du, *J*. *Am*. *Chem*. *Soc*., 138, (**2016**), 6292–6296.

[164] J. Mao, T. Peng, X. Zhang, K. Li, L. Ye, L. Zan, *Catal*. *Sci*. *Tech*., 3, (**2013**), 1253–1260.

[165] L. M. Azofra, D. R. MacFarlane, C. Sun, *Phys*. *Chem*. *Chem*. *Phys*., 18, (**2016**), 18507–18514.

[166] S. T. A. G. Melissen, S. N. Steinmann, T. Le Bahers, P. Sautet, *J*. *Phys*. *Chem*. *C*, 120, (**2016**), 24542–24550.

Chapter 3: Modelling methodology

Density Functional Theory (DFT) plays a crucial role in the determination of molecular properties such as structures, geometrical parameters, electronic properties, and formation energies. In this work a combined experimental and theoretical approach is followed in order to provide a deep insight into the role of functionalized carbon nitride as the photocatalyst for the two classes of organic reactions we focused on. The first approach pertains all syntheses and characterizations carried out in our laboratory, whereas the second one is using theoretical models simulating the reaction mechanisms to provide data detailed molecular-scale description in support of the experiments. Before describing the computational protocols applied for our studies, the basic concepts of Density Functional Theory will be reminded.

3.1 The Hohenberg-Kohn theorems

DFT is based on the Hohenberg–Kohn theorems, which describe the existence of a one-to-one correspondence between the ground-state electron density and the external potential containing the electron-nuclei attraction and the existence of a variational formalism for electron densities analogous to the Raleigh–Ritz principle for wavefunctions[1]. The first Hohenberg-Kohn theorem (HK-I) states that the external potential $v(\vec{\boldsymbol{r}}_i)$ and the number of electrons *N* determine the solutions of the many-electron Schrödinger equation and, for non-degenerate ground states, there exists a one-to-one mapping between $v(\vec{\boldsymbol{r}}_i)$ and the ground-state density $\rho_0(\vec{\boldsymbol{r}})$. The abovementioned quantities are:

$$\rho_0(\vec{\boldsymbol{r}}) = N \cdot \sum_{all\ m_s} \int \dots \int |\Psi(\vec{\boldsymbol{r}}_1, \vec{\boldsymbol{r}}_2, \dots, \vec{\boldsymbol{r}}_N, m_{s1}, m_{s2}, \dots, m_{sn}|^2 d\vec{\boldsymbol{r}}_1 d\vec{\boldsymbol{r}}_2 \dots d\vec{\boldsymbol{r}}_N \qquad \text{(Eq. 1)}$$

$$v(\vec{\boldsymbol{r}}_i) = -\sum_\alpha \frac{Z_\alpha}{\vec{\boldsymbol{r}}_{i\alpha}} \qquad \text{(Eq. 2)}$$

where $\rho_0(\vec{\boldsymbol{r}})$ in Eq.1 is the one-particle probability density at its ground state, indicated by the zero subscript next to ρ. This latter is given by the integral of the square modulus of the spin-orbit

wavefunction, having $\vec{\boldsymbol{r}}_N$ spatial coordinates and $m_{s,n}$ spin coordinates. In Eq. 2, $v(\vec{\boldsymbol{r}}_i)$ is the external potential given by the sum over all nuclei of positive charge Z_α at distance $\vec{\boldsymbol{r}}_{i,\alpha}$ with the *i*-th electron. This is an attractive interaction given by the negative sign of the sum. The expression of $v(\vec{\boldsymbol{r}}_i)$ comes from the Hamiltonian operator applied to a wavefunction of a given *N*-electron system as follows:

$$\hat{\mathrm{H}}_{\mathrm{el.}}\Psi_{\mathrm{el.}}(\vec{\boldsymbol{R}}, \vec{\boldsymbol{r}}) = E_{\mathrm{el.}}\Psi_{\mathrm{el.}}(\vec{\boldsymbol{R}}, \vec{\boldsymbol{r}}) \qquad \text{(Eq. 3)}$$

This is the Schrödinger time-independent equation, where the spatial coordinates of the nuclei $\vec{\boldsymbol{R}}$ have been parametrized due to the Born-Oppenheimer approximation, according to which nuclei are considered fixed in space[2]. The Hamiltonian operator in Eq. 3 is given by:

$$\hat{H}_{el.}(\vec{\boldsymbol{r}}_i) = \hat{T}_e + \hat{V}_{e,e} + \hat{V}_{e,n} = -\frac{1}{2}\sum_i \nabla_i^2 + \sum_j \sum_{i>j} \frac{1}{\vec{\boldsymbol{r}}_{ij}} + \sum_i v(\vec{\boldsymbol{r}}_i) \qquad \text{(Eq. 4)}$$

Eq. 4 shows the terms composing the Hamiltonian, *i.e.* the kinetic energy operator ($\hat{T}_e$), the repulsive potential operator between two electrons ($\hat{V}_{e,e}$) and the attractive potential operator between an electron and the nuclei ($\hat{V}_{e,n}$). The re-writing of the Hamiltonian in terms of the first Hohenberg-Kohn theorem can show the explicit dependence of the energy on the ground-state density, which will give an E_0 of the system. Combining the first Hohenberg-Kohn theorem with the expression of the *N*-electron Hamiltonian, the energy depends on the electron density as follows:

$$E_v[\rho_0] = \langle \Psi | T + V_{ee} + V_{ne} | \Psi \rangle = F[\rho_0] + \int v(\vec{\boldsymbol{r}})\rho_0(\vec{\boldsymbol{r}}) d\vec{\boldsymbol{r}} \qquad \text{(Eq. 5)}$$

which also shows a direct dependency of the energy on the external potential $v(\vec{\boldsymbol{r}}_i)$ defined in the theorem. In Eq. 5 a new term appears, *i.e.* $F[\rho_0] = T[\rho_0] + V_{ee}[\rho_0]$, that at this stage is still unknown because it depends only on the internal electron density, which is indeed a quantity to

compute. This indicates the repulsive electronic Hamiltonian of the system. The second term represents the application of the external potential to the electrons.

The second Hohenberg-Kohn theorem (HK-II) states that the true ground-state electron density $\rho_0(\vec{\boldsymbol{r}})$ minimizes the energy functional $E_v[\rho_{tr}]$, where $\rho_{tr}(\vec{\boldsymbol{r}})$ is a trial density that satisfies $\int \rho_{tr}(\vec{\boldsymbol{r}})d\vec{\boldsymbol{r}} = N$ and $\rho_{tr}(\vec{\boldsymbol{r}}) \geq 0$, for any given $\vec{\boldsymbol{r}}$, with the inequality such that $E_0 \leq E_v[\rho_{tr}]$. One could apply the variational theorem to obtain the latter value but $F[\rho_0]$ is an unknown quantity. Otherwise, the following quantity can be defined:

$$F[\rho_0] = \min_{\Psi \to \rho} \langle \Psi | T + V_{ee} | \Psi \rangle \qquad \text{(Eq. 6)}$$

where the minimization runs over all the normalized, antisymmetric *N*-particle wave functions (*i.e.* Slater determinants) yielding a given density $\rho(\vec{\boldsymbol{r}})$ and then:

$$E_0 = \min_{\rho} \{F[\rho_0] + \int dr\, v\,(\vec{\boldsymbol{r}})\rho_0(\vec{\boldsymbol{r}})\} \qquad \text{(Eq. 7)}$$

So, concisely, the sum of the kinetic and electron repulsion energies of an *N*-electron system is a *universal* functional of its density (universal in the sense that it is independent from the external potential). If this functional had been known, a variational resolution for the density and the energy would have been possible. Yet, no indications were given on how to calculate *E0* from $\rho_0(\vec{\boldsymbol{r}})$, nor on how to find $\rho_0(\vec{\boldsymbol{r}})$ without finding first the wave function.

3.2 The Kohn-Sham equations

Present-day DFT is almost exclusively based on the Kohn-Sham formalism[3], which corresponds to a formally exact dressed single-particle theory. In analogy to Hartree–Fock theory, the electrons

are treated as independent particles moving in the mean field of all others but now with the correlation included, by virtue of the exchange–correlation functional[4]. If a system of non-interacting electrons is introduced, a one-particle Hamiltonian can be defined as a sum extended over all electrons (Eq. 8). The $\varphi_i^{KS}(\vec{\boldsymbol{r}}_i)$ is the *i*-th element of the orthonormal set of fictitious functions defined by Kohn and Sham.

$$\sum_i \left(-\frac{1}{2}\nabla_i^2 + v_s(\vec{\boldsymbol{r}}_i)\right)\varphi_i^{KS}(\vec{\boldsymbol{r}}_i) = \sum_i \varepsilon_i^{KS}\varphi_i^{KS}(\vec{\boldsymbol{r}}_i) \qquad \text{(Eq. 8)}$$

These are the orbitals of the non-interacting system which yield a reference density $\rho_s(\vec{\boldsymbol{r}})$ defined as the sum of all square moduli of the Kohn-Sham orbitals, corresponding each to a single electron of the system (Eq. 10). The external potential acting on the fictitious one-electron solutions has the form of Eq. 9:

$$v_s(\vec{\boldsymbol{r}}_i) = v_{ext}(\vec{\boldsymbol{r}}_i) + \int \frac{\rho(\vec{\boldsymbol{r}}')}{|\vec{\boldsymbol{r}}-\vec{\boldsymbol{r}}'|}\, d\vec{\boldsymbol{r}}' + V_{xc}(\vec{\boldsymbol{r}}) \qquad \text{(Eq. 9)}$$

$$\rho_s(\vec{\boldsymbol{r}}) = \sum_i \left|\varphi_i^{KS}(\vec{\boldsymbol{r}}_i)\right|^2 \qquad \text{(Eq. 10)}$$

where $\int \frac{\rho(\vec{\boldsymbol{r}}')}{|\vec{\boldsymbol{r}}-\vec{\boldsymbol{r}}'|}\, d\vec{\boldsymbol{r}}'$ ($V_{\mathrm{e,e}}$) is the electron-electron potential and $v_{ext}(\vec{\boldsymbol{r}}_i)$ the nucleus-electron attractive potential. The introduction of the KS orbitals is useful because they are quantities now known by hypothesis, with which the electrons are conceived as non-interacting particles. In addition, the kinetic energy term depends on the fictitious density ($T_s[\rho]$, see Eq. 11) and the electron-electron potential can be considered as the classic Coulomb repulsive interaction (see Eq. 12).

$$T_s[\rho] =< \Psi_s|T|\Psi_s >= \sum_i \left\langle \varphi_i \left| -\frac{1}{2}\nabla_i^2 \right| \varphi_i \right\rangle \quad \text{(Eq. 11)}$$

$$V_{ee}[\rho] \approx J[\rho] = \frac{1}{2}\iint \frac{\rho(\vec{r}_i)\rho(\vec{r}_j)}{|\vec{r}_{ij}|} d\vec{r}_i d\vec{r}_j \quad \text{(Eq. 12)}$$

The advantage of Eq. 11 is that Ψ_s is given by a linear combination of all $\varphi_i^{KS}(\vec{r}_i)$ (known quantities), and that the kinetic energy reasonably approximates the actual one ($T_s[\rho] \approx T[\rho]$). $V_{ee}[\rho]$ is a term containing the self-interaction error (SIE) which is inevitable in DFT, as it cannot distinguish two particles. As the problem now addresses the reference density mentioned above, this will only be indicated as a general variable ρ from now on.

If one rewrites the unknown $F[\rho]$ as follows, a new quantity is defined:

$$F[\rho] = T[\rho] + V_{ee}[\rho] = T_s[\rho] + J[\rho] + (T[\rho] - T_s[\rho]) + (V_{ee}[\rho] - J[\rho]) \quad \text{(Eq. 13)}$$

We have added and subtracted $T_s[\rho]$ and $J[\rho]$, by which we can group together the new terms and define an exchange-correlation (xc) energy $E_{xc}[\rho] = T[\rho] - T_s[\rho] + V_{ee}[\rho] - J[\rho]$. So the potential-dependent energy from Eq. 5 can be conveniently rewritten as follows:

$$E_v[\rho] = T_s[\rho] + \int dr\, v(\vec{r})\rho(\vec{r}) + J[\rho] + E_{xc}[\rho] \quad \text{(Eq. 14)}$$

Variational minimization of Eq. 14 leads to the canonical Kohn-Sham expression. There are some advantages in the newly defined equation: electrons in atoms, molecules and solids can be regarded as independent particles, moving in an effective potential. This also means that the ground-state density of the interacting system can be found by solving N coupled 3-dimensional one-particle KS equations for the N orbitals and summing the squared of the lowest N occupied orbitals, $\rho(\vec{r}) = \sum_i |\varphi_i(\vec{r})|^2$. The $\varphi_i(\vec{r})$ orbitals can be regarded as the classic HF ones, with the only scope of providing guesses that, iteratively, will yield the real ground-state density. The challenge that still remains open at this stage is the $E_{xc}[\rho]$ term, for which no exact functional has been found. The

density present in that expression was determined at both the Local Density Approximation (LDA) and Generalized Gradient Approximation (GGA) levels of theory.

$$E_{xc}^{LDA}[\rho] = \int dr\, \rho(\vec{\boldsymbol{r}})\varepsilon_{xc}^{UEG}(\rho) \quad \text{(Eq. 15)}$$

$$E_{xc}^{GGA}[\rho] = \int dr\, \rho(\vec{\boldsymbol{r}})\varepsilon_{xc}^{GGA}(\rho, \nabla\rho) \quad \text{(Eq. 16)}$$

The first expression of the xc energy is obtained from the model of the uniform electron gas (UEG), where the density is constant in every point of the space. Although this is far from reality, it gives a manner of obtaining the energy of the fictitious non-interacting system, where only the local density is considered, hence the term LDA. The GGA conceives the density as a varying quantity, by means of its first derivatives. A further improvement is the meta-GGA approach, where also the second derivative is involved.

3.3 Density Functionals

Functionals can be organized in different groups, depending on their computing characteristics[5].

(A) LDA functionals.

(B) GGA functionals.

(C) meta-GGA functionals.

(D) Hybrid functionals.

(E) Fully non-local functionals.

(A) These are the simplest density functionals, and they were used for a generation in materials science, but they are insufficiently accurate for most chemical purposes. LDA typically overbinds molecules by about 30 kcal/mol, an unacceptable error for chemical applications[4].

(B) These are typically more accurate than LDA. Most importantly, they greatly reduce the bond dissociation energy error, and generally improve transition-state barriers. For example, as pointed out from F. Furche and J. P. Perdew[6], the bond dissociation energy of diatomic potassium K_2 is 15.4 kcal/mol with LDA, contrarily to 13.0 kcal/mol with PBE. The experimental value reported is 12.0 kcal/mol, clearly closer to the one obtained with PBE. But, unlike LDA, there is no single universal form. Popular GGAs include PBE[7] and BLYP[8,9].

(C) Next come meta-GGAs, which additionally depend on the Kohn-Sham kinetic energy density.

(D) Hybrid functionals, mix some exact exchange with a GGA. The most popular functional in use today is **B3LYP**. By mixing in only a fraction of exact exchange (about 20%), one can mimic effects of static correlation, provide more precise bon dissociation energies and produce a highly accurate functional. It is shown by Furche and Perdew[6] that potassium hydride (KH) has a bond dissociation energy of 46.7 kcal/mol with LDA, whereas 42.9 kcal/mol with B3LYP. The experimental value is 42.2 kcal/mol, closer to the one obtained with B3LYP. Its first use was to compute the vibrational absorption and circular dichroism[10] and nowadays it is mainly used for studying organic compounds, although these should not be too large[11].

(E) The need to overcome the difficulty encountered for long-range dispersion effects motivated the definition of this other group of functionals. As the exchange-correlation effect (XC) of electrons located in remote parts of a molecule cannot be properly described by the previous functionals, a van der Waals attraction contribution was initially added in a classical force field flavor[12,13]. This method however can only be applied to a small class of molecules and in addition its successful use is achieved by a meticulous calibration and knowledge. A fully non-local non-empirical dispersion correction to GGAs was proposed by Langreth, Lunqvist *et al*.[14,15]. Their functional explicitly depends on the density and its gradient at all parts of coordinates and exhibits

correct behavior for non-overlapping subsystems but still the sensitivity of the results and the ways to reduce the computational cost leave open questions.

3.4 Basis-sets and Orbitals

One-particle wavefunctions can have several expressions depending on specific cases. The Molecular Orbital approximation (MO) is one of the most famous methods by which a wavefunction can be determined. For polyelectronic systems, the Slater determinant is the final expression given to the wavefunction, which can finally solve the Hartree–Fock equations[16] but so applies also to DFT-KS. In practice, the unknown one-electron function in the Slater determinant is expressed as a linear combination of known basis functions χ_a as follows Dropping the dependence on coordinates for simplicity):

$$\varphi_i = \sum_{\alpha=1}^{M} C_{i,\alpha}\chi_\alpha \qquad \text{(Eq. 17)}$$

where M is the number of basis functions and $C_{i,\alpha}$ the expansion coefficients. In other words, the *basis-set* is a set of mathematical functions used to represent the one-electron wavefunctions obtained from the Schrödinger equation. As in the Hartree–Fock method, wavefunctions can also be obtained by linearly combining other simpler ones[16], which constitute a set of functions. An ideal basis-set should have certain properties[17]:

1. Each basis function should reflect the nature of the problem, such that a good representation of the orbitals can be achieved by a limited number of functions. One could mention the minimal basis-sets, which are constituted only by the number of orbitals (functions) needed to contain a set of electrons. A perfect example would be the case of a Ne atom described by a basis-set made of two *s* functions and a single three-component *p* function.

2. The basis functions should be able to generate a complete basis, such that a well-defined basis-set limit can be obtained. For example, correlation complete basis-sets such as those of the cc-PVnZ family, have preserved their popularity because, as the number *n* in their notation increases, energy and various properties converge smoothly to the complete basis-set limit[18].
3. Basis-sets composed of selected basis functions should be available in several well-defined qualities, such that the basis-set limit can be approached in a systematic fashion and the residual basis-set incompleteness can be quantified at each quality level. The basis set convergence is different for different methods and properties, which indeed indicates that dedicated and optimized basis sets will be more efficient than general purpose ones.

Two types of basis functions (or orbitals) are most commonly used, as we will briefly see below. For atoms, it is known that the exact wave function must have a cusp at the nuclear position and that the electron density should fall off exponentially in the long distance limit. This suggests that Slater-type orbitals (STOs) with the functional form given in Eq. 18 should be well suited for achieving a good representation of Atomic Orbitals with only a few functions[18].

$$\chi_{\zeta,n,l,m}(r,\theta,\varphi) = Nr^{n-1}Y_{l,m}(\vartheta,\varphi)e^{-\zeta r} \qquad \text{(Eq. 18)}$$

In Eq. 18, r, θ, and φ are spherical coordinates, where r is the distance between the electron and the nucleus at which the STO is centered, N is a normalization constant, $Y_{l,m}$ is a spherical harmonic function (the angular part of the STO), ζ is called the orbital exponent, and n is the principal quantum number. Unfortunately, the calculation of 3- and 4-center two-electron integrals with STO functions is difficult and computationally inefficient[19]. The common way to overcome this limitation in electronic structure calculations is to replace STOs by Gaussian-type Orbitals (GTOs)[20].

$$\chi_{\zeta,i,j,k}(x,y,z) = Nx^i y^j z^k e^{-\zeta r^2} \quad \text{(Eq. 19)}$$

In their Cartesian definition, GTOs can be written as in Eq. 19. Here *x, y, z* are the Cartesian components of the distance between the electron and the center of the GTO, normally a nuclear position. The orbital exponent ζ defines the radial extent of the function, and the sum of the powers *i, j, k* in the angular part of the function defines the angular momentum of the atomic orbital. For an *s*-type orbital, $i + j + k = 0$, while $i + j + k = 1$ is a *p*-type orbital, etc. GTOs are unable to properly describe the behavior in the short and long ranges due to the r^2 dependence in the exponential. A GTO possesses a zero slope instead of a cusp at the nucleus, and the function falls off too rapidly with increasing distance and thus represents the "tail" region of the orbital poorly. The usual way of improving the accuracy is to use a linear combination of a few GTOs to describe a single STO. Although the number of basis functions and, consequently, the number of integral evaluations are increased, the ease by which these integrals can be calculated makes GTOs the preferred basis functions in practical electronic structure calculations for molecules. In the molecular calculations run in this work, the 6-311G(d,p) split-valence basis-set was often chosen. Since the valence electrons are the ones directly involved in chemical reactions, it is common to separate them from the internal ones and to represent them by more than one basis function, each of which can in turn be composed of a fixed linear combination of primitive Gaussian functions. The general notation is of the form "X-YZWG" and it was introduced by John Pople *et al*.[21]. This means that the 6-311G(d,p) basis-set is composed by 6 primitive Gaussians comprising each core atomic orbital basis function. The Y, Z and W indicate that the valence orbitals are composed of three basis functions each, the first one composed of a linear combination of *Y* primitive Gaussian functions, the other composed of a linear combination of *Z* primitive Gaussian functions and the last one by W Gaussian functions. The letters in bracket (d,p) refer to polarization functions, *i.e.*

additional contributions which give the basis-set a *d*- and *p*-type description of the behavior of the electrons.

3.5 Time-Dependent DFT (TD-DFT)

The Kohn-Sham Density Functional Theory (DFT-KS) formulated in paragraph 3.2 only applies to time-independent studies. A desired extension to time-dependent cases requires the re-formulations of the two HK theorems, which begins with the time-dependent hamiltionian of Eq. 20.

$$\hat{H}_{el.}(\vec{\boldsymbol{r}}_{ij}, t) = -\frac{1}{2}\sum_i \nabla_i^2 + \sum_j \sum_{i>j} \frac{1}{\vec{\boldsymbol{r}}_{ij}} + \sum_i v(\vec{\boldsymbol{r}}_i, t) \qquad \text{(Eq. 20)}$$

Here, the dependence on time of the Hamiltonian is introduced, where the last term is a time-dependent potential, which, according to the Runge-Gross theorem, is in a one-to-one correspondence with the TD density and the potential[22]. This theorem is the time-dependent analogue of the first Hohenberg-Kohn theorem which introduces the one-to-one correspondence between the ground-state electron density and an external potential. Since this latter defines the ground-state wavefunction, which also depends on the density, in the time-dependent re-formulation it will look like in Eq. 21.

$$\Psi(\vec{\boldsymbol{r}}, t) = \Psi[\rho(t)](t)e^{-i\alpha(t)} \qquad \text{(Eq. 21)}$$

According to the generalization of the Runge-Gross theorem by van Leeuwen, a time-dependent density of a fictitious non-interacting system with KS-like basis functions must exist. The sum in Eq. 22 runs over all the single-electron orbitals $\varphi_i(\vec{\boldsymbol{r}}, t)$.

$$\rho(\vec{\boldsymbol{r}}, t) = \sum_i |\varphi_i(\vec{\boldsymbol{r}}, t)|^2 \qquad \text{(Eq. 22)}$$

The principle of the existence of a reference ground-state density, which equals by hypothesis the real one, also applies to the time-dependent case, *i.e.* $\rho(\vec{\boldsymbol{r}}, t) = \rho_s(\vec{\boldsymbol{r}}, t)$. The $\varphi_i(\vec{\boldsymbol{r}}, t)$ are then used

to solve a Time-Dependent Kohn-Sham (TDKS) equation (Eq. 23), which is of the same type of Eq. 8, where only the *N* one-particle orbitals, that were initially occupied, are time-propagated. Here, time is the second variable of all quantities (operators and orbitals).

$$\left[-\frac{1}{2}\nabla^2 + v_s[\rho](\vec{r},t)\right]\varphi_i(\vec{r},t) = i\frac{\partial}{\partial t}\varphi_i(\vec{r},t) \qquad \text{(Eq. 23)}$$

$$v_s[\rho](\vec{r},t) = v(\vec{r},t) + v_J[\rho](\vec{r},t) + v_{xc}[\rho](\vec{r},t) \qquad \text{(Eq. 24)}$$

At this point, the static KS equations can self-consistently be solved, making an approximation on $v_{xc}[\rho](\vec{\boldsymbol{r}})$ in Eq. 24; then, one let the *N* initially occupied orbitals time-propagate from an initial t_0(the ground state) to a final time t_1, making an approximation on $v_{xc}[\rho](\vec{\boldsymbol{r}},t)$. The most common approximation is known as adiabatic approximation, for which the same xc functional from static DFT is used and then it is evaluated with a TD density (*i.e.* no *memory* effects): briefly, at any given time, the xc potential does not depend on the history of the charge density, but only on its present distribution. But the idea of self-consistency in static DFT is different from that in TDDFT, where the self-consistency must be built into the time propagation scheme: first, the static KS equations with the ground state density $\rho_0(\vec{\boldsymbol{r}}) = \rho(\vec{\boldsymbol{r}},t_0)$ must be solved and then one makes a guess of the TD density $\rho(\vec{\boldsymbol{r}},t)$ for all times $t_0 \le t \le t_1$; a new set of orbitals will be determined by propagating the TDKS equations with $v_s[\rho](\vec{\boldsymbol{r}},t)$ and they will yield a new density and so on. Therefore, the self-consistent propagation of the TDKS equation is carried out step by step for all times between t_0 and t_1.

TD-DFT is a particularly useful technique in the computation of excitation energies which can be obtained in two ways: real-time TD-DFT and linear-response TD-DFT[4]. While the former is mainly used in chemistry and biophysics, the latter is the principal scheme implemented in most

standard quantum chemistry codes. It is possible to work with a density in the frequency domain, given by the Fourier transform of the first-order (linear) density response as follows:

$$\rho^{(1)}(\vec{\boldsymbol{r}},\omega) = \int dr' \chi(\vec{\boldsymbol{r}},\vec{\boldsymbol{r}}'\omega) v^{(1)}(\vec{\boldsymbol{r}}',\omega) \quad \text{(Eq. 25)}$$

$$\rho^{(1)}(\vec{\boldsymbol{r}},t) = \int dt' \int d\boldsymbol{r}' \chi(\vec{\boldsymbol{r}},t,\vec{\boldsymbol{r}}',t') v^{(1)}(\vec{\boldsymbol{r}}',t') \quad \text{(Eq. 26)}$$

where ω is the frequency and $\chi(\vec{\boldsymbol{r}},\vec{\boldsymbol{r}}'\omega)$ is the density-density response function and $v^{(1)}(\vec{\boldsymbol{r}}',t')$ the external potential, considered as the external perturbation over time *t*'.

Like in ground-state DFT, some limitations arise mainly due to the fact that no exact xc functional is known nowadays. For example, B3LYP and PBE can also be employed in TD-DFT, but their choice must include which molecular system is under estimation. Now calculations can follow the same rationale as in ground-state DFT, with particular applications in the determination of optical spectra, which can only be obtained in a time-dependent approach, as the excited states involved have only a limited range of time of existence.

3.6 Evaluation of the electronic transitions

When a molecule is excited from the electronic ground state to an energetically higher-lying excited state, the electronic many-body wavefunction changes. The analysis of such changes could be done directly on the excited state of interest, considering the new electron density or the wavefunction itself. Often however, the differences between the ground state and the excited state are required, the analysis of which can be done by considering the Molecular Orbitals, the Transition Density or the Difference Density Matrixes and the Attachment/Detachment Density Matrixes. If the transition density approach is considered, the concept of matrix can be clarified as follows. The transition couples the electronic ground state with the excited one.

$$T(\vec{\boldsymbol{r}}) = N \int |\Psi_{exc.}(\vec{\boldsymbol{r}}_1, \vec{\boldsymbol{r}}_2, \dots, \vec{\boldsymbol{r}}_n)\Psi_0(\vec{\boldsymbol{r}}_1, \vec{\boldsymbol{r}}_2, \dots, \vec{\boldsymbol{r}}_n)|\, d\vec{\boldsymbol{r}}_1, d\vec{\boldsymbol{r}}_2, \dots, d\vec{\boldsymbol{r}}_n \qquad \text{(Eq. 27)}$$

If the electronic ground state is a single Slater determinant and the excited state is a combination of determinants, $T(\vec{\boldsymbol{r}})$ is given as a linear combination of single-determinants transition densities weighted by their expansion coefficients.

$$T(\vec{\boldsymbol{r}}) = \sum_{i,a} c_{i,a} \int |\Psi_{exc.}(\vec{\boldsymbol{r}}_1, \vec{\boldsymbol{r}}_2, \dots, \vec{\boldsymbol{r}}_n)\Psi_0(\vec{\boldsymbol{r}}_1, \vec{\boldsymbol{r}}_2, \dots, \vec{\boldsymbol{r}}_n)|\, d\vec{\boldsymbol{r}}_1, d\vec{\boldsymbol{r}}_2, \dots, d\vec{\boldsymbol{r}}_n \qquad \text{(Eq. 28)}$$

In hole-particle excitations, there is a variety of electronic transitions simultaneously taking place among the canonic orbitals of a given electronic system. This might restitute a complicated picture of an event where only one excitation could often be the one searched. To this regard, the analysis of the transition density can be more easily done via the so-called Natural Transition Orbital analysis (NTO analysis), which simplifies the representation of the electronic transitions, by separately performing unitary transformations on the occupied and virtual set of orbitals[23]. Since the transition density contains matrix elements of the type "n_{occ} x n_{virt}" (occupied and virtual), it cannot simply diagonalized but rather transformed via the Amos–Hall approach[24]. At the end of matricial operations which lead to the writing of a "n_{occ} x n_{occ}" matrix, a one-to-one mapping between occupied and virtual orbitals is established.

The further improvement of NTO analysis are Attachment/Detachment Density Matrixes, which are a valuable tool to represent the transitions involved in vertical electronic excitations. In particular, they are one-electron matrixes, obtained from the diagonalization of the Difference Density Matrix, that define an electronic transition as **D** → **A**, where **D** is the Detachment Density and **A** the Attachment Density. Their difference **Δ** = **A**–**D** highlights the actual hole-charge separation in a vertical transition (h^+/e^-)[25]. This is what is used in this work to represent the excited states involving carbon nitride and the substrates.

3.7 Calculations on periodic systems

Since carbon nitride materials are extended 2D systems, a more peculiar approach is needed in order to properly account for their big size and properties which repeat in space in a defined manner. The Kohn-Sham orbitals introduced earlier for polyelectronic (but still limited) systems are now insufficient to describe the huge amount of electrons present in such cases. In condensed-matter physics, one possible way to solve Kohn-Sham equations is a Fourier series which is applied in a unit cell defined by the three vectors $\mathbf{a}_1$, $\mathbf{a}_2$, $\mathbf{a}_3$, which give the volume $\Omega = \left| \mathbf{a}_1 \cdot \mathbf{a}_2 \times \mathbf{a}_3 \right|$. These vectors define a lattice in real (direct) space as follows: $\mathbf{T} = N_1\mathbf{a}_1 + N_2\mathbf{a}_2 + N_3\mathbf{a}_3$, with $N_1, N_2, N_3 \in \mathbb{R}$. In this way, both the electron density and potential are periodic. According to the Bloch theorem[26], single-particle electronic wavefunctions in a periodic potential may be expressed as the product of a periodic function in the unit cell and a plane wave. That is,

$$\varphi_i(\vec{\boldsymbol{r}}) \rightarrow \varphi_{i,\boldsymbol{k}}(\vec{\boldsymbol{r}}) = u_{i,\boldsymbol{k}}(\vec{\boldsymbol{r}})e^{i\boldsymbol{k}\cdot\vec{\boldsymbol{r}}} \qquad \text{(Eq.29)}$$

$$u_{i,\boldsymbol{k}}(\vec{\boldsymbol{r}}) = u_{i,\boldsymbol{k}}(\vec{\boldsymbol{r}} + \boldsymbol{T}) \qquad \text{(Eq. 30)}$$

Since $u_{i,\boldsymbol{k}}(\vec{\boldsymbol{r}})$ is periodic, the wavefunctions can be expressed by a linear combination of plane-waves, so the energy bands in a crystal lattice are *periodic functions in reciprocal space*, where the vector **k** defines the periodicity and a volume known as the first Brillouin zone of the reciprocal lattice.

In addition to the creation of periodicity as a new concept to face the issue of bigger systems, a further development is needed in order to overcome the number of all core electrons present. Pseudopotential is an attempt to replace the complicated effects of the motion of the core electrons of an atom and its nucleus, such that they are included in the mathematical expression in an averaged way, thus creating an effective core-density, whereas the valence electrons are described by pseudo-wavefunctions with significantly fewer nodes. Pseudopotential calculations have

provided explanations for a vast number of solid-state properties, which had been previously rationalized mostly with Pauling's empirical rules[27]. Accurate analyses of real materials became possible at the beginning of the 1960's[28,29]. Efforts made in order to find a pseudopotential for each element enabled the study of electronic properties of surfaces, by matching bulk and surface wavefunctions[30]. Studying electron charge redistribution was also made possible by separating the potential into an ionic part, the pseudopotential, and an electronic part containing an Hartree–Fock exchange correction. To a further extent, a DFT-adapted pseudopotential approach is also possible, this requiring the determination of functionals for the exchange and correlation[31–33]. From that point on, improvements have followed and pseudopotentials have become one of the major tools for condensed matter-physics calculations.

The improved description of electronic many-body effects within Density Functional Theory has brought an important impact on solid-state physics and chemistry. The Vienna Ab-Initio Software Package (VASP) is particularly efficient in dealing with pseudopotential calculations and thus enabling the study of solid-state materials such as carbon nitride. In 1994 Blöchl proposed a new formalism called projector-augmented waves (PAWs), where an accurate all-electron representation of the electronic system is placed in a one-to-one correspondence with a pseudopotential-like treatment of the valence electrons[34]. In addition to VASP, the PAW method has been implemented in several other codes, such as PWPAW[35], SOCORRO[36] or the GPAW code[37], but the one used in this work is indeed VASP. Kresse *et al*. developed this package in order to overcome the difficulty related to large atomic systems in solid-state chemistry[38,39]. The first rule which VASP is based on is the expansion of the basis-sets used in the calculations in plane-waves, which provide a lighter description of the all-electron arrangement of a system.

3.8 Plane waves

The development of plane-waves to represent the wavefunctions in periodic systems introduces some advantages: (*i*) it is easy to pass from a real-space representation to a momentum-space via a Fourier Transformation, where the kinetic energy *T* is diagonal; (*ii*) to control the basis-set convergence, it is sufficient to monitor the eigenvalues and total energy as functions of the cut-off energy, *i.e*. the highest *T* for each plane-wave; (*iii*) Basis-set superposition errors, which characterize local basis-sets, can be avoided. However, a general requirement that always needs to be taken into account is that a *reasonable convergence of a plane wave expansion is obtained only if the nodal character of the valence orbital is eliminated*, *i.e*. if the ion–electron interaction is described by a given pseudopotential. With this, the choice of a convenient basis-set for solid-state DFT calculations is needed to expand the Kohn-Sham eigenfunctions, which are localized wavefunctions.

3.9 Computational protocol for modelling the perfluoroalkylation of 1,3,5–trimetoxybenzene

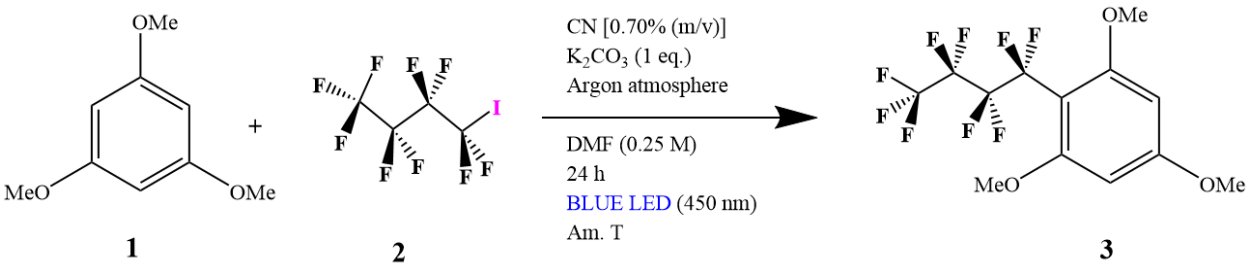

Figure 3–1: C–C bond-formation reaction between 1,3,5–trimethoxybenzene (**1**) and nonafluoro–1–iodobutane (**2**).

This reaction involves (functionalized) carbon nitride in the presence of light. As the first step, we used DFT to optimize periodic models of carbon nitride at the ground-state. The code used to run periodic DFT calculations is the Vienna Ab-Initio Software Package (VASP) with the Projector-

Augmented Wave (PAW) basis-set. Exchange and correlation effects are treated at the Perdew−Burke−Ernzerhof (PBE) level with the dispersion forces treated by Grimme correction (PBE+D2), *i.e*. the evaluation of the long-range electronic correlation effects via the D2 approach proposed by Stefan Grimme in 2006[40]. A kinetic energy cut-off of 500 eV is set and using a Monkhorst-Pack sampling of 3×3×1 for the Brillouin zone (BZ) integration on all the CN unit cells replicated 4x4x1 times, with the vacuum spacing set to be 30 Å to avoid the interaction with periodic images. Dipole moment correction was employed along the 'c' axis (Z direction & perpendicular to the *g*-CN surface). The geometries of pristine and defective CN surfaces along with C_4F_9–I adsorbed were fully optimized at the PBE/GGA level of theory prior to the calculation of the electronic properties at the hybrid (HSE06) level of theory. Bond orders and ground state partial charge transfers were computed using the Density-Derived Electrostatic and Chemical method DDEC06[41].

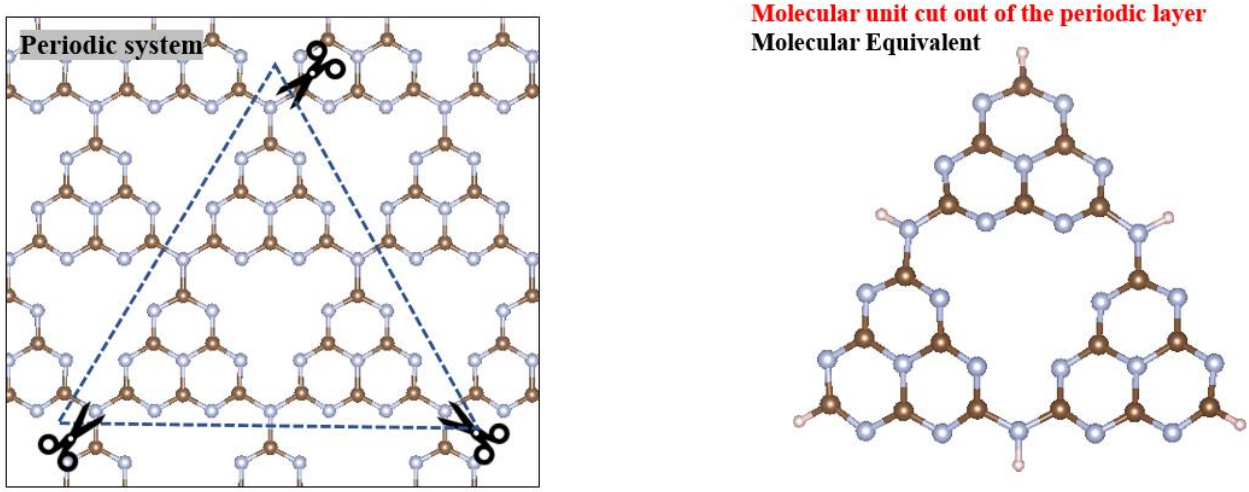

Figure 3–2: Periodic and molecular structures for modelling carbon nitride species.

DFT and TD-DFT calculations of the *g*-CN molecular equivalent units (Fig. 3–2) with and without C_4F_9–I adsorption were performed using the Gaussian16 code at the B3LYP/6-311G(d,p) level of theory for molecular optimizations. The electronic structure and UV-Vis absorption spectra

calculations, along with the corresponding NTO analysis were performed on the molecular systems at the hybrid level of theory (HSE1HSE), to maintain a consistency with the electronic structure obtained with the periodic DFT calculations. Prior to TD-DFT calculations on the molecular systems, the consistency between the periodic and molecular *g*-CN/C_4F_9–I descriptions was ensured by comparing the electronic structure at the hybrid level (HSE06) of theory.

3.10 Computational protocol for modelling the dual carbon nitride/Ni arylamination reaction

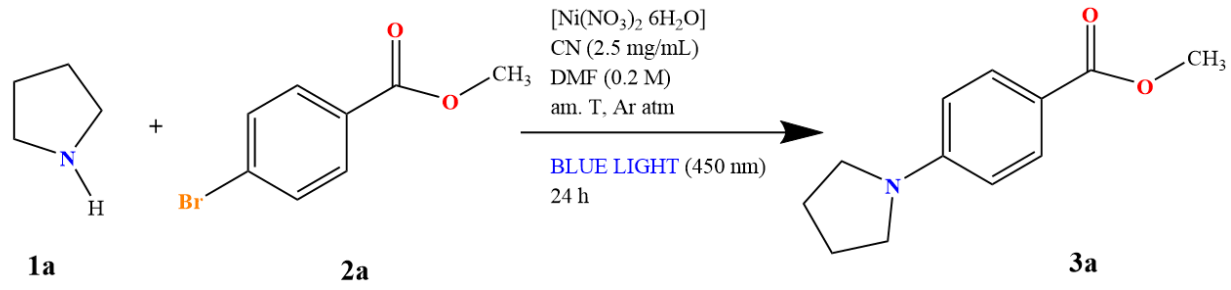

Figure 3–3: C–N bond-formation reaction between pyrrolidine (**1a**) and methyl–4–bromobenzoate (**2a**).

This reaction involves carbon nitride and a nickel complex as a co-catalyst in the presence of light. The structures of both species were optimized using the Gaussian16 code at the B3LYP level of theory in the ground state, with non-metal atoms treated with the Ahlrichs basis-set Def2SVP, whereas the Los-Alamos Effective-Core Potential (ECP) basis-set LanL2DZ was used for the nickel atom. A solvent cavity of *N*,*N*-dimethylformamide (DMF, $\varepsilon \approx 37$) was added in the ground-state optimizations as a Polarizable Continuum Model (PCM), which is the most commonly used method to compute solvation effects in computational chemistry[42]. The theoretical models were built and visualized by use of the GaussView 6.0 software as square-planar starting geometries presenting a Ni(II) metallic center with a d^8 valence electronic configuration. The excited-state calculations were performed on the previously optimized structures by use of TD-DFT at the

HSE06 level of theory. The excited-state electronic structures were visualized with the VESTA software. Molecular models for the carbon nitride binding sites coordinated to nickel were used for the TD-DFT calculations, also run at the HSE06 level.

References

[1] P. Hohenberg, W. Kohn, *Phys*. *Rev*., 245, (**1964**), 841–842.

[2] The NIST Reference on Constants, units and uncertainties, 20 May 2019. Retrieved 2019-05-20.

[3] W. Kohn, L. Sham, *J*. *Phys*. *Rev*., 140, (**1965**), A1133–A1138.

[4] A. Dreuw, M. Head-Gordon, *Chem*. *Rev*., 105, (**2005**), 4009–4037.

[5] D. Rappoport, N. R. M. Crawford, F. Furche, K. Burke, "*Which functional do I choose*?", (**2008**).

[6] F. Furche, J. P. Perdew, *J*. *Chem*. *Phys*., 124, (**2006**).

[7] J. P. Perdew, K. Burke, M. Ernzerhof, *Phys*. *Rev*. *Lett*., 77, (**1996**), 3865–3868.

[8] A. D. Becke, *Phys*. *Rev*. *A*, 38, (**1988**), 3098–3100.

[9] C. Lee, W. Yang, R. G. Parr, *Phys*. *Rev*. *B*, 37, (**1988**), 785–789.

[10] J. Tirado-Rives, W. L. Jorgensen, *J*. *Chem*. *Theory Comput*., 4, (**2008**), 297–306.

[11] L. Simón, J. M. Goodman, *Org*. *Biomol*. *Chem*., 9, (**2011**), 689.

[12] R. Ahlrichs, R. Penco, G. Scoles, *Chem*. *Phys*., 19, (**1977**), 119–130.

[13] S. Grimme, *J*. *Comput*. *Chem*., 27, (**2006**), 1787–1799.

[14] M. Dion, H. Rydberg, E. Schröder, D. C. Langreth, B. I. Lundqvist, *Phys*. *Rev*. *Lett*., 92, (**2004**), 246401.

[15] M. Dion, H. Rydberg, E. Schröder, D. C. Langreth, B. I. Lundqvist, *Phys*. *Rev*. *Lett*., 95, (**2005**), 109902.

[16] R. J. Bartlett and J. F. Stanton, in *Reviews in Computational Chemistry*, K. B. Lipkowitz and D. B. Boyd, Eds., VCH Publishers, Inc., NY, 1994, Vol. 5, pp. 65–169. Applications of Post-Hartree-Fock Methods: A Tutorial.

[17] B. Nagy, F. Jensen, *Reviews in Computational Chemistry*, *Volume 30*, First Edition. Edited by Abby L. Parrill and Kenny B. Lipkowitz. @ 2017 John Wiley & Sons, Inc. Published 2017 by John Wiley & Sons, Inc.

[18] J. G. Hill, *Int*. *J*. *Quant*. *Chem*., 113, (**2013**), 21–34.

[18] J. C. Slater, *Phys*. *Rev*., 36, (**1930**), 0057.

[19] J. E.Avery and J. S.Avery, in *Advances in Quantum Chemistry*, R. S. John and J. B. Erkki,Eds., Academic Press, 2015, Vol. 70, pp. 265–324. Chapter Six—Molecular Integrals for Exponential-Type Orbitals Using Hyperspherical Harmonics.

[20] S. F. Boys, *Proc. Roy. Soc. London A: Mat. Sci.*, 200, 542 (**1950**).

[21] R. Ditchfield, W. J. Hehre, J. A. Pople, *J. Chem. Phys*. 54 (2), (**1971**), 724–728.

[22] E. Runge, E. K. U. Gross, *Phys. Rev. Lett.*, 52, (**1984**), 997.

[23] R. L. Martin, *J. Chem. Phys*., 118, (**2003**), 4775.

[24] A. T. Amos, G. G. Hall, *Proc. R. Soc. A*, 263, (**1961**), 263–483.

[25] M. Head-Gordon, A. M. Graña, D. Maurice, C. A. White, *J. Phys. Chem*., 99, (**1995**), 14261–14270.

[26] F. Bloch, *Z. Physik*, 52, (**1929**), 555–600.

[27] M. L. Cohen, *Phys. Script*., Vol. T1, (**1982**), 5–10.

[28] I. V. Abarenkov, V. Heine, *Phil. Mag*., 12, 529, (**1965**).

[29] M. L. Cohen, T. K. Bergstresser, *Phys. Rev*., 141, 789, (**1966**).

[30] J. A. Appelbaum, D. R. Hamann, *Rev. Mod. Phys*., 48, 3, (**1976**).

[31] E. Wigner, *Phys. Rev*., **46**, 1002, (**1934**).

[32] L. Hedin, B. I. Lundqvist, *J. Phys*., C4, 2064, (**1971**).

[33] U. von Barth, L. Hedin, *J. Phys*., C5, 1629, (**1972**).

[34] P. Blöchl, *Phys. Rev. B*, 50, (**1994**), 17953.

[35] N. Holzwarth, G. Matthews, R. Dunning, A. Tackett, Y. Zeng, *Phys. Rev. B*, 55, (**1997**), 2005.

[36] http://dft.sandia.gov/socorro.

[37] J. Mortensen, L. Hansen, K. Jacobsen, *Phys. Rev. B*, 135, (**2001**), 348.

[38] G. Kessner, J. Hafner, *J. Phys. Rev. B*, 47, (**1993**), 558.

[39] G. Kresse, J. Furthmüller, *J. Computat. Mater. Sci*., 6, (**1996**), 15.

[40] S. Grimme, *J. Comput. Chem*., 27, (**2006**), 1787–1799.

[41] T. A. Manz, N. G. Limas, *RCS Adv*., 6, (2016), 47771–47801.

[42] S. Miertus, E. Scrocco, J. Tomasi, *Chem. Phys*., 55, (**1981**), 117–129.

Chapter 4: the modelling of the C–C bond-formation reaction between 1,3,5–trimethoxybenzene and nonafluoro–1–iodobutane

4.1 Objective of this study

Carbon nitride is a highly versatile material, which can adapt to numerous catalytic contexts. As presented in chapter 2, several generalized studies are available to date which explain how doping by external elements can modify its optical properties to address specific types of catalytic processes. However, little has been revealed about the mechanisms of many of the reactions to which carbon nitride participates as catalyst. A systematic computational investigation about the catalytic response of the carbon nitride materials tested in the perfluoroalkylation of 1,3,5–trimethoxybenzene is the subject of this Chapter, in order to explain the marked activity observed for *am*. CN, one of the post-synthetic forms prepared recently in Trieste, with respect to the pristine catalyst. The structure of the defects introduced by the thermal treatment and the degree of interaction of those defects with the C_4F_9–I reagent are investigated with DFT. The theoretical study starts with the design of models for the pristine and defective CNs and the calculation of their stability and electronic structure. The second modelling stage deals with the interaction between such carbon nitride structures and C_4F_9–I. Finally, the theoretical characterization of the excited states of the carbon nitride/C_4F_9–I systems with Time-Dependent DFT (TD-DFT) and the results are interpreted to shed light on the experimental reaction mechanism.

4.2 The post-synthetic forms of carbon nitride

Several post-synthetic forms of carbon nitride deriving from the pristine one were prepared[1], (Fig. 4–1) with the intention of comparing their catalytic efficiencies in the perfluoroalkylation of 1,3,5–trimethoxybenzene. In particular:

1. The amorphous carbon nitride (*am*. CN) is prepared by thermal treatment of the pristine one (*g*-C_3N_4) in a tubular furnace at 550°C in argon.

2. The reduced carbon nitride (*red*. CN) is prepared by performing the thermal treatment at 550°c in a gaseous H_2 flux.
3. The oxidized carbon nitride (*ox*. CN) was prepared by treatment with a 4 M HNO_3 solution.

These post-synthetic treatments bring on changes in the molecular structure and the packing patterns with respect to the regular and well-defined crystal structure of *g*-C_3N_4.

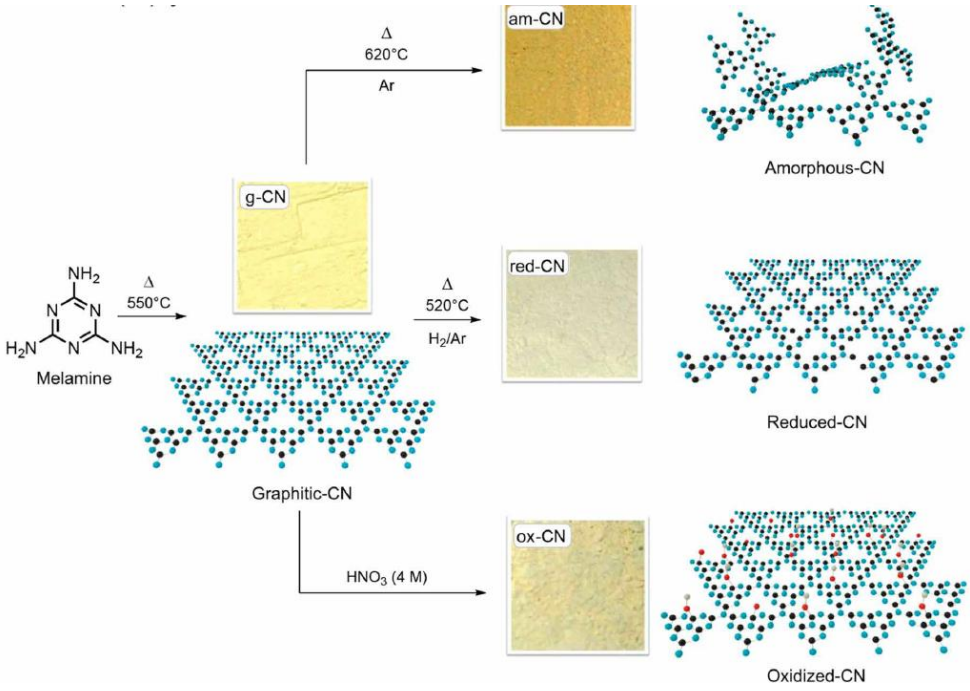

Figure 4–1[1]: Synthesis of pristine carbon nitride (*g*-CN) from melamine and amorphous (*am*. CN), reduced (*red*. CN) and oxidized (*ox*. CN) post-synthetic forms.

The identification of the structural and chemical alteration consequent to each modification was investigated by XRD and XPS measurements. It can be observed for *am*. CN that the strong 27.2° peak ascribed to the (002) plane of the interlayer stacking of the conjugated aromatic system, associated with the crystallinity of the material, is broader and less intense as compared to the other three materials, indicating an increased amorphous nature (Fig. 4–2a). The calculated crystallite size (Fig. 4–2a, inset table) is therefore smaller (5.4 nm), implying a reduction in the number of layers in *am*. CN. Consistently, the intensity of the (100) reflection at 12.7°, which is associated

to the intralayer spacing, also decreases from *g*-C_3N_4 to *am*. CN, further corroborating the hypothesis of the partial rupture of the strands of heptazines.

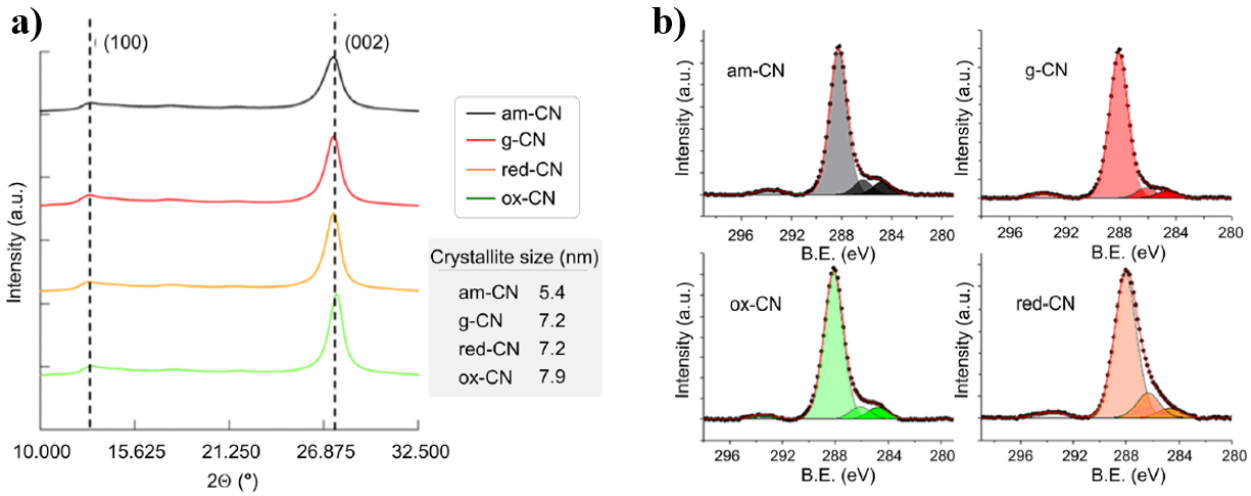

Figure 4–2[1]: Structural information about the post-synthetic forms of carbon nitride materials: **a)** XRD patterns and crystallite size; **b)** XPS spectra, showing the C1s region.

In the XPS spectra, all C1s regions for the four CN materials can be deconvoluted in four components, 284.8, 286.2, 288.2 and 293.5 eV, assigned to C–C, C–N, C═N–C moieties, and the signature of π–π* excitations, respectively. Amorphization by high-temperature treatment is reflected into the lower contribution of the aromatic component (288.2 eV) with respect to the other species, as compared to *g*-C_3N_4. Again, this is consistent with the fact that the thermal treatment partially disrupts the molecular and crystal structure of *g*-C_3N_4.

Further important experimental results are the Electron Paramagnetic Resonance spectra (EPR) obtained for the four carbon nitride materials. As shown in Figure 4–3, a clear signal for the presence of unpaired electrons is present in each form, suggesting that all four materials contain radical centers.

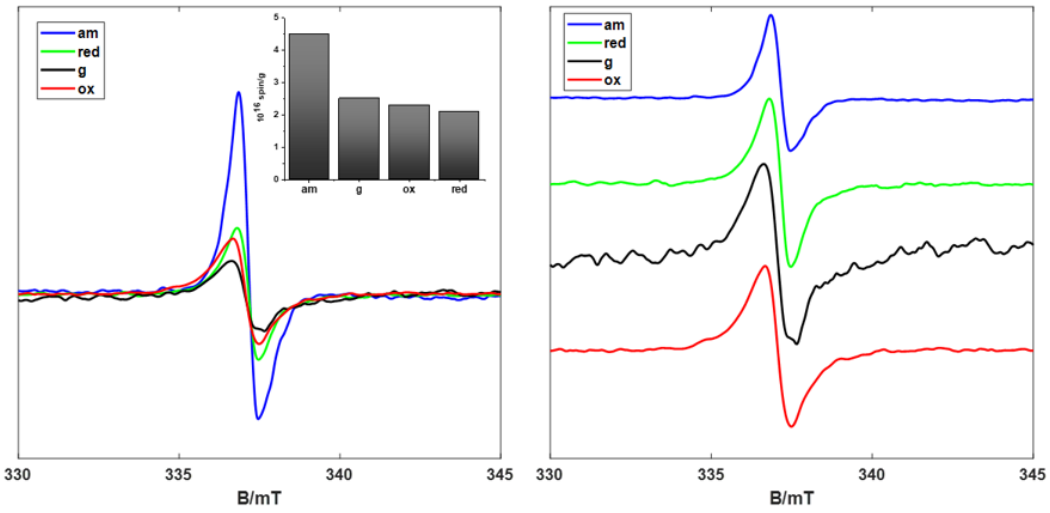

Figure 4–3[1]: Continuous Wave X-band EPR Spectra of the four carbon nitride forms considered, recorded in the dark at 77 K.

In the inset of the left panel, a bar-plot shows the density of the radical centers expressed as n° spins/g for each entry and it is possible to observe that *am*. CN has the highest density of native unpaired electrons. This constitutes very important extra information about how to build the theoretical models of carbon nitrides that will be presented in the computational study below.

4.3 Catalytic activity of the carbon nitride materials

The four forms of carbon nitride described above were tested as photocatalysts for the perfluoroalkylation of 1,3,5–trimethoxybenzene. Table 4–1 compares the yields of the reaction for various experimental conditions. Specifically, *am*. CN reveals the highest catalytic response in the reaction, even higher than that shown by *red*. CN, which is also a defective structure. Even at a lower loading (0.27% *w*/*v*), *am*. CN brings the reaction to completeness, a result that makes this form particularly interesting for the investigated class of reactions.

Table 4-1[1]: Reaction yields determined by ^{1}H-NMR spectroscopy using 1,1,2–trichloroethene as the internal standard. (*w*/*v*) = weight/volume, concentration.

Entry [loading%]	Yield (%)
g-CN [0.35% (*w*/*v*)]	20
ox. CN [0.35% (*w*/*v*)]	10
red. CN [0.35% (*w*/*v*)]	90
am. CN [0.35% (*w*/*v*)]	>99
am. CN [0.27% (*w*/*v*)]	>99
am. CN [0.125% (*w*/*v*)]	89
am. CN [0.063% (*w*/*v*)]	11

A possible reaction mechanism was then hypothesized and a schematic illustration is shown in Figure 4–4.

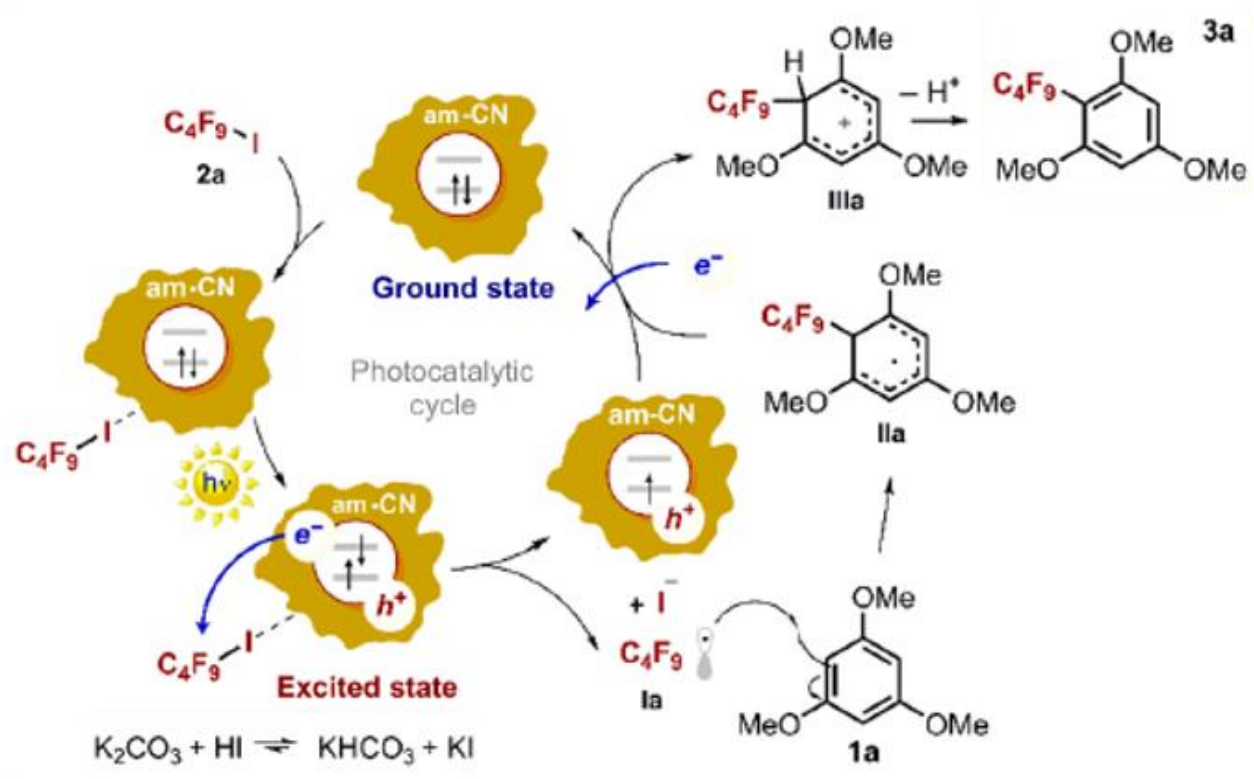

Figure 4–4[1]: Proposed reaction mechanism of the perfluoroalkylation of 1,3,5–trimethoxybenzene.

It is commonly accepted that halogen atoms can form attractive interactions by functioning as electron donor sites (*i.e.* nucleophiles)[2,3]. In compounds wherein the halogen atom is involved in

the formation of one covalent bond there is a region of higher electron density, where the electrostatic potential is negative in nearly all cases, which forms a belt orthogonal to the covalent bond, and a region of lower electron density (the so-called σ-hole) where the potential is frequently positive, mainly in the heavier halogens, which generates a cap of depleted electron density on the elongation of the covalent bond. The perfluoroalkyl substrate (C_4F_9–I) is hence thought to interact with the carbon nitride via a halogen bond established between the iodine and nitrogen atoms. Upon the absorption of light, CN photocatalyst undergoes charge separation, and the electron promoted to the conduction band can be transferred to the substrate, causing the cleavage of the C–I bond and the formation of the perfluorinated radical. This latter attacks the 1,3,5–trimethoxybenzene molecule, which then yields product **3a** at the end.

In order to shed light on this mechanism from a computational perspective, the first step is to design model structures for the defective carbon nitrides, consistent with the indications from the XPS and EPR data. Then a particular focus is made on the initial ground-state interaction between CNs and C_4F_9–I. Finally, the excited-state photochemical step, where the charge is expected to be transferred from CNs to C_4F_9–I, is modelled.

4.4 Carbon nitride models

According to what is reported in chapter 2 and to our experimental findings, graphitic carbon nitride (*g*-C_3N_4) is a mainly crystalline 2D material with 1,3,5-triazine- or heptazine-like repeating units forming its layers. The heptazine motif was therefore chosen for building the model systems for pristine and defective CNs. Figure 4–5 shows the unit-cells of the periodic CN structures, where pristine carbon nitride is represented as the standard C_3N_4 graphitic model, preserving the 0.75 C/N ratio (**P**.**0**). Following now the logic of the post-synthetic forms prepared, a radical N-vacant carbon nitride model was built, where the removal of an internal nitrogen atom in an heptazine

unit creates a radical structure, with the radical center being formally the lowest carbon atom in the disrupted ring (**1**.**a**; N-vac Heptazine Radical).

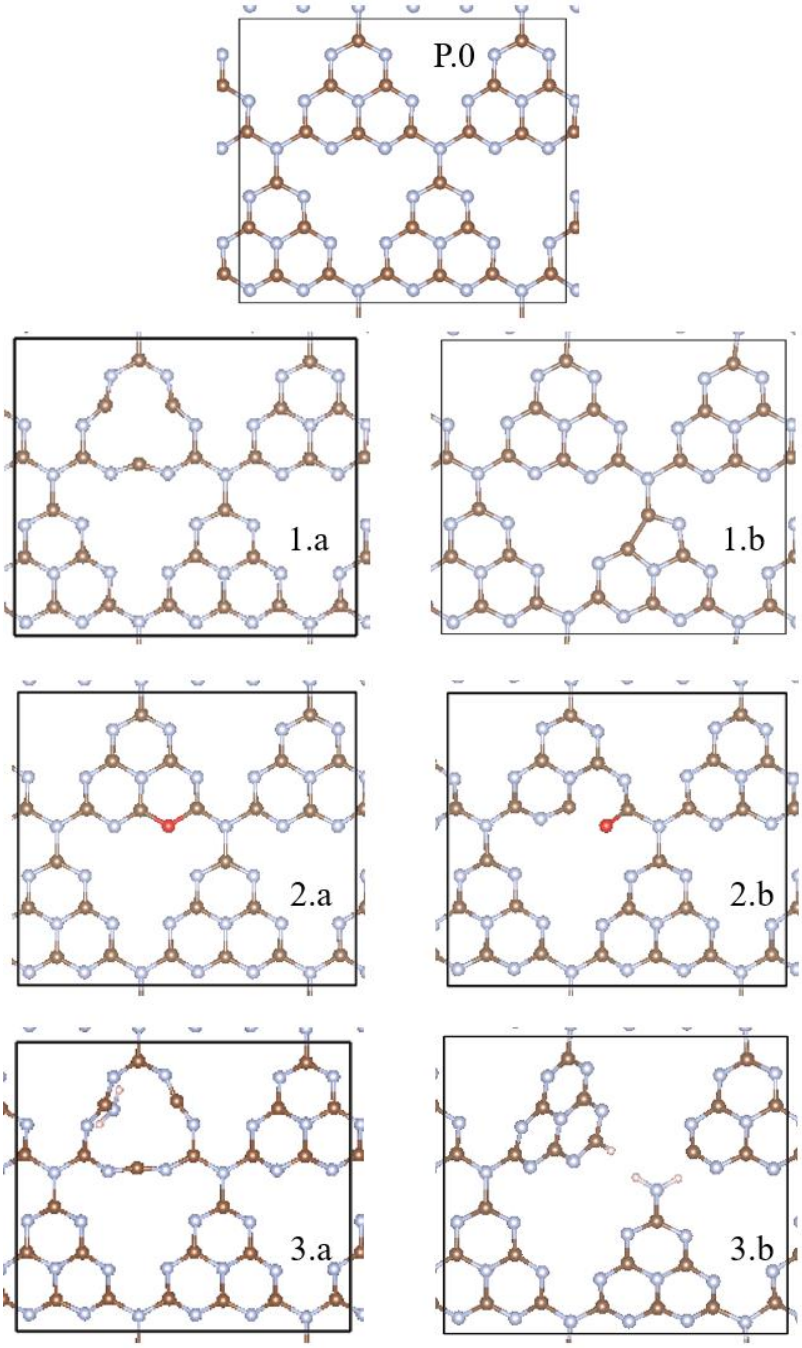

Figure 4–5: Periodic models of carbon nitride materials (carbon: brown; nitrogen: grey; oxygen: red; hydrogen: white). From top: **P**.**0** pristine; **1**.**a** N-vac Heptazine Radical; **1**.**b** N-vac Heptazine Edge Radical; **2**.**a** N-vac "Pyran-like" Radical; **2**.**b** N-vac "Carbonyl-like" Radical; **3**.**a** N-vac Heptazine Bi-Radical ($-NH_2$ group); **3**.**b** Disconnected Heptazine Radical.

The removal of a nitrogen atom can also be considered on a peripheral position of the heptazine unit, creating a defect on the edge of the unit and the formation a new C–C bond (structure **1**.**b**; N-vac Heptazine Edge Radical). Structures **1**.**a** and **1**.**b** are expected to mimic the defects present in amorphous CN.

A first model for an oxidized carbon nitride was then designed, which has a pyran moiety inside of a sub-ring of a heptazine (**2**.**a**; N-vac "Pyran-like" Radical), where a radical center is always present in the structure. The selection of such a functional group is due to the hypothesis that oxygenated groups tend to form on the surface of the catalysts and, although the most usually detected ones are hydroxyls and carboxyls[4], a IR stretching band at 1100 cm^{-1} assigned to a C–O bond was also observed[5,6]. For this reason, a nitrogen atom at the lower corner of a heptazine unit was substituted with an oxygen, without disrupting the overall structure. The creation of another oxidized structure consists in breaking one C–O bond in the above system, which generates a carbonyl group and a radical center on the carbon atom that undergoes the cleavage (**2**.**b**; N-vac "Carbonyl-like" Radical).

In order to represent defects formed upon a reductive thermal treatment, structure **3**.**a** (N-vac Heptazine Bi-Radical ($–NH_2$ group)) is conceived as follows: two of the N–C bonds connecting the central nitrogen atom of the heptazine ring are cleaved, leaving a single C–N bond that is then saturated by hydrogen atoms, thus generating an $–NH_2$ group. The model is formally a bi-radical, since the carbon atoms that experience the cleavage are not saturated by hydrogens. Finally, another model for the reduced carbon nitride is conceived by cleaving the N-bridging point among three heptazine units and saturating with hydrogen atoms the nitrogen atom and one of the carbon atoms that experience the cleavage, whereas the one belonging to the third heptazine unit is left unsaturated, thus a radical center (**3**.**b**; Disconnected Heptazine Radical).

Table 4–2: Descriptive nomenclature of the various CN defective forms used in this work along with their reference numbers. The reference numbers correspond to the respective CN structures from Figure 4–5 and are hitherto used to indicate the specific CN species. The nature of the type of defect present on the CN surface is also reported for clarity.

Ref	**Type**	**Description of the CN surface**
P.0	Pristine	*g*-C_3N_4-Pristine
1.a	*am*. CN	CN-N vacancy at the center of a heptazine unit Nature of defect: radical with one unpaired electron
1.b		CN-N vacancy at the edge of a heptazine unit Nature of defect: radical with one unpaired electron
2.a	*ox*. CN	Oxygen substitution at the edge of a heptazine unit: pyran-like form Nature of defect: radical with one unpaired electron
2.b		Oxygen substitution at the edge of a heptazine unit: carbonyl form Nature of defect: radical with one unpaired electron
3.a	*red*. CN	Disconnected CN network, with N-C bonds cleaved at the center of a heptazine unit Nature of defect: radical with two unpaired electrons (bi-radical form)
3.b		Disconnected CN network, with N-C cleaved at the edge of a melamine unit Nature of defect: radical with one unpaired electron

Following the same rationale of the above-mentioned structures, the corresponding molecular equivalents are built (Fig. 4–6). Their size is close to that of the unit cell of the periodic calculations, so that the results obtained with the two approaches can be compared.

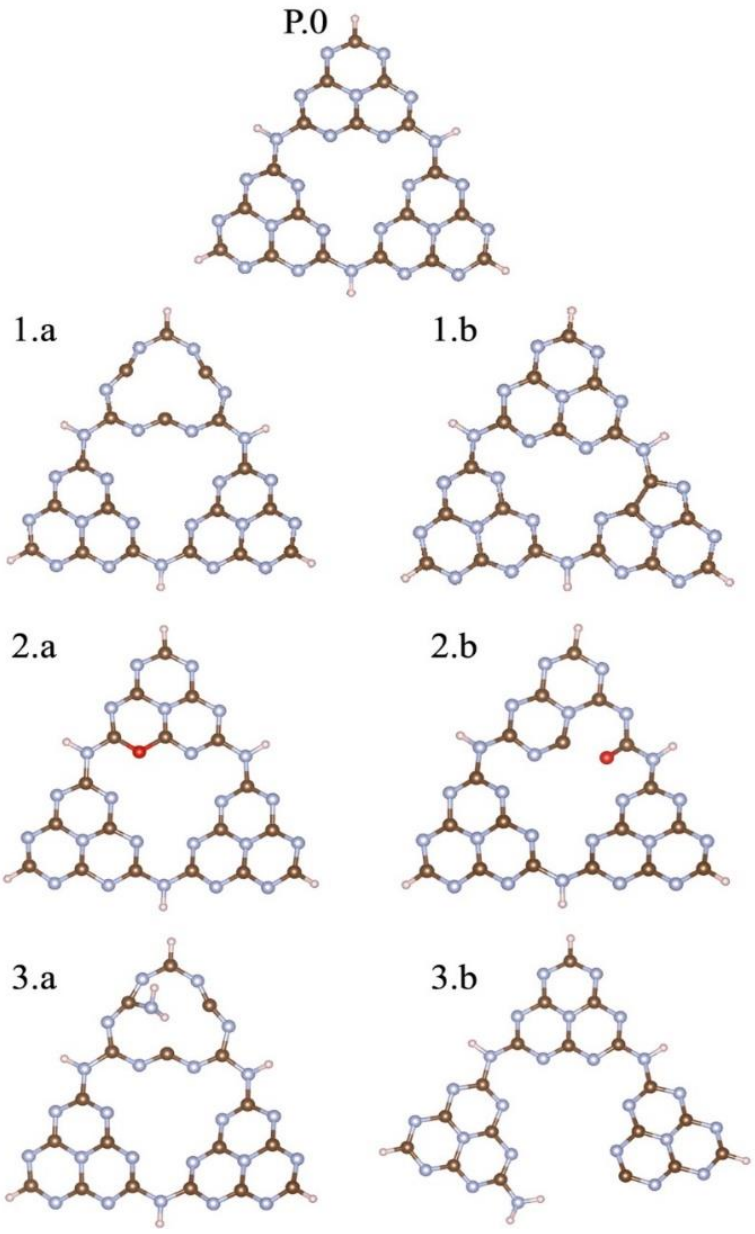

Figure 4–6: Molecular equivalents of carbon nitrides. **P.0** pristine; **1.a** N-vac Heptazine Radical; **1.b** N-vac Heptazine Edge Radical; **2.a** N-vac "Pyran-like" Radical; **2.b** N-vac "Carbonyl-like" Radical; **3.a** N-vac Heptazine Bi-Radical ($-NH_2$ group); **3.b** Disconnected Heptazine Radical.

4.5 Electronic structures and spin density of the carbon nitrides

The electronic structures computed for the periodic models of the pristine and defective CNs are collected in Figure 4–7 as Density of States plots (DOS). The red curves correspond to the α spin population and the blue ones to the β spin population. The zero of the energy scale is the Fermi

Level, *i.e*. the highest occupied level. Pristine *g*-C_3N_4 features perfectly symmetrical spin populations, as expected for a closed-shell system and a band-gap of ≈ 2.8 eV. In contrast the defective forms generally show additional states appearing in the band-gap. Structure 1.a shows an α state at 1.2 eV from the conduction band (CB) edge, which is related to a localized occupied defect level, whereas its corresponding unoccupied electronic level merges with the CB edge. In structure 1.b, an occupied α state appears at 1.8 eV from the CB while the corresponding unoccupied level (empty β state) is positioned within the band-gap at ≈ 0.6 eV from the CB. In structure 2.a, the occupied radical defect level is positioned at ≈ 0.9 eV from the CB, whereas in structure 2.b it merges with the top of the valence band (VB), with its empty level (β state) being positioned at ≈ 0.5 eV from the CB. Structure 3.a features two occupied radical defect levels with opposite spins in the gap. This is a bi-radical structure, as confirmed by the ground-state broken-symmetry calculation, with an energy difference between the α and β states of ≈ 0.5 eV. In structure 3.b, the occupied defect level lies very close (≈ 0.2 eV) to the VB edge.

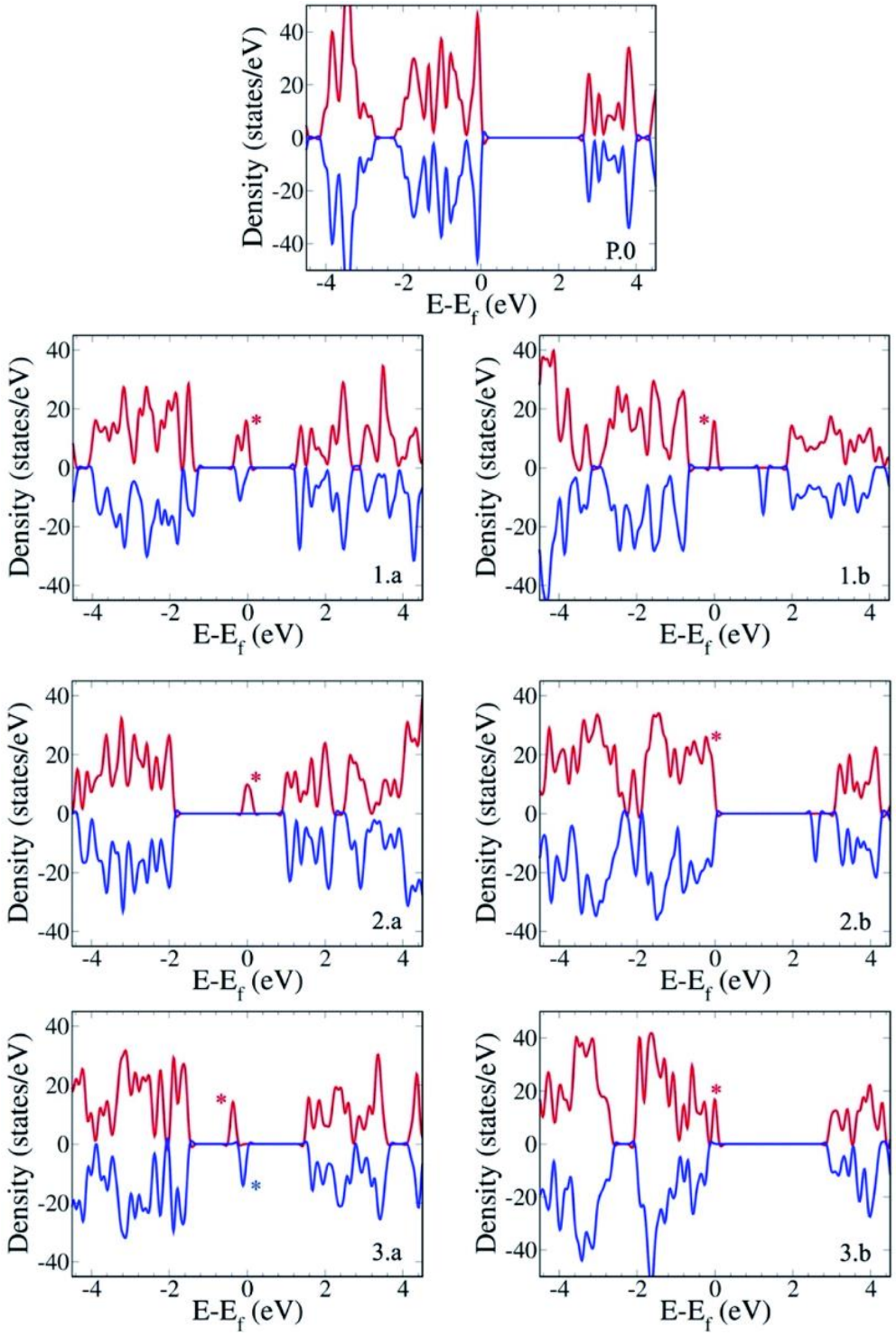

Figure 4–7: Electronic structures of the periodic models of carbon nitrides. **P**.**0** pristine; **1**.**a** N-vac Heptazine Radical; **1**.**b** N-vac Heptazine Edge Radical; **2**.**a** N-vac "Pyran-like" Radical; **2**.**b** N-vac "Carbonyl-like" Radical; **3**.**a** N-vac Heptazine Bi-Radical (–NH_2 group); **3**.**b** Disconnected Heptazine Radical. The positive (red) and negative (blue) density-of-states curves correspond to the α and β electron densities, respectively. The zero of the energy scale, *i.e*. the Fermi level, corresponds to the highest-occupied electronic state. Electronic energy levels corresponding to the localized occupied defect states at the Fermi level are indicated by an asterisk.

The electronic structure of the pristine and defective molecular CN models, obtained with pristine and modified heptazine units, shows a very good quantitative agreement with the periodic CN forms in terms of the electronic structure, energy gap and orbital symmetry, implying the transferability between the periodic and the molecular approaches. More specifically, it can be seen that the Highest Occupied Molecular Orbitals (HOMOs) of periodic and molecular models are well-localized in the defective part of the structures (Fig. 4–8, 1.a, 1.b, 3.a, 3.b), where the radical centers are. In contrast, the Lowest Occupied Molecular Orbitals (LUMOs) are delocalized over the rest of the structures. This picture emerges in both molecular and periodic models, confirming that the electronic distribution observed in such carbon nitrides is peculiar and that the defect states of the radical structures may play a crucial role in the interaction with C_4F_9–I. Indeed, it is the nature of the localized radical defect states present on the surface of carbon nitrides that is expected to generate a significant and specific binding interaction with the perfluoroalkyl iodide reagent, which subsequently modulate the photo-induced charge transfer from the surface of carbon nitrides to C_4F_9–I. It is to be noted that CN samples prepared by direct thermocondensation of precursors could form a melon-based structure, as reported previously. A melon-based carbon nitride principally represents a one-dimensional (1D) class wherein some of the heptazine sub-units form 1D polymer strands and the other heptazine sub-units align in a zigzag manner due to a hydrogen bonding network with the nitrogen atoms in the 1D strands, resulting in an interconnected network of heptazine units over a flat basal plane. The periodic and the molecular models considered in this work represent the two limit structures of a CN surface, namely, the periodic monolayer represents the result of the complete crosslinking of a melon model into a two-dimensional (2D) structure whereas the molecular model is the zero-dimensional (0D) representation of independent heptazine units, which are also present in the melon-like 1D

structure. As both the defective periodic (2D) and molecular (0D) models show a similar electronic structure (see Fig. 4–8 and 4–9 for details), we believe that the conclusions drawn from this work could be extended to other CN forms, in particular the melon-based 1D carbon nitride structures.

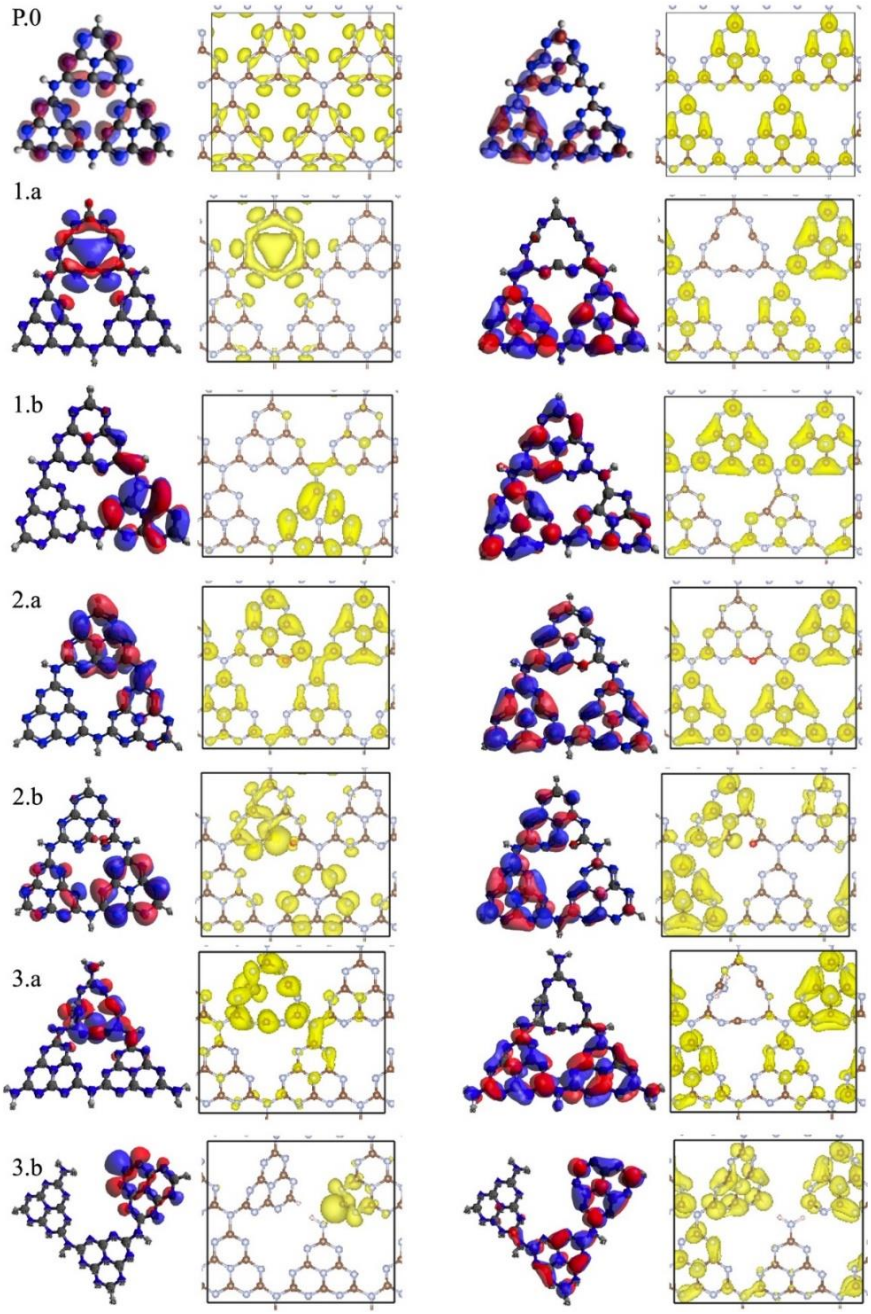

Figure 4–8: Molecular (left side of each panel, B3LYP/6-311G(d,p)) and crystalline (right side, PBE/PAW) orbitals of CN in its pristine (P0), radical - reduced/amorphous (1.a/b), radical -oxidative (2.a/b), disconnected (3.a/b). For clarity, only the orbitals of mid-gap defect state (HOMO, left column) and LUMO (right column) orbitals are shown.

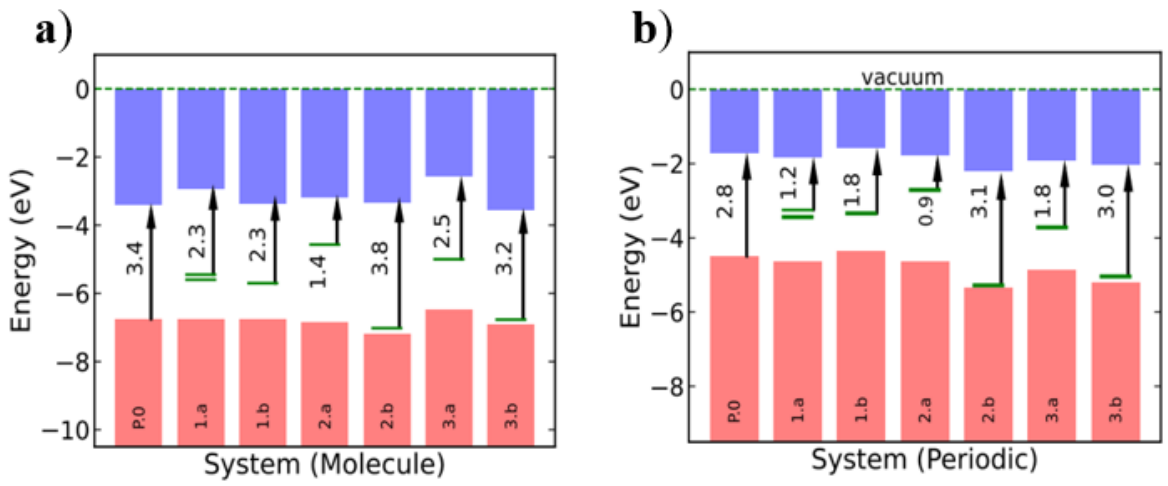

Figure 4–9: Electronic structure of (**a**) left: molecular (B3LYP/6-311G(d,p)) and (**b**) right: periodic CN forms (PBE/PAW) in its pristine, radical - reduced/amorphous, radical -oxidative, radical-disconnected, along with the isolated C_4F_9-I molecule. A very good agreement was observed between the periodic structures and their molecular equivalents.

Figure 4–9 summarizes the electronic structure calculations. In the radical models, the presence of the intra-gap states is expected to reduce the energy required to promote one electron to the conduction band, with respect to pristine *g*-CN. This will be useful in terms of catalytic efficiency, as it will be shown below.

It is also of interest to analyze the computed spin-density distributions on various defective CN forms. These systematically show larger spin densities on carbon atoms, along with smaller contributions on the nitrogen atoms. This result concurs with the EPR data, which indicate that all the CN structures (including pristine CN) contain radical carbon species. This is also consistent with the molecular models, for which the computed spin density is shown in Figure 4–10, with the highest density sites circled in red. Importantly, the ^{14}N 2D-EPR experiment performed on *am*. CN (Fig. 4–10, next to the molecular models) provides evidence for a small ^{14}N hyperfine coupling ($A_{max} \approx 1$ MHz), consistent with the delocalization of the unpaired electron wave function over a number of nitrogen atoms.

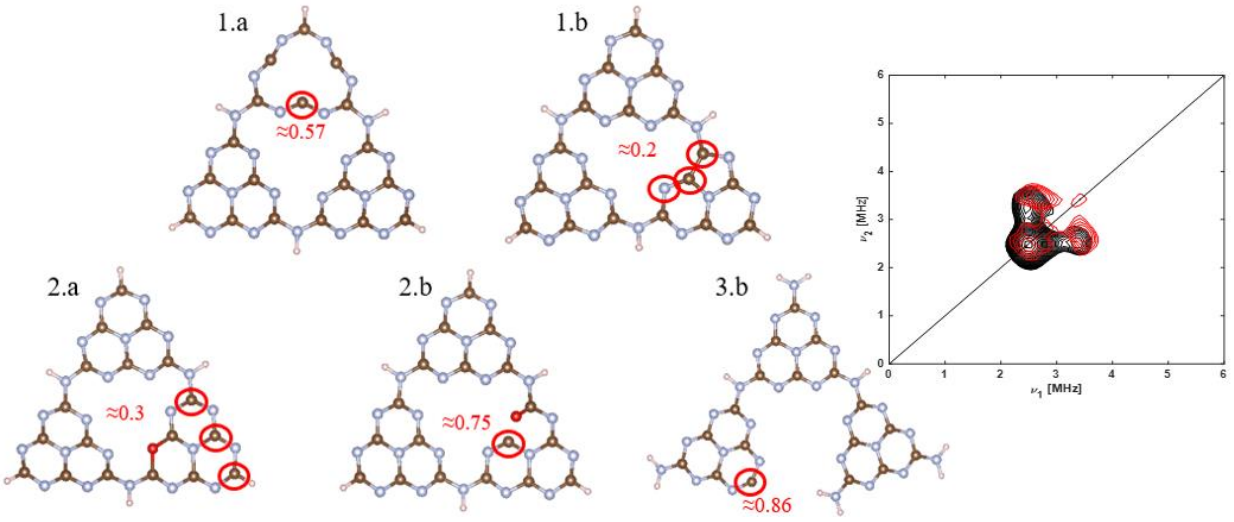

Figure 4–10: Spin density computed for the molecular models (B3LYP/6-311G(d,p): **1**.**a** N-vac Heptazine Radical, **1**.**b** N-vac Heptazine Edge Radical, **2**.**a** N-vac "Pyran-like" Radical, **2**.**b** N-vac "Carbonyl-like" Radical and **3**.**b** Disconnected Heptazine Radical. Aside, Q-band ^{14}N HYSCORE of the amorphous CN recorded at 110 K.

Although the spin density displays a more localized character for the radical defects on carbon atoms, a delocalization on nitrogen atoms also appears in some cases, for instance in structure 1.b, consistent with the EPR hyperfine coupling data.

4.6 Adsorption of C_4F_9–I on the carbon nitrides

The perfluoroalkylation reaction is expected to start with an initial interaction between the carbon nitride surface and C_4F_9–I. A series of combined systems are hence designed, given that the reaction is performed in solution and that carbon nitrides act as heterogeneous kind of catalysts. This justifies the approach "*in space*" of one C_4F_9–I molecule with the periodic models for pristine and defective carbon nitrides, which have then built close to one another prior to optimization. The adsorption geometry and energy (left panels in Fig. 4–11) as well as the electronic structure of those systems (middle and right panels) are then calculated.

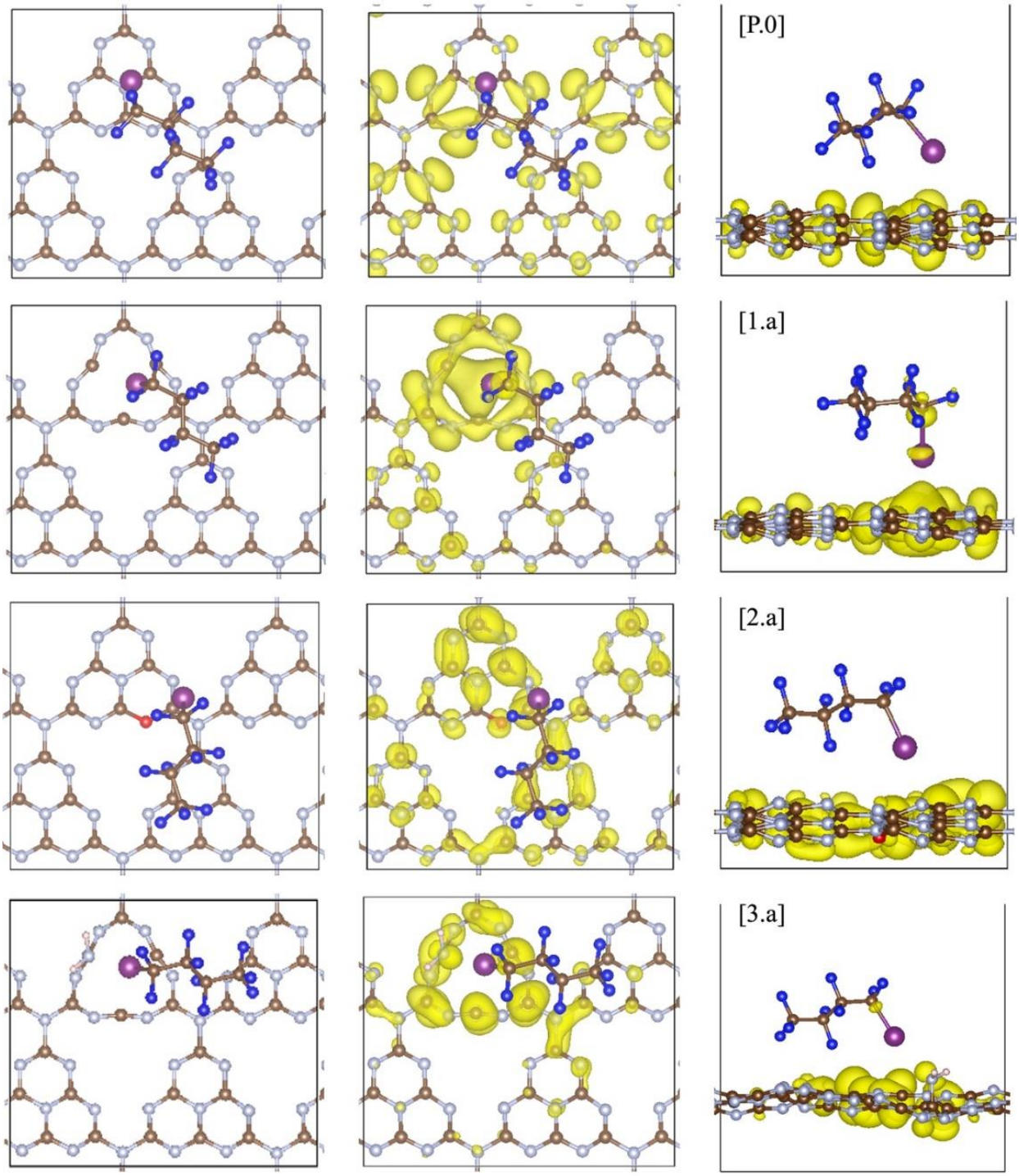

Figure 4–11: Adsorption of C_4F_9–I on the periodic models of carbon nitride: [**P**.**0**]: pristine + C_4F_9–I; [**1**.**a**]: N-vac Heptazine Radical + C_4F_9–I; [**2**.**a**]: N-vac "Pyran-like" Radical + C_4F_9–I; [**3**.**a**]: N-vac Heptazine Radical (–NH_2 group). Left: adsorption geometry; middle and right: wavefunction plots (HSE06) at the Fermi level (highest-occupied electronic state).

The adsorption energy of C_4F_9–I is ≈ 6 kcal/mol on the pristine *g*-C_3N_4 surface (structure P.0) but it has significantly higher values when radical defects are present. More specifically, for the *am*. CN forms (structures 1.a and 1.b), the adsorption energy of C_4F_9–I ranges from ≈ 11 kcal/mol to ≈ 17 kcal/mol, the highest value being found when a nitrogen vacancy is present in the middle of a heptazine unit (structure 1.a). In contrast, when oxygenated defects (pyran/carbonyl-like) are present on the CN surface, the adsorption energies are reduced to ≈ 8 kcal/mol. The adsorption energies of C_4F_9–I on the molecular CN models are in good quantitative agreement with the periodic models (see Table 4–3). This decrease in adsorption energy for oxygenated defects, despite the radical nature of these defects, could be attributed to the electrostatic repulsion between the oxygen and iodine atoms.

Table 4–3: Adsorption energies (in kcal/mol) of the C_4F_9–I molecule adsorbed on the CN surface in its pristine and defective forms, show a quantitative agreement between the periodic and molecular models.

Combined systems	**$E_{ads.}$**	
	Periodic	Molecular
P.0	6.1	5.5
1.a	17.4	15.6
1.b	11.2	10.5
2.a	8.1	8.1
2.b	7.06	7.2
3.a	12.5	14.5
3.b	11.4	14.2

In addition, the strong adsorption of C_4F_9–I on most *red*./*am*. CN surfaces (structures 1.a/b and 3.a) is also associated with a: (i) non negligible ground-state partial charge-transfer from the CN surface to the C_4F_9–I molecule (≈ 0.1q) and (ii) a small elongation of the carbon-iodine (C–I) bond of the C_4F_9–I molecule, of ≈ 0.06 Å. Interestingly, the adsorption energies also reflect a variation in the net bond order of the iodine atom: the highest bond order on iodine is observed when the C_4F_9–I molecule is adsorbed on CN surfaces containing nitrogen vacancies at the center of the

heptazine unit (structures 1.a and 3.a, and Table 4–4). This is an indication of the stronger interaction of the iodine atom with the surface defects in these systems. In addition, a variation of net bond order is also observed on the two fluorine atoms that are in proximity to the iodine atom. The relative change in the bond order of these fluorine atoms for different defect types compared to pristine *g*-C_3N_4 is also the highest for the CN surfaces containing a nitrogen vacancy at the center of the heptazine unit (Table 4–4).

Table 4–4: Adsorption energies ($E_{ads.}$), Bond Orders, C–I bond lengths and partial charge-transfers computed for all CN + C_4F_9–I combined systems.

Ref.	**$E_{ads.}$** (kcal/mol)	**Bond Order**		**C-I Bond length** (Δd, Å)	**Partial charge transfer** (∂q)
System		I	ΔF		
P.0	6.1	1.28	-na-	-na-	+0.03
1.a	17.4	1.57	0.20	0.061	-0.10
1.b	11.2	1.38	0.05	0.051	-0.07
2.a	8.1	1.35	0.04	0.006	-0.01
2.b	7.0	1.21	0.01	0.004	-0.01
3.a	12.5	1.51	0.15	0.051	-0.10
3.b	11.4	1.35	0.1	0.008	-0.03

The matching between the increased adsorption energy of the C_4F_9–I molecule on defective surfaces representing the amorphous and reduced CNs and the relative variation in the bond orders of iodine and fluorine atoms well correlates with the variation in the experimental ^{19}F-NMR T_1/T_2 ratios[1], *i.e*. the relaxation times of the pulse pattern set up in the measurement. The highest T_1/T_2 ratios are observed for the amorphous/reduced CN forms. More specifically, these earlier studies, using perfluorohexyl iodide as a probe molecule, reported higher ^{19}F-NMR T_1/T_2 ratios for *am*. CN and *red*. CN forms compared to pristine-/*ox*. CN forms, pointing to stronger molecule/surface interactions in the former systems. These strong interactions between the defective/modified CN surface and the perfluorohexyl iodide molecule, were hypothetically ascribed to the formation of

halogen bonding (N/I) between the freely accessible nitrogen (N) atoms from the defective amorphous CN surfaces and the iodine(I) atom of the probe molecule.

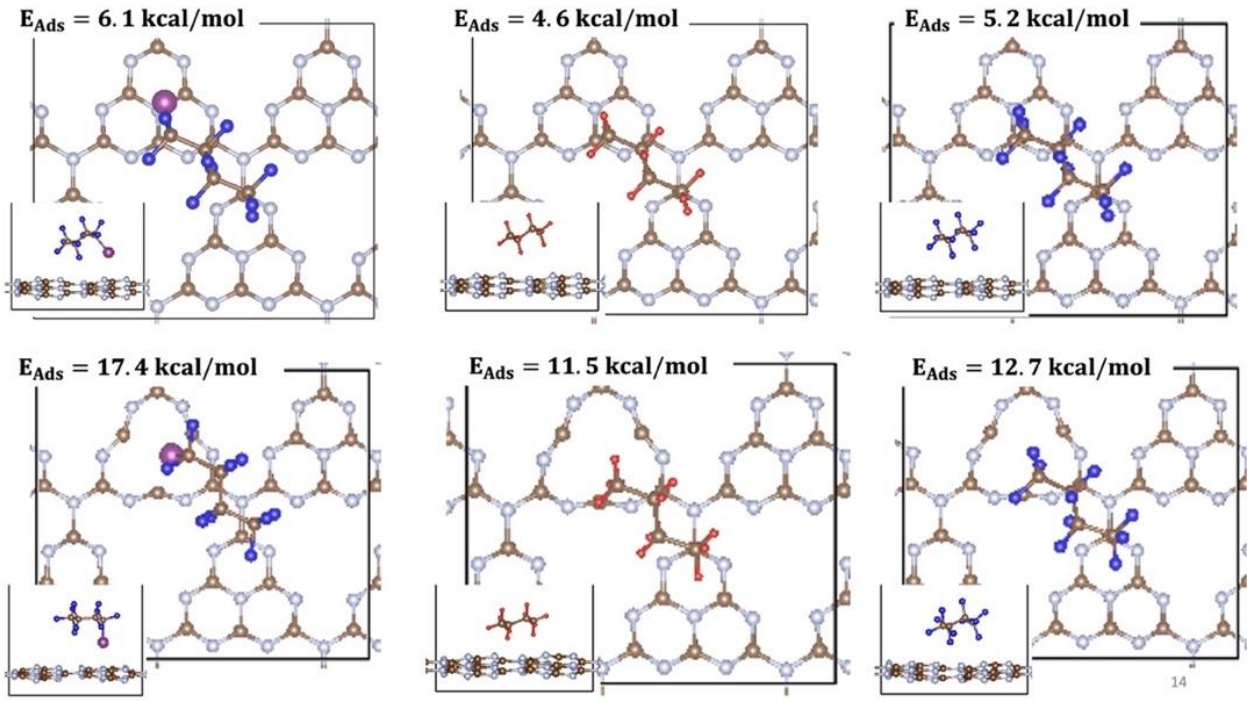

Figure 4–12: Adsorption of C_4F_9-I (left), C_4H_{10} (center) and C_4F_{10} (right) molecules on (top) pristine *g*-C_3N_4 and (bottom) a defective CN surface containing a nitrogen vacancy at the center of the heptazine unit (PBE/PAW). Iodine, Fluorine and Hydrogen atoms are represented with magenta, blue and red colors, for clarity.

To validate this hypothesis, C_4F_9–I, C_4F_{10} and C_4H_{10} were considered as probe molecules and their interactions on the pristine *g*-C_3N_4 surface (structure P.0) and on the *am*. CN surface containing a nitrogen vacancy at the center of the heptazine unit were computed (structure 1.a), as shown in Figure 4–12. On the pristine *g*-C_3N_4 surface, all the three probe molecules show a similar adsorption energy in the order of ≈ 4.5 to 6 kcal/mol. On the *am*. CN surface, their adsorption energies are larger, ranging from ≈ 11.5 kcal/mol to ≈ 17.5 kcal/mol. Of the three probe molecules adsorbed on the *am*. CN surface, C_4F_9–I has the largest adsorption energy (17.4 kcal/mol) while both C_4F_{10} and C_4H_{10} molecules show comparatively smaller adsorption energies of 12.7 and 11.4 kcal/mol, respectively. In addition, both C_4F_{10} and C_4H_{10} molecules adsorbed on *am*. CN surfaces are characterized by a negligible partial charge transfer between the surface and molecule (≈ 0.01

∂q) and no variations are observed: (i) in the bond orders of fluorine or hydrogen atoms; (ii) in the C–F/C–H bond lengths. In contrast, C_4F_9–I adsorbed on the *am*. CN surface shows larger variations in terms of partial ground-state charge transfer (∂q), a relative change in the bond order of fluorine atoms (Δ*F*) and a relative change in the C–I bond length (Δ*d*), as shown in Table 4–4, and consequently shows the highest adsorption energy, which is indicative of the strong interaction between the C_4F_9–I molecule and the defective CN surface. It therefore follows that the increased interaction between the defective CN surface and C_4F_9–I does not appear to be related to a conventional halogen bonding between the freely available nitrogen atoms from the defective CN surface and the iodine atom of the molecule, as hypothesized previously based on the increased experimental ^{19}F-NMR T_1/T_2 ratios. Instead, the calculations indicate that this results from a more complex interaction mechanism involving a reorganization of the electronic density on the terminal iodine. The reorganization is characterized by: (i) a partial ground state charge transfer from the defective CN surface to the molecule; (ii) an increase in the C–I bond length; and (iii) a consequential increase (decrease) in the bond order (length) between carbon and fluorine atoms neighboring the iodine atom. These specific interactions between the C_4F_9–I molecule and the defects present on the CN surface could indeed be manifested into an increase in ^{19}F-NMR T_1/T_2 ratios, observed experimentally.

4.7 Excited-state calculations on C_4F_9–I/CN systems

In Figure 4–4, the reaction mechanism shows a second step after the initial ground-state interaction between carbon nitride and C_4F_9–I, where the supply of light brings the catalyst to an excited state that can be intuitively described as the promotion of one electron into the conduction band. At that point, that electron can be transferred from the CB of carbon nitride to the molecule, which then undergoes an homolytic cleavage, becoming a radical. To model the initial step, the optimized

combined systems "CN + C_4F_9–I" described above are now reused for calculating the excited-state electronic structure, focusing on the theoretical optical absorption spectra of the CN materials and on the hole/electron density distribution in the excited "CN + C_4F_9–I" systems.

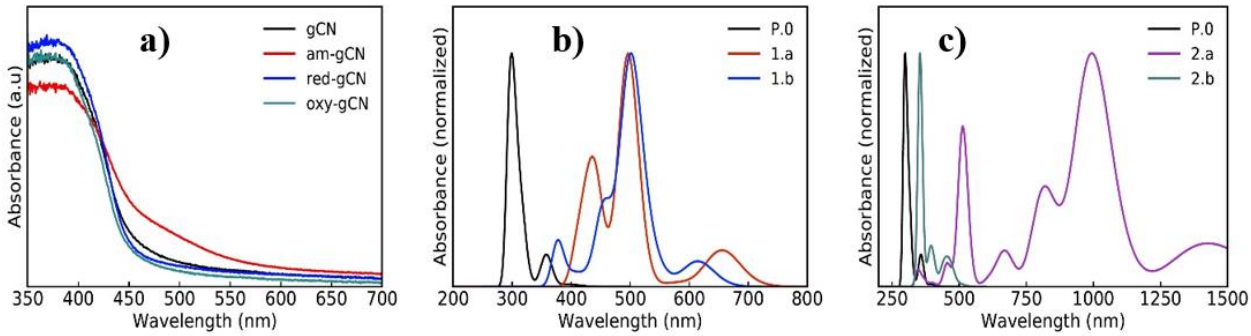

Figure 4–13: **a)** Experimental UV-vis. absorption spectra (HSE06/6-311G(d,p)) of pristine (*g*-C_3N_4), amorphous (*am*. CN), reduced (*red*. CN) and oxidized (*ox*. CN) carbon nitrides. **b)** and **c)** theoretical UV-vis. absorption spectra of all models.

Figure 4–13 shows the experimental and theoretical UV-vis. absorption spectra. The first ones show intense absorptions in the UV range and tails in the visible and near infrared region (NIR). *am*. CN clearly features a broader absorption capacity in the visible range, unlike the other CN forms. Theoretical UV-vis. spectra are used as a term of comparison. These show that, consistently, *g*-C_3N_4 mainly absorbs in the UV range, showing an intense band at 300 nm and a small one at ≈ 350 nm. The defective structures feature strong absorptions in the visible and the NIR region of the spectrum, with 1.a showing a noticeable band at ≈ 450 nm and, along with 1.b, a strong band at 500 nm. Beyond these values, small but still observable absorptions are present. The disconnected structure 2.b does not seem to absorb much in the visible but rather the pyran-like model shows intense bands in the infrared. Although this is unexpected for systems like carbon nitride, the interpretation of such a trend was found in the possibility that oxidized carbon nitrides can act as internal "push-pull" systems, where the charge moves within their structure[5].

For the description of the hole (h^+) and electron (e^-) distributions for the transitions of interest, Attachment and Detachment Density Matrixes were computed. In Figure 4–14, all CN + C_4F_9–I combined systems are shown. The light-blue and yellow bulbs on the structures indicate the hole and electron localization of each state, respectively. Among all the excited states computed for *g*-CN, the one appearing at 353 nm is reported. The charge redistribution associated to that transition clearly remains confined within the structure of carbon nitride. This suggests that pristine *g*-C_3N_4 is not favoring the electron-transfer to the fluorinated molecule. In contrast, the N-vacant radical model (1.a) transfers a considerable amount of electron density to the molecule, in particular around the C–I bond, with a d_{z2}-like character. In addition, that transition appears at 500 nm, *i.e.* in the visible range, in line with the experimental conditions. This further corroborates the hypothesis according to which the C-I bond can be cleaved in order to generate the fluorinated radical. This also holds for the N-vacant Edge model (1.b) which is also prone to transfer some charge to the C–I bond of C_4F_9–I, again for the transition appearing at 500 nm. Contrarily to what observed so far, the pyran-like and N-vacant –NH_2 models do not seem to be effective in conveying the charge to the molecule. If one considers again the theoretical UV-vis. spectra in Figure 4–13, a contradiction seems to appear, because the purple spectrum of the pyran-like model (2.a) presents very intense bands in the infrared. However, those defects act like internal "push-pull" systems[7] (the hole is positioned at the top right part of the pyran-like model and the charge in the opposite part) and those transitions do not involve charge transfer to the adsorbed molecule. They are therefore not likely to promote the photochemical reaction.

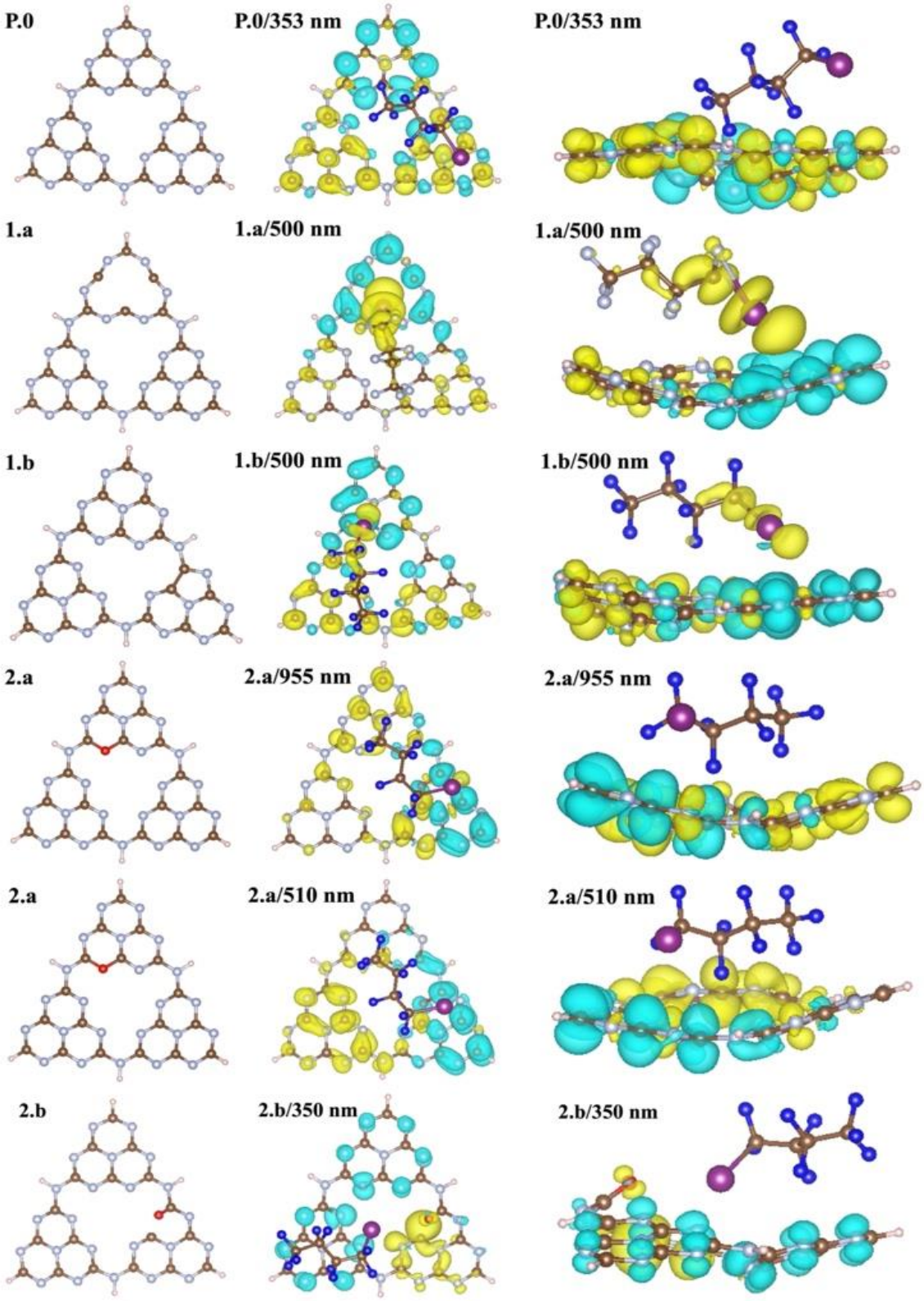

Figure 4–14: Attachment/Detachment Density distributions (HSE06/6-311G(d,p)) of the "CN + C_4F_9–I" models. The hole density is represented in light blue and the electron density in yellow.

Very interestingly, upon electron transfer from the CN surface, the C_4F_9–I molecule undergoes an elongation of the C-I bond length by ≈ 1 Å, with ≈ 80% of the charge localized on the iodine atom, while the unpaired electron is strongly localized (≈ 65%) on the neighboring carbon atom (see Fig. 4–15). This is fully consistent with the mechanism proposed for the CN-assisted perfluoroalkylation of electron-rich aromatic compounds. Importantly, the modelling results suggest that the photo-induced electron transfer and C–I bond breaking reactions occur in a concerted way.

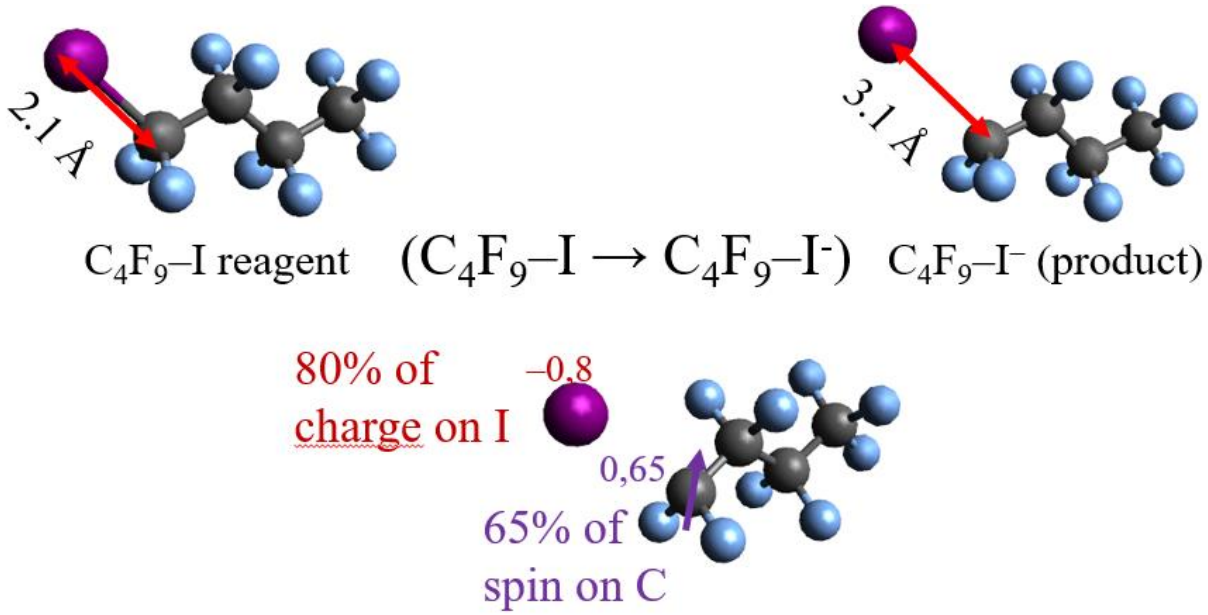

Figure 4–15: The elongation of the C–I bond of the nonafluoro–1–iodobutane after receiving the charge by carbon nitrides. Iodide: purple; carbons: grey; fluorines: light-blue.

4.8 Conclusions

To conclude, the modelling of the perfluoroalkylation of 1,3,5–trimethoxybenzene shows that a ground-state interaction between the carbon nitride materials and the substrate of reaction, C_4F_9–I, takes place. Pristine *g*-C_3N_4 does not seem to strongly interact with the substrate, whereas the defective structures generally have a higher degree of interaction, as shown by the adsorption energies computed. Consistently, the HOMOs reported in the combined systems "CN + C_4F_9–I"

are delocalized onto the substrate in the case of defective structures, especially N-vacant and N-vacant Edge radicals. Those radicals feature a more marked electronic density on carbon atoms, suggesting an electronic interaction between the two species at the ground-state mostly involving carbon atoms and not nitrogen atoms. The interaction established is more complex than a classical halogen bonding, as pointed out by the Bond Order analysis. In addition to the C-I bond, which experiences an elongation upon interaction with the defective structures, also the C–F bonds appear to elongate, hence also participating to the interaction.

The theoretical UV-vis. absorption spectra indicate which wavelengths can be involved in the photoelectron-transfer expected to happen. Pristine *g*-C_3N_4 only shows absorption only in the UV range whereas the defective models feature more marked visible absorptions. A clear separation between electron and hole densities is observed for the N-vacant and N-vacant Edge Radical models for the excited states corresponding to absorption around 500 nm. In contrast, no delocalization of electron density is observed for pristine *g*-C_3N_4 and for the pyran-like and N-vacant –NH_2 models. This clearly correlates with the photocatalytic activities measured experimentally and allows to identifying the types of defects that initiate the photo-induced reaction in this series of CN catalysts.

References

[1] Filippini G., Longobardo F., Forster L., Criado A., Di Carmine G., Nasi L., D'Agostino C., Melchionna M., Fornasiero P., Prato P., *Sci*. *Adv*., 6, (**2020**).

[2] G. Cavallo, P. Metrangolo, R. Milani, T. Pilati, A. Priimagi, G. Resnati, G. Terraneo, *Chem*. *Rev*., 116, (**2016**), 2478–2601.

[3] P. Metrangolo, G. Resnati, *Chem*. *Commun*., 49, (**2013**), 1783–1785.

[4] Bai J. Y., Wang L. J., Zhang Y. J., Wen C. F., Wang X. L., Yang H. G., *Appl*. *Catal*. *B*: *Environm*., 266, (**2020**), 118590.

[5] Wang H., Jiang S., Chen S., Li D., Zhang X., Shao W., Sun X., Xie J., Zhao Z., Zhang Q., Tian Y., Xie Y., *Adv*. *Mater*., 28, (**2016**), 6940–6945.

[6] She X., Wu J., Zhong J., Xu H., Yang Y., Vajtai R., Lou J., Liu Y., Du D., Li H., Ajayan P. M., *Nano Energy*, 27, (**2016**), 138–146.

[7] Song X., Li X., Zhang X., Wu Y., Ma C., Huo P., Yan Y., *Appl*. *Catal*. *B*: Environ., 268, (**2020**), 118736.

Chapter 5: Modelling the dual Ni-carbon nitride-catalyzed arylamination reaction

5.1 Objective of this study

As mentioned in chapter 2, carbon nitride materials (CNMs) can easily create a synergy with metallic complexes in dual photoredox cross-coupling reactions, where the former act as photocatalysts (PCs) performing the single electron-transfer to the latter, which acts as the catalytically active species. Despite the considerable literature production, the mechanism still has to be understood in details for these complicated reactions, which are even more challenging due to the intervention of light.

This chapter is aimed at elucidating some of the mechanistic critical steps in the photochemical arylamination reaction in the presence of a dual catalyst associating a CNM and a nickel complex. The particular case that will be modelled involves the model molecules methyl–4–bromobenzoate and pyrrolidine (see Fig. 5–1).

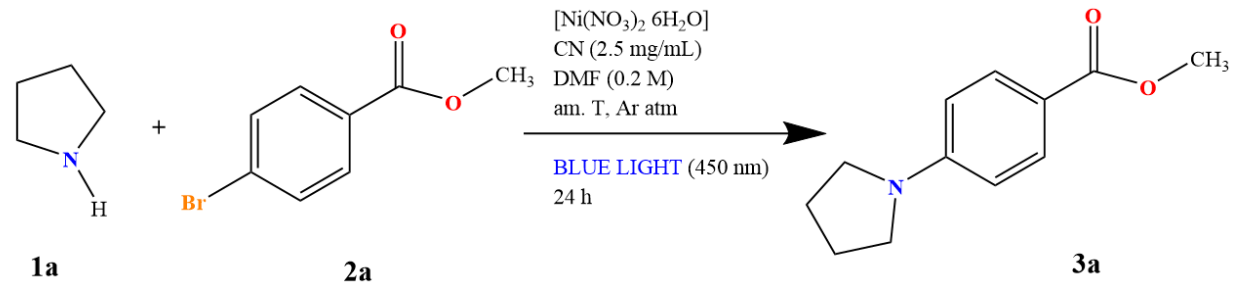

Figure 5–1: Amination of methyl–4–bromobenzoate in the presence of CN and a nickel complex.

Among the CNMs tested, a new microwave-treated carbon nitride was prepared (*mw*-CN), within the research group[1]. The purpose of the treatment is to generate specific defects in its structure, namely carbon vacancies, that can evolve into proper binding sites groups for the Ni species, specifically triazole and imine moieties. Details on the structural aspects were provided in chapter 4. The modified *mw*-CN has the structural requisites for boosting the catalytic efficiency, with

many entries of the scope of reaction going to (or approaching) completeness (see Table 5–1), therefore being more efficient than pristine *g*-C_3N_4 and other investigated modified CNMs.

Table 5–1: Catalytic efficiencies of various types of CNMs for the arylamination reaction. The details of the experimental protocol can be found in ref [1].

Entry	CN photocatalyst	Yield 3a (%)
1	*g*-C_3N_4	48
2	*am*-CN	7
3	*ox*-CN	24
4	*mw*-CN	87
5	*mw*-CN with Kessil lamp (456 nm)	97

In this work, Density Functional Theory (DFT) is employed in order to better characterize this new CN material and to provide insights into the fundamental features responsible of the higher catalytic efficiency. The mechanism proposed for the reaction is shown in Figure 5–2. It is hypothesized to comprise: (i) the coordination of a nickel (II) complex to carbon nitride; (ii) the photoexcitation of that functionalized CN, followed by: (iii) an internal charge transfer generating a nickel (I) species, which is released by the CN surface. Such a Ni complex then reacts with the halogenated aryl compound and enters a homogeneous catalytic cycle eventually leading to final product. This is an example of dual catalysis combining a photo-induced process and a “dark” cycle.

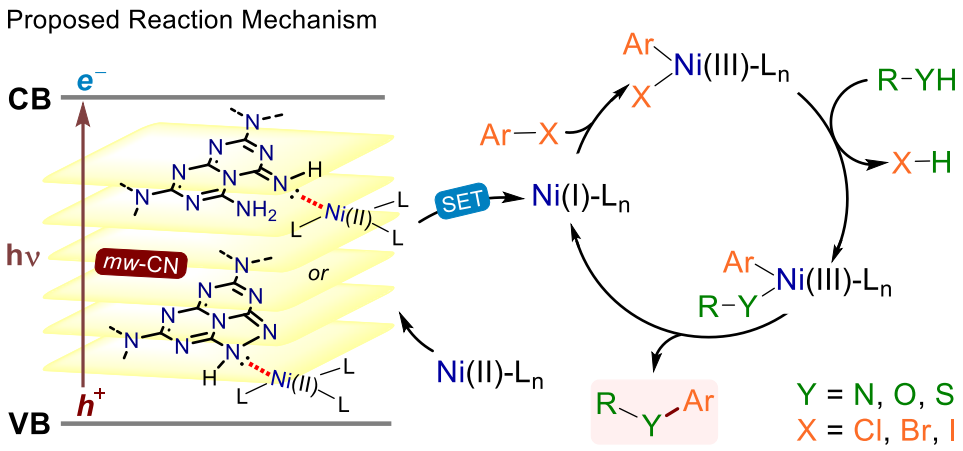

Figure 5–2: Hypothetical reaction mechanism involving carbon nitride and nickel complex catalysts.

The key (unresolved) questions that were addressed here by means of this modelling study are:

(i) the actual structure of the Ni(II) complex present in solution;

(ii) the nature of the interaction between that complex and the carbon nitride surface;

(iii) the nature of the optically-excited states, opening the possibility of electron transfer from carbon nitride to the nickel species upon light absorption.

5.2. Determining the nature of the nickel complex in solution

It is well known that nickel ions can be stabilized in solution through many coordinative environments and that those complexation equilibria are elusive to observe[2,3]. Nickel(II) is usually a hexa- or tetra-coordinated metal ion and, among the latter species, tetrahedral or square-planar geometries are the most frequently occurring ones[4,5]. The first part of the work therefore consists in the identification of the metallic complexes that are present in the reaction mixture. For that purpose, a joint experimental/theoretical approach was employed, combining optical spectroscopy measurements and DFT calculations.

The reaction conditions imply the dissolution of the starting nickel salt (nickel nitrate hexa-hydrate, $[Ni(NO_3)_2 \cdot 6H_2O]$), in *N*,*N*-dimethylformamide (DMF), the solvent used for the reaction. Since metallic complexes generally feature characteristic electronic transitions, UV-vis. absorption spectroscopy appears to be an adequate tool to obtain information about the coordinative situation of the nickel complexes in solution. Figure 5–3 shows the UV-vis. absorption spectrum of $[Ni(NO_3)_2 \cdot 6H_2O]$ in DMF. It features three distinct bands at ≈ 300, 400 and 700 nm, the last one being split in two peaks.

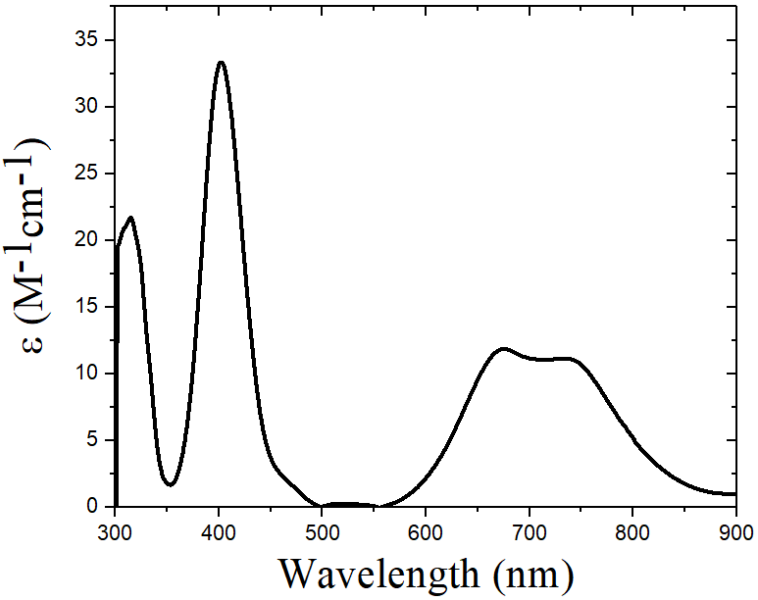

Figure 5–3: UV-vis. absorption spectrum of a 30 mM DMF solution of $[Ni(NO_3)_2 \cdot 6H_2O]$.

Despite the well-defined shape of such spectrum, no clear information can be deduced besides the molar extinction coefficient (ε, $M^{-1}cm^{-1}$), which is extremely low, about 35 $M^{-1}cm^{-1}$ for the highest band. Such low values are usually the signature of "*d–d electronic transitions*" (also known as Herzberg–Teller effect) which are typical for transition metal complexes[6,7]. These are forbidden excitations justified by violated spin rules, often associated to the spin-orbit coupling (SOC). This is a phenomenon arising due to the interaction of the angular momentum of an electron with its spin angular momentum, which often implies the mixing of non-interacting states (singlets

with triplets) or the removal of electronic degeneracy of states[8]. Therefore, SOC changes the spectroscopic behavior of molecules, by lightning up some dark states for example. They gain some intensity, albeit very low, probably because of slight structural distortions with respect to the perfect complex symmetry. A theoretical study about hetroannelated octatetraenes in the Franck–Condon and Herzberg–Teller approximations showed how the simulated $S_0 \rightarrow S_1$ and $S_0 \rightarrow S_2$ optical transitions can be hard to see, albeit with still appreciable oscillator strengths (0.005 and 0.06 respectively)[9].

To try to identify the chemical compound giving rise to the experimental spectrum, a number of Ni(II) complexes were considered for calculations. Their geometry was optimized and their optical absorption spectrum was calculated with TD-DFT. As the solvent of reaction is DMF, it appeared reasonable to consider that solvent molecules may displace the initial water ligands. A nickel complex containing six DMF molecules in octahedral configuration, with "+2" as total charge, was thus optimized, both in the singlet and triplet multiplicity. Figure 5–4 shows the singlet and triplet structures and Table 5–2 reports the most relevant bond lengths obtained from the optimization. The complexes appear as regular octahedra with six *O*-coordinated DMF ligands, but depending on the structure, changes in the bond lengths can be noticed. The bond lengths calculated for the triplet state are close to the values reported for a crystal of a hexa-coordinated DMF nickel complex[10], confirming the validity of our theoretical methodology. It can be reasonably hence concluded that the complexes are in a triplet state, as it normally happens for nickel hexa-coordinated transition metals[11].

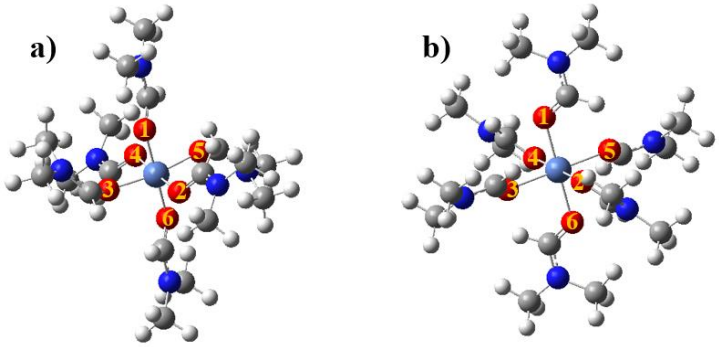

Figure 5–4: **a)** singlet and **b)** triplet hexa-coordinated DMF nickel complexes (B3LYP/Def2SVP; Ni: LanL2DZ).

Table 5–2: Bond lengths of the two hexa-coordinated nickel complexes with DMF.

Singlet		Triplet	
Bonds	**Bond lengths (Å)**	**Bonds**	**Bond lengths (Å)**
$Ni–O_1$	1.85	$Ni–O_1$	2.06
$Ni–O_2$	1.89	$Ni–O_2$	2.06
$Ni–O_3$	1.86	$Ni–O_3$	2.06
$Ni–O_4$	1.86	$Ni–O_4$	2.06
$Ni–O_5$	1.88	$Ni–O_5$	2.06
$Ni–O_6$	1.87	$Ni–O_6$	2.06

The excited-state electronic structure and the optical absorption spectra of the above two complexes were then calculated with TD-DFT. The lowest-energy excited states have either zero or vanishingly small oscillator strengths, as expected with *d–d transitions.* This is consistent with the very low extinction coefficients observed in the experimental spectra, as the oscillator strength is the equivalent of the molar extinction coefficient in theory[12]. In particular, zero intensity is found in the calculated spectra in the 600-800 nm region (see the spectrum of the singlet complex in Fig. 5–5), in sharp contrast with the experimental results. This discrepancy suggests that hexa-coordinated DMF complexes are not present in solution.

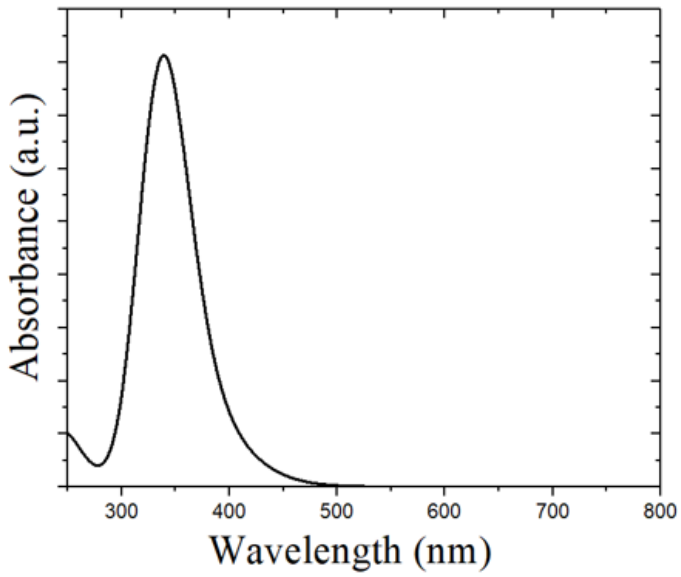

Figure 5–5: Theoretical UV-vis. absorption spectrum of the singlet hexa-coordinated DMF nickel complex (HSE06/Def2SVP; Ni: LanL2DZ).

Since the hexa-coordinated complexes did not provide any connection with the experimental absorption spectrum, we then turned to tetra-coordinated complexes, starting with a symmetric tetrahedral nickel complex coordinated by four DMF molecules. As illustrated in Figure 5–6 and Table 5–3, the optimized geometry of this complex is far from a typical tetrahedron, indicating that the tetrahedral coordination is not stable. Expectedly, the spectrum calculated for that structure does not agree with the experimental data.

Table 5–3: Bond angles around the Ni atom in the tetra-coordinated complex with DMF (B3LYP/Def2SVP; Ni: LanL2DZ.

Angles	Amplitudes (°)
O_1–Ni–O_2	94.7
O_1–Ni–O_3	100.0
O_1–Ni–O_4	97.2
O_2–Ni–O_3	97.2
O_3–Ni–O_4	96.1
O_2–Ni–O_4	160.3

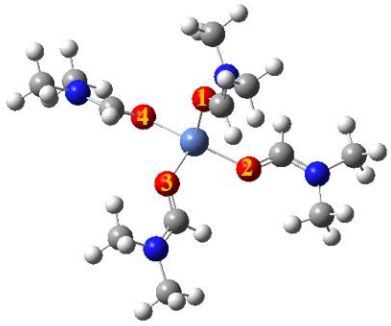

Figure 5–6: Tetra-coordinated DMF nickel complex, optimized starting from a tetrahedral geometry (B3LYP/Def2SVP; Ni: LanL2DZ).

When examining the structure of the complex more closely, it appears that the oxygen atoms of three ligands lie on a plane along with the nickel atom, whereas the fourth is perpendicular to that plane, and the angles between the coplanar ligands are somewhat close to 90°. This led us to the hypothesis that the actual complex may have a square-planar configuration. This hypothesis has been reinforced by EPR data obtained at the University of Torino by the group of Prof. Mario Chiesa: the spectra of samples made of a mixture of *mw*-CN and the nickel complex interacting with NO are best explained considering that the complex has a square-planar geometry, according to the result of a slightly distorted planar configuration obtained from the measurement. We then extended the calculations to a DMF complex in that geometry (Figure 5–7 and Table 5–4).

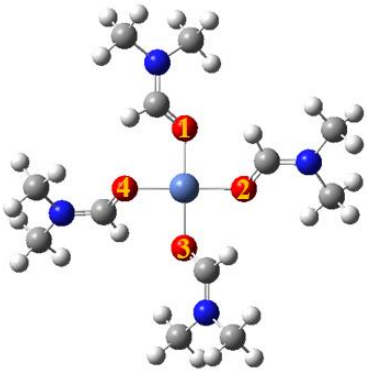

Figure 5–7: Square-planar $(DMF)_4$-Ni complex (B3LYP/Def2SVP; Ni: LanL2DZ).

Table 5–4: Bond angles around the Ni atom in the tetra-coordinated complex with DMF (B3LYP/Def2SVP; Ni: LanL2DZ).

Bonds	**Bond lengths (Å)**	**Angles**	**Amplitudes (°)**
Ni–O_1	1.8	O_1–Ni–O_2	90.4
Ni–O_2	1.8	O_1–Ni–O_3	175.6
Ni–O_3	1.8	O_1–Ni–O_4	90.9
Ni–O_4	1.8	O_2–Ni–O_3	89.5
		O_3–Ni–O_4	89.2
		O_2–Ni–O_4	178.7

The square-planar fashion mentioned above can be recognized when looking at the structure of the new complex. Four DMF ligands now lie on the same plane at 90° among one another around the nickel metallic center, featuring only small deviations in amplitudes from that values. In addition, the amplitude of the angle involving O_1, nickel and O_3 is close to the value of 180°. This is a small deviation from planarity obtained in the optimization calculation which is however still in accordance with the experimental EPR data, which indicate the presence of slightly distorted square-planar nickel complexes in the measurements.

In contrast to the other complexes, the calculated absorption spectrum for the square-planar complex shows a weak intensity band around 600 nm (see Fig. 5–8), originating from a couple of *d-d* excited states. This is consistent with the experimental spectrum of Figure 5–3 and constitutes a clear indication that the actual complex in solution is square planar, with DMF ligands. We will also consider that the same geometry is maintained for the other nickel complexes described below.

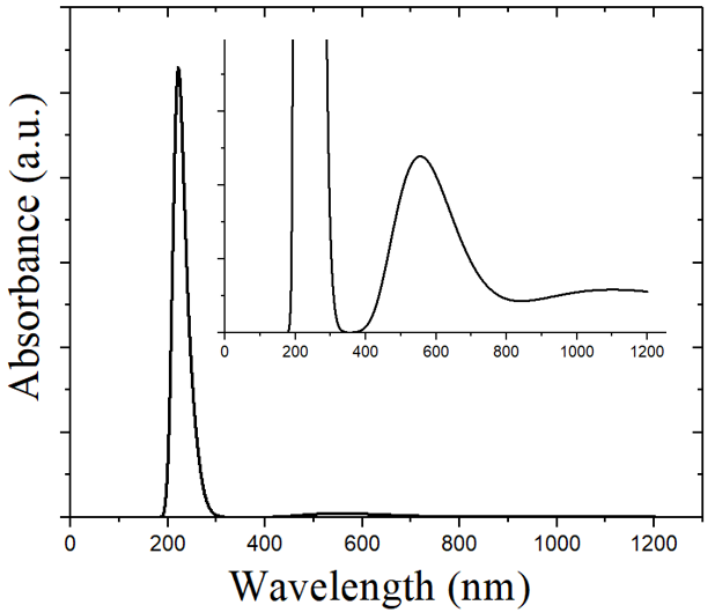

Figure 5–8: Calculated absorption spectrum for the square-planar $(DMF)_4$-Ni complex. Up-right panel: magnification of the visible region falling around 600 nm (HSE06/Def2SVP; Ni: LanL2DZ).

When the nickel catalyst is engaged in the arylamination reaction, it gets in contact with pyrrolidine, which could also act as a ligand to the metal ion via its nitrogen atom. To examine that possibility, titration experiments monitored by UV-vis. spectroscopy were performed. Figure 5–9 shows a set of spectra obtained upon the progressive addition of equivalents of pyrrolidine as the titrating agent in a 30 mM $[Ni(NO_3)_2 \cdot 6H_2O]$ DMF solution.

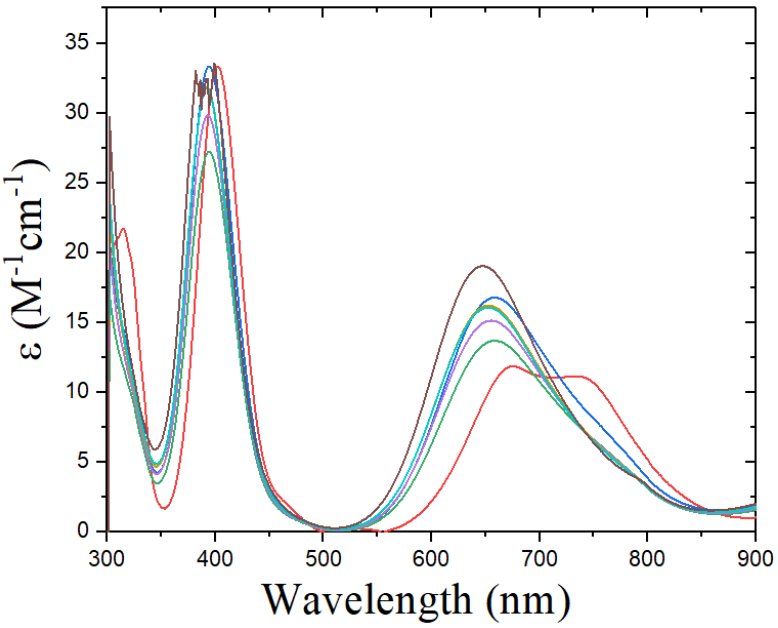

Figure 5–9: UV-vis. titration spectra of a 30 mM DMF solution of $[Ni(NO_3)_2 \cdot 6H_2O]$ with pyrrolidine. The red spectrum corresponds to $[Ni(NO_3)_2 \cdot 6H_2O]$ alone; the other spectra are recorded after addition of 1, 2, 3, 4, 5, 10 and 20 equivalents of pyrrolidine.

It can be noticed that the band centered at 700 nm is blue-shifting and increasing in intensity as the number of equivalents of pyrrolidine are added, whereas the band at 400 nm is only marginally affected. In addition, the splitting of the band at 700 nm is lost as pyrrolidine is added. It can therefore be deduced that pyrrolidine affects the electronic properties of the nickel complex, presumably as a result of its coordination to the metal and displacement of the DMF ligands. It is also noteworthy that the strongest changes in the spectrum are already apparent after addition of one equivalent of pyrrolidine.

In parallel to the experimental UV-vis. measurements, calculations were performed to determine the binding affinity of pyrrolidine towards nickel. For this purpose, the square-planar complex with DMF is progressively substituted by pyrrolidines. Figure 5–10 shows the structure of those compounds with up to three pyrrolidine ligands and Table 5–5 lists the formation energies, *i.e.*, the difference in total energy between the complex and its isolated components.

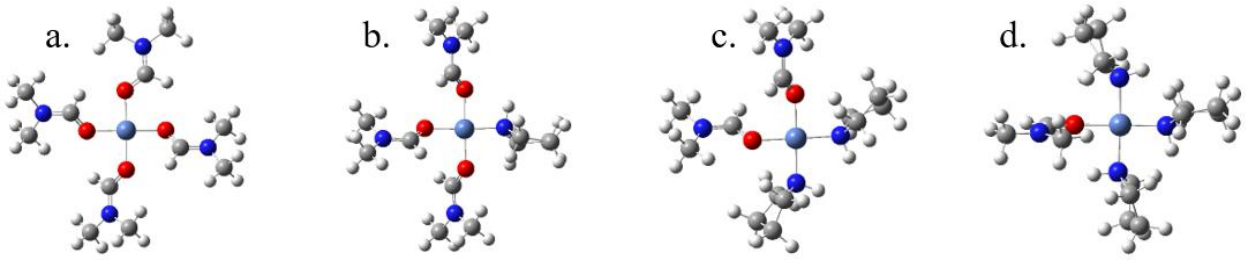

Figure 5–10: The progressive substitution of DMF ligands by pyrrolidine in square-planar nickel complexes (B3LYP/Def2SVP; Ni: LanL2DZ).

Table 5–5: Formation energies of the square-planar nickel complexes with an increasing number of pyrrolidine ligands (B3LYP/Def2SVP; Ni: LanL2DZ).

Complex	**Formation energies (kcal/mol)**
Ni_4_DMF	–97.0
Ni_3_DMF_1pyrr	–106.3
Ni_2_DMF_2pyrr	–112.3
Ni_1_DMF_3pyrr	–111.8

All complexes maintain their square-planar geometry and substituting one DMF ligand by a pyrrolidine stabilizes the complex by about 10 kcal/mol. This is consistent with the observation that the addition of pyrrolidine in the DMF solution of the complex modifies the absorption spectrum. The energy values also indicate that the increase in stability saturates upon further substation, presumably as a result of steric hindrance among the pyrrolidine ligands, since that molecule is significantly larger than DMF.

The visible part of the absorption spectra calculated for pyrrolidine-based complexes is reported in Figure 5–11 and details on the lowest-energy transitions are given in Table 5–6.

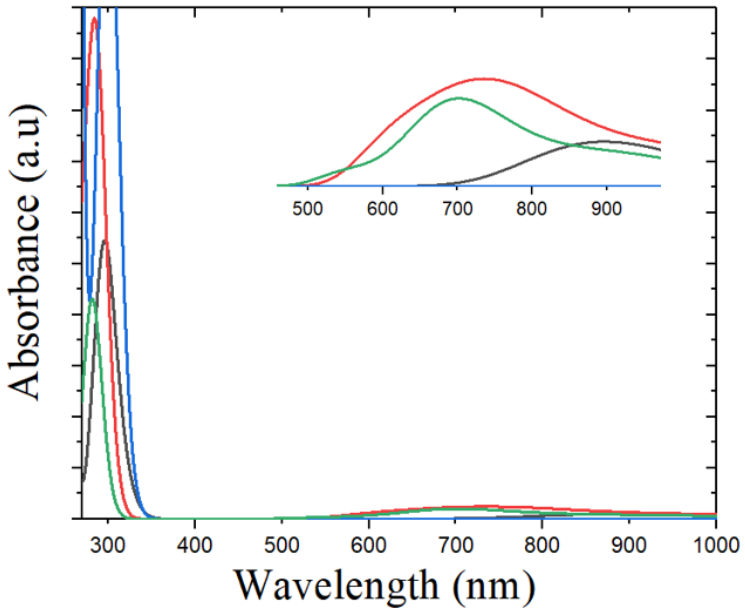

Figure 5–9: Theoretical UV-vis. spectra of the new square-planar nickel complexes. In **black**: Ni_4_DMF; in **red**: Ni_3_DMF_1pyrr; in **blue**: Ni_2_DMF_2pyrr; in **green**: Ni_1_DMF_3pyrr. Up-right panel: magnification of the visible region between 500–900 nm (HSE06/Def2SVP; Ni: LanL2DZ)..

Table 5–6: Wavelengths and oscillator strengths of the first four low-energy excited states of the Ni square-planar complexes (HSE06/Def2SVP; Ni: LanL2DZ).

Low-energy transitions											
Ni_4_DMF			**Ni_3_DMF_1pyrr**			**Ni_2_DMF_2pyrr**			**Ni_1_DMF_3pyrr**		
State	Wavelength (nm)	osc. strength	State	Wavelength (nm)	osc. strength	State	Wavelength (nm)	osc. strength	State	Wavelength (nm)	osc. strength
1	1270	0	1	1026	0.0002	1	932	0.0003	1	917	0.0002
2	908	0.0001	2	796	0.0004	2	688	0.0004	2	707	0.0002
3	890	0.0002	3	707	0.0004	3	680	0.0002	3	658	0.0001
4	658	0	4	616	0.0003	4	571	0	4	557	0.0001

When examining qualitatively the data in Table 5–6, it can be proposed that:

(i) the two states with non-zero oscillator strength in the Ni_4_DMF complex could correspond to the low-energy doubly-split band in the experimental spectrum;

(ii) upon substitution by one pyrrolidine, those two states shift to lower wavelengths (*i.e.* higher energy) and their oscillator strength slightly increases. State 4 also gains some oscillator strength. This evolution is similar to the changes observed in the experimental spectra during the titration experiments.

(iii) further substitution leads to a stronger blue shift of the excited states of interest, with no further increase of the oscillator strength.

Globally, these results clearly indicate that pyrrolidine participates to the coordination of the nickel ion. The titration experiments, the stability data and the analysis of the theoretical absorption spectra all suggest that the most probable complex hosts one pyrrolidine ligand along with three DMF molecules. We will thus consider that species (Ni_3_DMF_1pyrr) when investigating the interaction of the nickel complex with the carbon nitride surface in the following section.

5.3 Modelling the interaction of the nickel complex with the carbon nitride surface

Once that the structure of the nickel complex is established, an appropriate model for the *mw*-CN surface was defined. Similarly to what has been done for the carbon nitride materials used in chapter 4, XPS spectra were used to obtain information on the structures of the pristine graphitic and the microwave-treated carbon nitrides, since they are (very) active in the arylamination reaction. Their N1s spectra are compared in Figure 5–12.

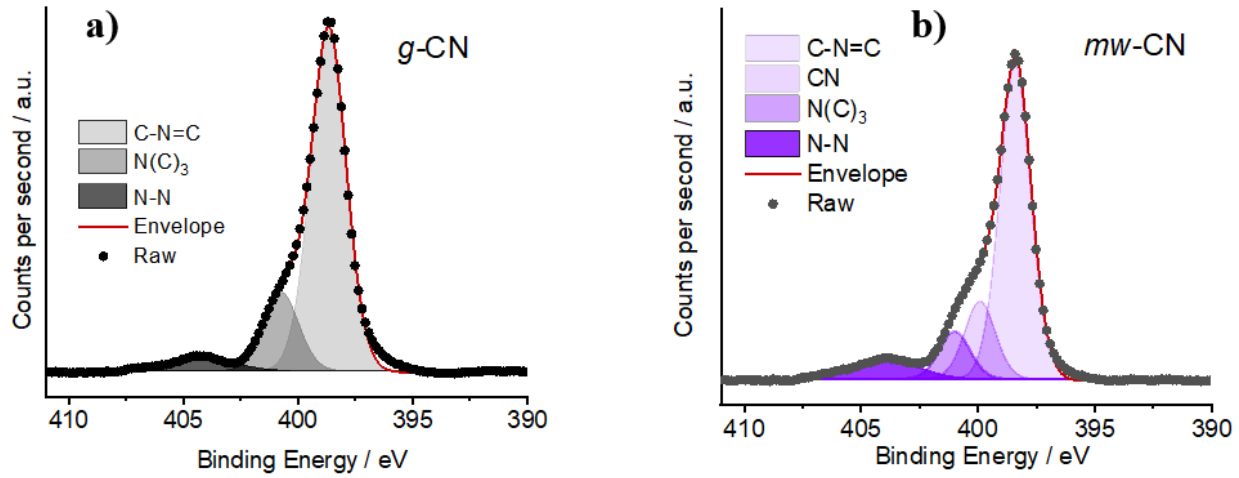

Figure 5–12: N1s XPS spectra of **a**) pristine *g*-CN **b**) *mw*-CN.

In the pristine *g*-C_3N_4, the typical intense signal assigned to the –C=N–C groups (≈ 398.3 eV) and another one near 401.0 eV assigned to the $N(C)_3$ chemical environment can be observed[13,14]. A very small signal attributed to N–N bonds is also present near 404.6 eV, which would suggest some minor loss of carbon atoms in the structure. Differently, the *mw*-CN form shows a lower content of carbon atoms and a higher content of nitrogen atoms, as also confirmed by the smaller C/N ratio measured: 0.70 vs 0.73 in pristine *g*-C_3N_4. This is consistent with the dominant signal at 398 eV but important changes are observed: (i) a decrease in the intensity of the $N(C)_3$ signal and, (ii) an increase of the N–N bonds signal. This reveals that *mw*-CN features carbon vacancies, which are expected to induce couplings among the vicinal nitrogen atoms. The new N–N bonds may therefore be the signature of the presence of **triazole** five-membered sub-units within heptazine blocks, whereas radical nitrogen atoms remaining after the cleavage of the C–N bonds could cause the formation of **amine** and **imine** functional groups via reaction with water, the solvent in which the microwave treatment is performed. The molecular model systems for these types of defects are shown in Figure 5–13, along with the model for *g*-C_3N_4. In this study, molecular systems were

preferred over periodic models (as used in chapter 4), because the excited-state calculations are more tractable with the former.

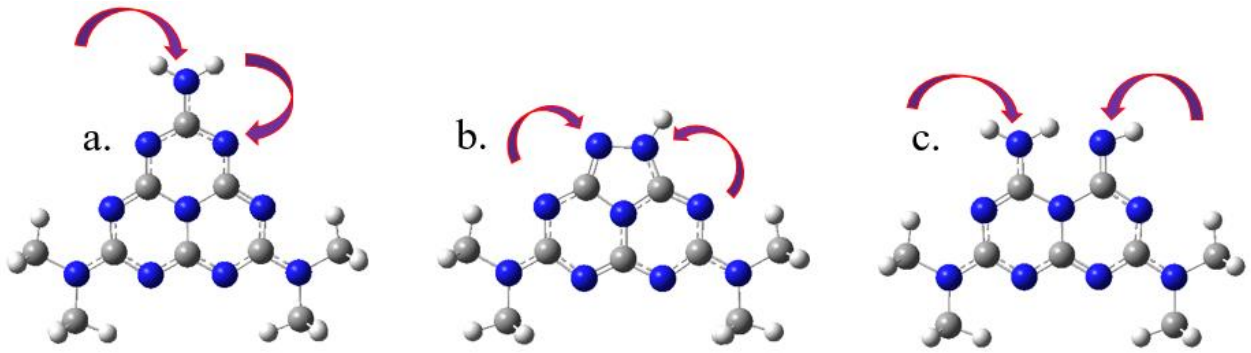

Figure 5–13: Models of the CNMs considered, with the coordination sites indicated by the red arrows: **a**) *g*-C_3N_4; **b**) Triazole-like *mw*-CN; **c**) Defective Amine/Imine *mw*-CN.

All three model systems possess "external" nitrogen atoms representing the bridging atoms between heptazine units in the real materials; there are two such atoms in the defective systems, at the bottom left and bottom right part of the molecules. Such nitrogen atoms have been saturated with methyl groups, to prevent them from acting as binding sites to nickel (see below). In the model of *g*-C_3N_4, the third external nitrogen has been saturated with hydrogen atoms, forming an amine group, to represent binding sites that can exist along the edges of *g*-C_3N_4 sheets. The triazole-like defect (structure **b**) is built with the characteristic N–N bond, one nitrogen atom bearing a hydrogen atom. In the Defective Amine/Imine model, amine and/or imine groups can form in an open sub-ring of the structure, as shown in **c**.

In principle, the nickel complex can interact with carbon nitride in two ways: either it can simply adsorb on the (defective) carbon nitride surface, interacting via van der Waals forces (physisorption), or one nitrogen atom on the surface can act as a ligand to the nickel ion, displacing one DMF molecule; the complex is then chemisorbed.

We first investigated physisorption situations; an example is given in Figure 5–14, for the square-planar complex with three DMF and one pyrrolidine ligands interacting with a model pristine *g*-C_3N_4 surface made of three heptazine units. There is no specific interaction between the partners, the distance between the nickel ion and the CN surface is large (≈ 5.0 Å) and the adsorption energy is small (≈ 10 kcal/mol), as expected for van der Waals systems. In terms of excited states, the lowest-energy transitions are localized on the complex, with very small oscillator strengths, and transitions involving a charge transfer from CN to the complex only appear around 330 nm, *i.e*, in the UV. This description, which holds for all the physisorbed systems that were examined, does not seem to provide a strong rationale for explaining the difference in efficiency between the CN catalysts observed experimentally.

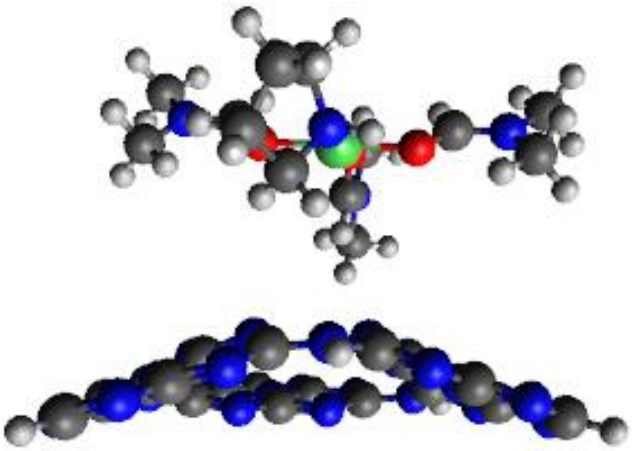

Figure 5–14: Square-planar Ni_3_DMF_1_pyrrolidine complex interacting with a model system for pristine *g*-C_3N_4.

We therefore turned to chemisorbed systems, in which one nitrogen atom of the carbon nitride surface coordinates the nickel ion. Two binding sites were selected for each molecular model for (defective) CN; those sites are marked by red arrows on Figure 5–13. On pristine *g*-C_3N_4, these are the protruding NH_2 group and one peripheral nitrogen atom of the heptazine unit; they represent

the edges of *g*-C_3N_4 sheets. For the triazole defect, they are the nitrogen atoms bound to each other (they differ by the presence of a hydrogen atom on one of them). For the amine/imine defect, the two binding sites are obviously the amine and imine nitrogen atoms.

Since pyrrolidine is a stronger ligand than DMF, it is reasonable to consider that the binding sites of (defective) carbon nitride would likely displace one DMF molecule from the nickel ion. Therefore, the systems that were modeled contain two DMF, one pyrrolidine and the (defective) CN model molecule around the nickel atom, in a square planar configuration. The persistence of pyrrolidine around the nickel atom is also essential for the "dark" part of the reaction, after the hypothesized photo-induced charge transfer.

Figure 5–15 shows the optimized structures of the CNMs-containing complexes, the first two structures representing nickel complexes coordinating pristine *g*-C_3N_4 and the four structures below representing nickel complexes coordinating *mw*-CN. To limit the steric hindrance, the CN molecular model has been set opposite to the pyrrolidine ligand. Table 5–7 lists their formation energies.

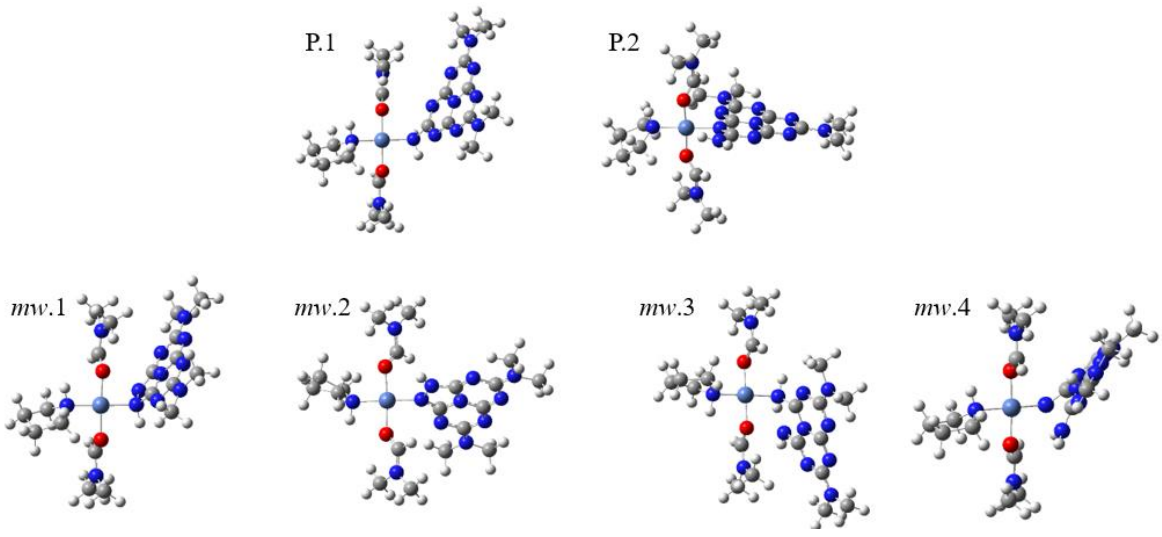

Figure 5–15: The CN-containing nickel complexes (B3LYP/Def2SVP; Ni: LanL2DZ): **P**.**1**) –NH_2-coordinating Pristine; **P**.**2**) N-coordinating Pristine; ***mw***.**1**) –NH-coordinating Triazole; ***mw***.**2**) N-coordinating Triazole; ***mw***.**3**) Defective Amine; ***mw***.**4**) Defective Imine. The CN ligand is always bound on the 'East' position of the complex.

Table 5–7: Formation energies of the CN-containing nickel complexes (B3LYP/Def2SVP; Ni: LanL2DZ).

Complex	**Formation energies (kcal/mol)**
–NH_2-coordinating Pristine	–86.6
N-coordinating Pristine	–96.6
N-coordinating Triazole	–94.6
NH-coordinating Triazole	–79.5
Defective Imine	–101.0
Defective Amine	–90.5

In terms of stability, these data show that the Defective Imine ligand more strongly bind nickel than all the others. The new functional group (–C=NH) created in the defective *mw*-CN is hence beneficial for a better complexation of the metal. N-coordinating Pristine, N-coordinating Triazole and the Defective Amine conclude the trend, demonstrating how the carbon nitride motifs can overall complex nickel, albeit preferably with lone nitrogen atoms. This indicates that the nickel complex in solution can chemisorb on: (i) the defects present at the surface of *mw*-CN, but also (ii) along the edges of the *g*-C_3N_4 sheets in the pristine material itself. These results seem consistent with the catalytic efficiencies recorded for the different types of CN materials (Table 5–1): the microwave treatment increases the density of binding sites by creating triazole and imine groups, which probably supplement the binding sites present at the edges and thus maximize the efficiency. Pristine *g*-C_3N_4, which has only edge binding sites, shows a lower but still sizable efficiency.

5.4 The excited states electronic structure of the nickel complexes bound to the CN surface

To rationalize the photocatalytic activity, the excited states of these complexes were modelled with TD-DFT. Besides strong bands in the UV range attributed to the absorption of carbon nitride and the vanishingly-small bands expected in the 600-800 nm range due to the spin–forbidden "*d–d transitions*", the complexes show a number of singlet electronic excitations at the UV-visible boundary. This energy range is reasonably close to that of the light used for the photocatalytic

experiments (450 nm), considering the fact that the calculations are performed on molecular models that are smaller, hence less delocalized, than actual (defective) carbon nitride sheets.

The nature of the electronic transitions, as analyzed with Attachment/Detachment Densities (see Fig. 5–16), clearly shows that the absorption bands around 400 nm have a predominant charge transfer (CT) character from the carbon nitride species to the nickel center, in particular to the $dx^2–y^2$ orbital, consistent with the EPR data. Such CT excitations are observed in both the defective structures and pristine heptazine, consistent with the fair photocatalytic activity of pristine *g*-C_3N_4.

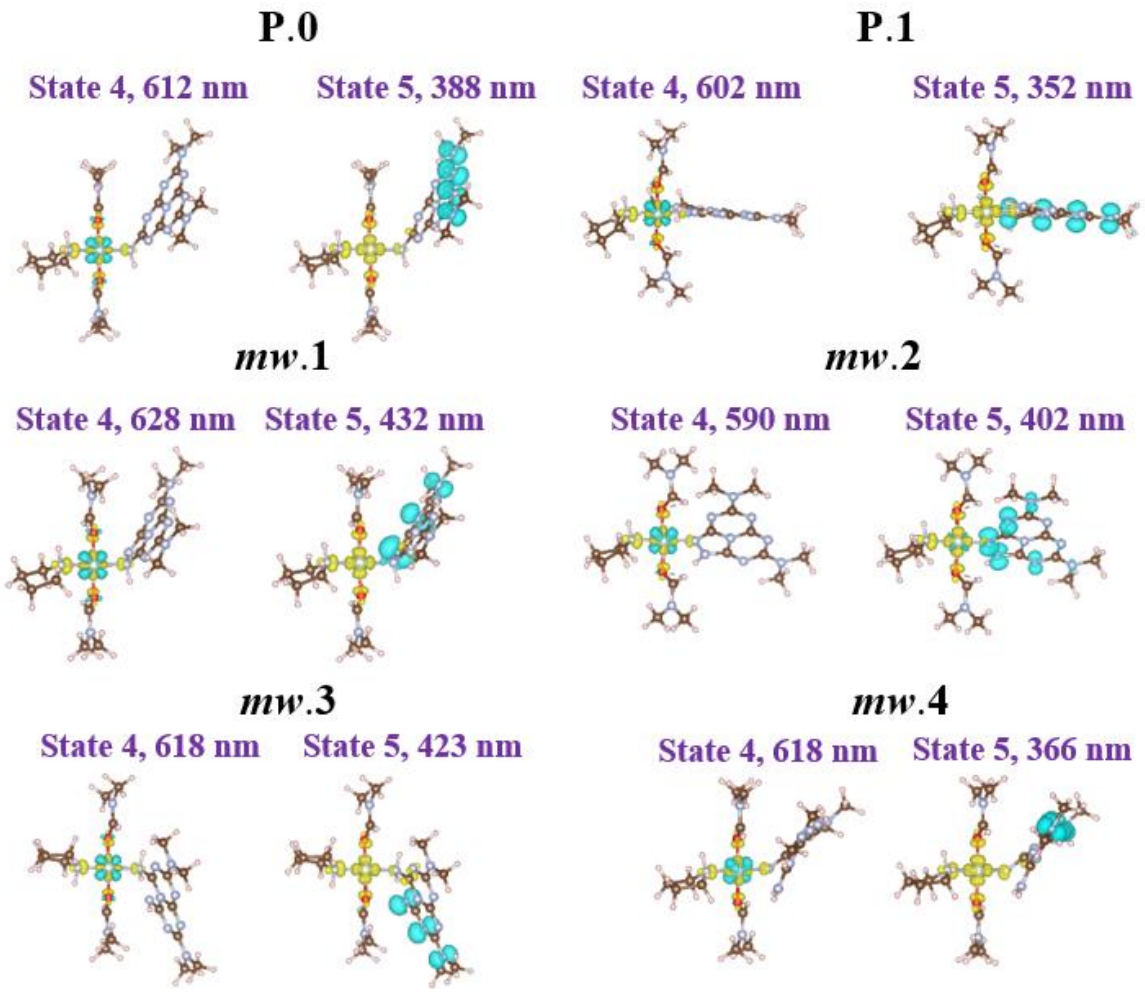

Figure 5–16: Attachment/Detachment Density of the models for *g*-C_3N_4 and *mw*-CN ligands in the square-planar nickel complexes (HSE06/Def2SVP; Ni: LanL2DZ). **P.0**: –NH_2-coordinating Pristine; **P.1**: N-coordinating Pristine; ***mw*.1**: –NH-coordinating Triazole; ***mw*.2**: N-coordinating Triazole; ***mw*.3**: Defective Amine; ***mw*.4**: Defective Imine. The hole and electron density is represented with light-blue and yellow bulbs, respectively.

Finally, the calculations were used to assess the stability of the corresponding Ni(I) complexes, which form after the photo-induced electron transfer from (defective) CN. The data in Table 5–8 indicate that all Ni(I) complexes, regardless of the nature of the carbon nitride ligand, are unstable (the formation energy is positive). This suggests that the nickel center dissociates from carbon nitride after the photoinduced charge transfer and that the following steps in the reaction mechanism, *i.e.*, the "dark cycle" comprising the actual coupling step, take place in solution.

Table 5–8: Formation energies of the Ni(I) complexes (B3LYP/Def2SVP; Ni: LanL2DZ).

Complex (Ni(I))	**Formation energies (kcal/mol)**
–NH_2-coordinating Pristine	+22.9
N-coordinating Pristine	+10.9
N-coordinating Triazole	+10.0
NH-coordinating Triazole	+30.5
Defective Imine	+13.8
Defective Amine	+25.6

5.5 Conclusions

This study is aimed at understanding how carbon nitride materials can pair up with transition metal complexes to catalyze cross-coupling reactions, exemplified here by the arylamination between methyl–4–bromobenzoate and pyrrolidine. To carry out that reaction, a novel microwave-treated carbon nitride (*mw*-CN) developed in Trieste was combined with a Ni(II) species. The reaction yield of such dual catalysis system turned out to be excellent, compared to the carbon nitride materials described in the previous chapter.

Quantum-chemical modelling has been used to provide the basic missing details of a reaction not yet understood. Although the limited and unclear experimental context, some relevant advancements provided by DFT can be remarked, such as (i) the suggestion of the actual structure of the Ni(II) complex present in solution; (ii) the nature of the interaction between that complex

and the carbon nitride surface; and (iii) the nature of the optically-excited states, opening the possibility of electron transfer from carbon nitride to the nickel species upon light absorption.

A UV-vis. absorption spectrum recorded in the DMF solution where the Ni salt was dissolved was the initial experimental data available, which was used in support for the computational approach. The theoretical calculations focused on hexa- and tetra-coordinated DMF complexes of the Ni(II) ion; they showed that the square-planar geometry displays a more similar optical spectrum to the experimental data, in particular the position at higher wavelengths of the excited states. Although they are affected by the Herzberg–Teller effect (*d–d transitions*), their evidence is provided. This, in turn, is supported by EPR measurements, which indicated that a square-planar geometry can be the responsible species featuring the abovementioned optical absorptions. Titration experiments and calculations also indicate that in the presence of pyrrolidine (one of the reagents), DMF can be substituted as ligand by it. A square-planar complex comprising three DMF molecules and one pyrrolidine molecule was thus used as model to investigate the subsequent steps in the reaction.

Concomitantly, XPS spectra recorded for *g*-C_3N_4 and *mw*-CN samples have shown that carbon atoms are lost during the microwave treatment, which induces the coupling between the radical nitrogen atoms left by the cleavage of the C–N bonds to form triazole sub-rings or amine/imine functional groups. Model molecular systems for those defects were built and made to interact with the model nickel complex, in order to evaluate the possibility that sites on the (defective) carbon nitride surface act as ligands for the nickel ion. The calculations indeed indicate that one nitrogen of the triazole ring and the imine nitrogen are capable of displacing one DMF molecule and coordinating the nickel ion. Interestingly, one peripheral nitrogen atom on pristine *g*-C_3N_4 can also bind efficiently to the metal atom.

Those dual systems made of a pyrrolidine-containing nickel complex attached to those specific sites of carbon nitride were then modelled with TD-DFT. They all show excited states at the UV-visible boundary with a clear charge transfer character between carbon nitride and the nickel atom, confirming the hypothesis of the photo-induced formation of a Ni(I) species as the first step in the reaction. Finally, the calculations show that the complexes between the Ni(I) atom and carbon nitride are not stable, implying that after the charge transfer, the nickel species migrates back to the solution for the following steps of the reaction, *i.e* the "dark cycle".

References

[1] M. Marchi, E. Raciti, S. M. Gali, F. Piccirilli, H. Vondracek, A. Actis, E. Salvadori, C. Rosso, A. Criado, C. D'Agostino, L. Forster, D. Lee, A. Foucher, R. K. Rai, D. Beljonne, E. Stach, M. Chiesa, R. Lazzaroni, G. Filippini, M. Prato, M. Melchionna, P. Fornasiero, *submitted,* (**2023**).

[2] E.K. Barefield, D.H. Busch, S.M. Nelson, *Quart. Rev. Chem. Soc.* 1968, 22, 457−498.

[3] P. Segla, H. Elias, *Inorg. Chim. Acta,* 149, (**1988**), 259−264.

[4] R.H. Holm, M.J. O'Connor, *Prog. Inorg. Chem.*, 14, (**1971**), 241−401.

[5] L. Sacconi, P. Paoletti, M. J. Ciampolini, *Am. Chem. Soc.* 85, (**1963**) 411−416.

[6] S. Roger Qiu, B.C. Wood, P.R. Ehrmann, S.G. Demos, P.E. Miller, K.I. Schaffers, T.I. Suratwala, R.K. Brow, *Phys. Chem. Chem. Phys.*, 17, (**2015**), 18913–18923.

[7] O. Laporte, W.F.J. Meggers, *Opt. Soc. Am.*, 11, (**1925**), 459.

[8] P. Pokhilko, E. Epifanovsky, A. I. Krylov, *J. Chem. Phys.*, 151, (**2019**), 034106.

[9] N. N. Karaush, R. R. Valiev, G. B. Baryshnikov, B. F. Minaev, H. Ågren, *Chem. Phys.*, 459, (**2015**), 65–71.

[10] R. Yamaguchi, M. Yamasaki, H. Sakiyama, *X-Ray Structure Analysis Online*, 27, (**2011**).

[11] J.D. Braun, I.B. Lozada, M. Shepit, J. van Lierop, D.E. Herbert, *RSC Adv.*, 11, (**2021**), 3547.

[12] R. van Meer, O.V. Gritsenko, K.J.H. Giesbertz, E.J. Baerends, *J. Chem. Phys.*, 138, (**2013**).

[13] C. Zhao, Q. Li, Y. Xie, L. Zhang, X. Xiao, D. Wang, Y. Jiao, C. Alexander, H. Price, B. Jiang, J. Liu, *J. Mater. Chem.* A, 8, 305, (**2020**).

[14] Y. Xiao, G. Tian, W. Li, Y. Xie, B. Jiang, C. Tian, D. Zhao and H. Fu, *J. Am. Chem. Soc.*, 141, (**2019**), 2508–2515.

Chapter 6: Conclusions and perspectives

6.1 Conclusions

The main objective of this dissertation was to understand how structural defects induced in 2D Carbon Nitride Materials (CNMs) modulate their catalytic response in organic syntheses of interest. To reach that purpose, we used computational chemistry to decipher the mechanisms by which functionalized carbon nitride acts as a photocatalyst in a number of reactions developed in Trieste. Several experimental publications highlight the importance of elemental and molecular doping as strategies for conveniently modifying their electronic properties[5–7] but little is known about how carbon nitrides actually intervene in a given reactive scenario. For this reason, the modification of the structure of pristine carbon nitride appeared to be a valuable strategy with which to shed light on the structure-activity relationship in the reactions investigated in this thesis, in particular a C–C bond-formation reaction between 1,3,5–trimethoxybenzene and nonafluoro–1–iodobutane and a dual Ni-carbon nitride arylamination reaction between pyrrolidine and methyl–4–bromobenzoate. The post-synthetic forms of carbon nitrides conceived for this scope, in addition to the pristine one, are a reduced carbon nitride, an oxidized and an amorphous one (*red*. CN, *ox*. CN, *am*. CN). To understand how the functional groups/defects generated in CN by the various treatments affect its photocatalytic efficiency, a Density Functional Theory study was designed and carried out.

For the perfluoroalkylation reaction described in chapter 4, convenient 2D and molecular models of the functionalized CNs were built, based on XRD data, which pointed out that the thermal treatment partially disrupts the molecular and crystal structure of *g*-C_3N_4, and on EPR data, which showed that all carbon nitrides considered contain radical species, with a higher content of radical centers in the amorphous form. The interaction profiles computed at the ground-state for the combined systems "CNMs + C_4F_9–I" showed that weak van der Waals interactions take place in

the case of pristine *g*-C_3N_4, whereas the interaction is stranger for the radical models representing amorphous CN. A slight lowering of the interaction energy is observed for the oxidized model of carbon nitride, probably due to the presence of oxygen, which repeals the iodine atom, another electron-rich element. As a result of the amorphous CN/C_4F_9–I interactions, the C–I bond of the fluorinated molecule experiences an elongation in the vicinity of the surface of carbon nitrides but also the C–F bonds.

The excited-state calculations provide the theoretical UV-vis. spectra of the carbon nitride models. These show that pristine CN mainly absorbs in the UV range, whereas the defective structures feature strong absorptions in the visible and the NIR region. The description of the hole (h^+) and electron (e^-) density distributions, as obtained from Attachment and Detachment Density Matrixes, shows that for pristine carbon nitride the charge redistribution associated to the major transition remains confined within its structure, indicating that pristine *g*-C_3N_4 is not favoring the electron-transfer to the fluorinated molecule. In contrast, the excited states around 500 nm for the models representing amorphous CN show a considerable transfer of electron density to the molecule, in particular around the C–I bond. As a result, the C–I bond strongly elongates, the extra charge is mostly localized on the iodine atom and a marked spin density appears on the neighboring carbon atom. This corresponds to the formation of a perfluoroalkyl radical species, which is the key intermediate for completing the perfluoroalkylation reaction. Overall, these results thus allow understanding the contrast in efficiency between pristine and amorphous CN photocatalysts for that reaction.

For the arylamination reaction described in chapter 5, an elucidation of the mechanism is presented, in the presence of a dual catalyst associating a nickel complex and a CNM, in particular a new microwave-treated carbon nitride (*mw*-CN). The microwave treatment, which induces the

formation of carbon vacancies, turns out to boost the catalytic efficiency, making *mw*-CN much better than pristine *g*-C_3N_4 and the functionalized CNs used in chapter 4. Here the DFT study addresses three questions: (i) the identity of the nickel complex in solution; (ii) the nature of the defects in the new amorphous carbon nitride, for which little experimental data was available; (iii) the nature of the optically-excited states, opening the possibility of electron transfer from carbon nitride to the nickel species upon light absorption.

To determine the nature of the nickel complex in solution, the UV-vis absorption spectra calculated for a variety of model systems were compared to the experimental spectrum obtained in DMF. It appeared that the first theoretical model of a hexa-coordinated DMF nickel complex showed no agreement with the experiment. A tetrahedral square-planar DMF nickel complex was then selected. Its theoretical optical spectrum shows an intense UV band and a very weak one in the visible, consistent with the measured spectrum and with EPR data indicating that the complex has a slightly distorted square-planar geometry. In order to simulate the presence of pyrrolidine in the reaction medium, other square-planar nickel complexes were built, where the DMF ligands were progressively substituted by pyrrolidines. The complexation energies computed indicate that pyrrolidine is a stronger ligand to nickel than DMF; the calculations also show that the absorption bands in the visible are expected to be blue-shifted upon pyrrolidine binding, in full agreement with the titration experiment of the DMF complex by pyrrolidine

To build a relevant model for *mw*-CN, we used XPS data showing that, in comparison with *g*-C_3N_4, the carbon content is lower and a new signal assigned to N–N bonds is present. The carbon vacancies left in the structure would induce N–N couplings, which would lead to the formation of triazole sub-rings. The nitrogen radical species formed upon carbon abstraction could also generate amine and imine groups. New square-planar nickel complexes coordinating those new carbon

nitride defective molecular models were built. In terms of stability, those complexes can clearly be separated in two groups: on one hand, the N-coordinating Triazole, the N-coordinating Pristine and the Defective Imine sites yield complexes that are more stable than the reference square-planar DMF complex. On the other hand, the complexes with the NH_2-coordinating Pristine, the Defective Amine and the NH-coordinating Triazole sites have similar or lower stability than the reference complex. The nickel complex is therefore expected to bind to the first three types of sites.

Concerning the excited-state calculations, the nature of the electronic transitions, as analyzed with Attachment/Detachment Densities, clearly shows that the absorption bands around 400 nm for all models have a predominant charge transfer (CT) character, from the carbon nitride species to the nickel center. Such CT excitations are observed in both the defective structures and pristine heptazine, consistent with the very high photocatalytic efficiency of the microwave-treated carbon nitride and with the fair activity of pristine *g*-C_3N_4. Importantly, the calculations also indicate that the Ni(I) species formed upon electron transfer from CN tends to desorb from the surface, therefore kicking off the "dark catalytic cycle" taking place in solution.

6.2 Perspectives

The results obtained in this work would deserve some further developments. In the first study reported here, the electronic structures of models of different forms of carbon nitrides are reported, for which mid-gap defect states appear in the DOS plots. It would be interesting to better characterize them in terms of quantum-chemical properties, including an analysis of a possible singlet/triplet interconversion. It was already shown that oxygen atoms favor such interconversion[8], so the presence of structural defects alone would be an additional explanation of the phenomenon of the relationship between electronic structure and texture.

In both studies reported, defective carbon nitrides show a tendency to interact with reaction partners (C_4F_9–I and nickel complexes). It would hence be interesting to try new reactive scenarios that involve different substrates and compute the nature and degree of interaction, for example with aromatic molecules. Often π–π stacking offers convenient organization in space and since carbon nitrides are generally conjugated systems, the possible existence of unpaired electrons in defective forms would render those interactions specific.

Finally, another interesting reaction would need theoretical elucidations: the oxidation of diphenyl sulfide to diphenyl sulfoxide mediated by the more strongly-oxidized carbon nitride form (CNO, see chapter 4, first paragraph) under light irradiation. This reaction involves CNO as the photocatalyst, diphenyl sulfide as the reagent and O_2 as a co-reagent along with diphenyl sulfide.

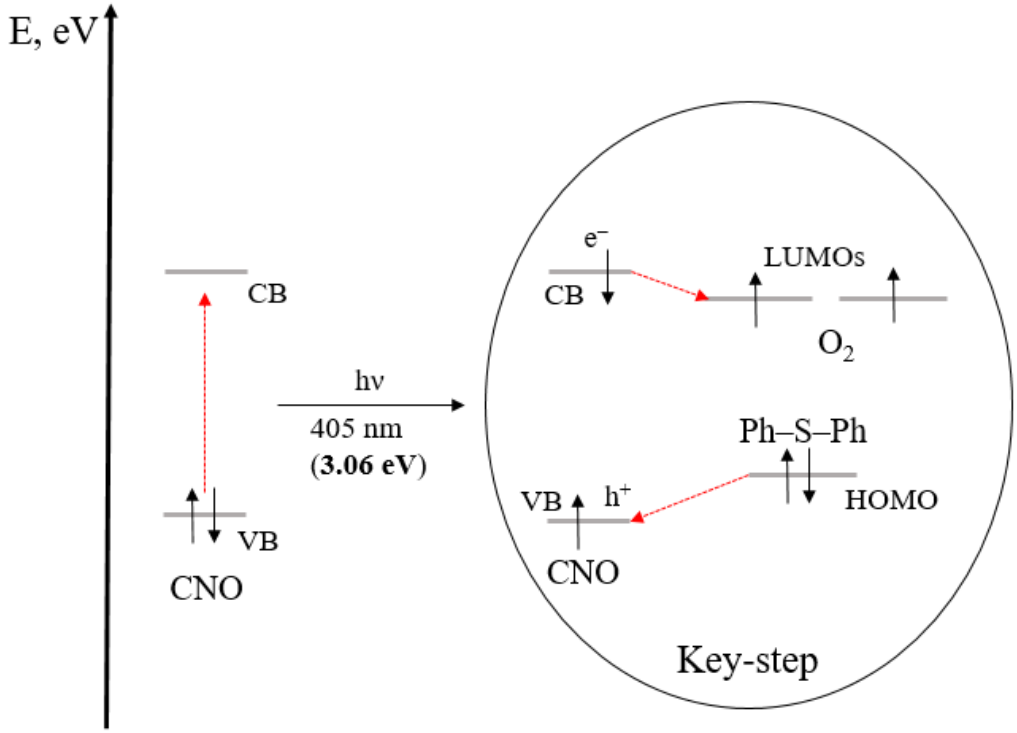

Figure 6–1: hypothesized reaction scheme of the CNO-assisted oxidation of diphenyl sulfide to diphenyl sulfoxide.

Upon light absorption (405 nm), CNO would be brought to an excited state, where an electron would be promoted to its Conduction Band, leaving in the Valence Band a positive vacancy (see Fig. 6–1). This latter would have a higher reducing potential than diphenyl sulfide, which would then transfer one electron from its HOMO to the VB of CNO. The electron promoted to the CB of CNO would be higher in energy than the LUMOs of O_2, which could then accept that electron, becoming a radical anion. This, in combination with the diphenyl sulfide radical cation, would couple to form diphenyl sulfoxide. The mechanism remained only a hypothesis and another DFT protocol would need to be set up to study it.

References

[1] J. Lin, W. Tian, H. Zhang, X. Duan, H. Sun, S. Wang, *Energy Fuels*, 35, 1, (**2021**), 7–24.

[2] C. Cometto, A. Ugolotti, E. Grazietti, A. Moretto, G. Bottaro, L. Armelao, C. Di Valentin, L. Calvillo, G. Granozzi, *2D Materials and Applications*, 5, 53, (**2021**).

[3] X. Wang, K. Maeda, A. Thomas, K. Takanabe, G. Xin, J. L. Carlsson, K. Domen, M. Antonietti, *Nature Materials*, 8, (**2009**), 76–80.

[4] C. Butchosa, P. Guiglion, M. A. Zwijnenburg, *J. Phys. Chem. C*, 118, 43, (**2014**), 24833–24842.

[5] J. Zhang, M. Zhang, S. Lin, X. Fu, X. Wang, *J. Catal.*, 310, (**2014**), 24–30.

[6] V. Hasija, P. Raizada, A. Sudhaik, K. Sharma, A. Kumar, P. Singh, S. B. Lonnalagadda, V. K. Thakur, *Appl. Mater. Today*, 15, (**2019**), 494–524.

[7] X. Han, A. Yuan, C. Yao, F. Xi, J. Liu, X. Dong, *J. Mater. Sci.*, 54, (**2019**), 1593–1605.

[8] H. Wang, S. Jiang, S. Chen, D. Li, X. Zhang, W. Shao, X. Sun, J. Xie, Z. Zhao, Q. Zhang, Y. Tian, Y. Xie, *Adv. Mater.*, 28, (**2016**), 6940–6945.